

Micropolar Continuum Modeling of Large Space Structures with Flexible Joints and Thermal
Effects: Theory and Experiment

Armaghan Salehian

Dissertation submitted to the faculty of the Virginia Polytechnic Institute and State University in
partial fulfillment of the requirements for the degree of

Doctor of Philosophy
In
Mechanical Engineering

Daniel J. Inman
Eugene M. Cliff
Donald J. Leo
Martin E. Johnson
Mary E. Kasarda
Thomas Michael Seigler

01/30/2008
Blacksburg, Virginia

Keywords: Micropolar Continuum Modeling, Vibrations, Large Space Structures,
Thermally Induced Vibrations, ISAT, Experimental Validation

Micropolar Continuum Modeling of Large Space Structures with Flexible Joints and Thermal Effects: Theory and Experiment

Armaghan Salehian

ABSTRACT

The presented work is intended to develop a geometrically reduced order (homogenized) model for a large antenna space structure with flexible joints. An energy equivalence concept is employed to find the continuum model for the system. The kinetic and strain energy expressions of the fundamental elements are found based on the assumptions of the micropolar elasticity theory. Necessary assumptions are made to reduce the order of the strain variables while retaining the effects of the micro-rotations that are coupled to the primary strain terms. As a result, a micropolar-based continuum model is found for the structure with torsional joints. The vibrations equations of motion for various coordinates of the one dimensional equivalent model are presented. Subsequently, the relations between the physical parameters of the distributed parameter model and the radar structure are introduced. The effect of the asymmetric mass distribution as a result of the addition of the radar panel to the truss system is studied. For the purpose of the experimental validation of the suggested model a planar truss structure with Pratt Girder configuration was built and tested in the laboratory. The results for the experimental frequency response functions are shown to be in good agreement with the theory. Finally, the continuum model is used to quantify the effects of the thermally induced disturbances on the satellite system during the eclipse transition.

Dedication

I dedicate this dissertation to my parents and to the memory of my
wonderful grandfather!

Acknowledgements

My highest level of gratitude and appreciation go to my wonderful advisor, Dr. Daniel J. Inman. Words cannot be brought to express my deepest appreciations for his help, support and encouragement. His advising skills, thoughtfulness, consideration, patience in mentoring me, and above all his astounding engineering insight into the problems were amazing! Working under his supervision at CIMSS has been one of the best opportunities I have had in my entire life, and it has turned out to be one of the most memorable experiences as well. I could not have had a better advisor! Now that I am leaving CIMSS, I notice that engineering knowledge was just a small part of the valuable asset that I gained. Working for Dr. Inman has taught me time management skills, talent in dealing with people, humor, how to make the research fun, and to be a better person. I am indebted forever for his encouragement, care and support. As he mentioned to me once, he will be my advisor for my entire life. I also eagerly look forward to having more research collaborations with him and to learn from him for always and forever.

I would also like to thank Dr. Eugene M. Cliff at the Interdisciplinary Center for Applied Mathematics at Virginia Tech for his many excellent suggestions to improve this research and his time to meet with me. I am also grateful to my great friend, Dr. Michael T. Seigler, for his support, care and valuable discussions. I am very appreciative of Beth Howell, our wonderful assistant at CIMSS, for all her help, for giving me hope, and for keeping track of things to make sure that everything has been done right. Beth has been like a second mother to me all these years, and I will remember all her favor always. I would also like to express my gratitude to my great committee member, Dr. Mary Kasarda, for her help, advice and her emotional support during my job application. In addition, I owe many thanks to my friends Olga and Maryland Pierrakos, Xingxi He, Dave Neal, Pablo Tarazaga, Arian Shahabi, Peggy Roshan, and Forough Javid for their friendship and for giving me courage and strength during the four years of my PhD. I would also like to acknowledge my friend, Dr. Thomas Wallmersperger, at the University of Stuttgart in Germany, for being a good friend and his great support during the months of his stay in Blacksburg. I greatly appreciate Dr. Mehdi Ahmadian for his strong recommendation upon my admission to Virginia Tech. Finally, my most gratitude goes to my wonderful parents, Aman Salehian, and Mehri Khatibi, and my two beautiful siblings, Arghavan and Ardalan Salehian, for loving me, believing in me, supporting me and for being on my side during all my decisions in my life. I am extremely grateful to all of you for what you have done for me for always and forever!

This research was supported in part by the Defense Advanced Research Projects Agency, under contract DARPA/NASA LaRC/NIA-VT2535 for which we are grateful.

Contents

Acknowledgements	iv
List of Figures	viii
List of Tables	xii
Nomenclature	xiv
1 Introduction	1
1.1 Literature Review.....	1
1.2 Research Summary.....	8
2 Homogenization Modeling of the Lattice	10
2.1 Strain Energy Derivations.....	11
2.2 Kinetic Energy Derivations.....	14
2.3 Equations of Motion.....	19
2.3.1 Lumped Mass Model.....	20
2.3.2 Plate Model.....	22
2.4 Truss Structure (No Panel)	24
2.5 PDE Solution.....	26
2.6 Frequencies and Wavelengths.....	29
2.7 Numerical Results.....	30
2.8 Conclusion.....	40
3 Model Experimental Validation	42
3.1 Introduction.....	42
3.2 Equations of Motion.....	43

3.3 Boundary Conditions.....	45
3.3.1 Mass and Moment of Inertia.....	45
3.3.2 Strings at Boundaries.....	47
3.4 Effect of Strain Variations on Kinetic Energy.....	48
3.5 Wavelengths and Frequencies.....	49
3.6 Experimental Setup.....	50
3.7 Numerical Results and Discussion.....	52
3.8 Summary and Conclusion.....	61
4 Micropolar Continuum Presentation	62
4.1 Strain Energy Derivations.....	63
4.1.1 Longerons (Tension, and Compression)	64
4.1.2 Longerons (Bending)	65
4.1.3 Battens (Tension, and Compression)	67
4.1.4 Batten (Bending)	69
4.1.5 Joints.....	70
4.2 Reduced Order Strain Energy.....	71
4.3 Equations of Motion.....	77
4.4 Strain Energy of Pratt Girder Truss.....	79
4.5 Reduced Order Strain Energy for Pratt girder Truss.....	80
4.6 Equations of Motion for Pratt Girder Truss.....	81
4.7 Experimental Setup.....	82
4.8 Numerical Results.....	85
4.9 Concluding Remarks.....	95

5 Thermally Induced Vibrations	97
5.1 Introduction.....	97
5.2 Problem Overview.....	104
5.3 Heat Conduction.....	106
5.4 Structural Response.....	114
5.5 Numerical Results.....	120
5.6 Concluding Remarks.....	125
6 Conclusion, Recommendations and Future Work	128
6.1 Conclusions.....	128
6.2 Future work and Recommendations.....	130
Bibliography	133
Appendix A- Strain energy derivations for the hinge model	142
Appendix B- Decoupling the equations of motion	151
Appendix C- Strain energy for the Pratt Girder truss	153
Appendix D- Micropolar model of the 3D truss	158
Appendix E- Strain energy calculations of the planar truss element	167
Vita	174

List of Figures

1-1 A 3-dimensional schematic of a proposed configuration for ISAT.....	3
1-2 A schematic of an inflatable truss element.....	3
2-1 Truss element and the reference coordinate system.....	11
2-2 Displacement and rotational components of the repeating element.....	13
2-3 Nodal velocity components of a bar.....	15
2-4 Radar panel modeled as lumped masses.....	16
2-5 Schematic view of the structure cross-section and bottom view of the element.....	18
2-6 Coupled longitudinal and bending motion for the truss panel assembly.....	20
2-7 Coupled torsional and bending motion for the truss panel assembly.....	21
2-8 Natural frequencies of the lumped mass model (W_0, U_0, Φ_y).....	35
2-9 Natural frequencies of the solid panel model (W_0, U_0, Φ_y).....	35
2-10 Natural frequencies of the lumped mass model (V_0, Φ_x, Φ_z).....	36
2-11 Natural frequencies of the solid panel model (V_0, Φ_x, Φ_z).....	36
2-12 Comparison of the frequencies of lumped mass model for (V_0, Φ_x, Φ_z) and (W_0, U_0, Φ_y)	37
2-13 Comparison of the torsional frequency for the lumped mass and plate model.....	37
2-14 Bending frequencies of the Timoshenko, FEM and the Euler Bernoulli model of the truss w/o panel.....	39
2-15 Error in frequency estimations with respect to the wavelength for the truss w/o panel	40
3-1 An inflatable rigidized boom.....	43

3-2 Schematic of bar members and joints in a truss element.....	44
3-3 A view of the joint and the interconnecting parts.....	44
3-4 Boundaries of the planar truss.....	47
3-5 Schematic of the truss and the wires.....	48
3-6 Schematic of the experimental setup.....	51
3-7 Photo of the experimental setup.....	52
3-8 Animation snapshots of the experimental mode shapes.....	52
3-9 Experimental and theoretical results: (a) Magnitude plot of the FRF, (b) Imaginary part of the FRF, (c) Phase plot, (d) Coherence plot.....	56
3-10 Magnitude of frequency response functions for the lattice with strings attached (dashed line) and without strings (smooth line).....	58
3-11 Magnitude of the frequency response functions for experiment (blue) and theory without strings (black).....	58
3-12 Magnitude of the frequency response functions for experiment (blue line) and theory with no mass-string at the boundaries (black line).....	59
3-13 Coherence values around the fourth natural frequency.....	59
3-14 Error of the frequency estimations with respect to wavelengths.....	59
4-1 A comparison between a regular and a micropolar continuum (θ_i and θ_j micro-rotations) and (Ψ macro-rotation).....	63
4-2 Longer members in bending and the angular coordinates.....	64
4-3 Deflection components of a member in bending.....	65
4-4 Bending and extension of battens for ε_y	67
4-5 Bending deflection components of the battens.....	69

4-6 Angular deflections of the battens and the torsional joints.....	70
Figure 4-7 Schematic of an n-degree of freedom mass-spring system.....	72
4-8 Schematic of the coupling between twist and bending in y direction.....	78
4-9 Schematic of the planar truss element with members in bending.....	80
4-10 A schematic of the experimental setup.....	82
4-11 Photo of the experimental setup.....	83
4-12 A polynomial fit of the torque and torsional strain values.....	84
4-13 FRF after modeling joints.....	95
5-1 Schematic view of the Earth shadow on the Satellite (full and partial shadows).....	98
5-2 Photos of the SAFE courtesy of NASA Langley Research Center.....	99
5-3 A view of the heat conduction in the truss element.....	107
5-4 A view of the Earth and the ISAT orbit.....	108
5-5 A Schematic of the bottom side of the truss repeating element.....	110
5-6 Heat transfer in the front side of the repeating element.....	110
5-7 Heat transfer in the back side of the repeating element.....	110
5-8 The heat transfer schematic along a diagonal member.....	114
5-9 Thermal forces at the cross section.....	115
5-10 Non-dimensionalized temperature profile at the ends of a diagonal member.....	122
5-11 Variation of the thermal torque with respect to the temperature.....	122
5-12 The quasi-static torsion at the tip.....	122
5-13 The dynamic twist at the tip.....	123
5-14 The lateral oscillations as a result of the torsion at the tip.....	123
5-15 Dynamic twist with respect to the variation of the thermal conductivity.....	124

5-16 Dynamic twist with respect to the variation of the thermal diffusivity.....	124
5-17 Variation of the dynamic thermal twist with both diffusivity and conductivity.....	125
5-18 Dynamic twist with respect to the variation of the thermal capacity.....	125
5-19 An alternative element configuration (less susceptible to thermal vibrations).....	127
C-1 Schematic view of a bar and the nodal velocities.....	157
D-1 Bending and extension of battens for ε_z	159
D-2 Bending and extension of battens for ε_{yz}	160
D-3 Bending and extension of battens for ε_{zy}	161
D-4 Schematic of a beam member, the deflection components and nodal reactions.....	162
E-1 Batten member and the bending components.....	168
E-2 Longerons members and the bending components.....	168
E-3 Bending of the diagonal member for ε_x and κ_z	169
E-4 Bending of the diagonal member for ε_z	170
E-5 Bending of the diagonal member for ε_{zx}	170
E-6 Bending of the diagonal member for ε_{xz}	171
E-7 Extension of the diagonal member for ε_x	171
E-8 Extension of the diagonal member for ε_z	172
E-9 Extension of the diagonal member for ε_{zx}	173
E-10 Extension of the diagonal member for ε_{xz}	173

List of Tables

2-1 Material and geometrical properties of the truss.....	11
2-2 Natural frequencies of the lumped mass model for bending, longitudinal, and rotation of the cross section (W_0, U_0, Φ_y) in (rad/sec).....	33
2-3 Natural frequencies of the solid panel model for bending, longitudinal, and rotation of the cross section (W_0, U_0, Φ_y) in (rad/sec).....	33
2-4 Natural frequencies of the lumped mass model for bending, torsional, and rotation of the cross section (V_0, Φ_x, Φ_z) in (rad/sec).....	34
2-5 Natural frequencies of the solid panel model for bending, torsional, and rotation of the cross section (V_0, Φ_x, Φ_z) in (rad/sec).....	34
2-6 Natural frequencies of the truss w/o panel for bending in (rad/sec).....	38
2-7 Longitudinal natural frequencies of the truss w/o panel (rad/sec).....	38
2-8 Torsional natural frequencies of the truss w/o panel (rad/sec).....	39
3-1 Material and geometrical properties of the bar members.....	60
3-2 Properties of the truss.....	60
3-3 Theoretical and experimental natural frequencies.....	60
3-4 Theoretical and experimental natural frequencies (strain components included in the kinetic energy terms).....	60
4-1 Nodal bending deflection components of the fundamental element.....	66
4-2 Static deflection measurements and weight values.....	84
4-3 Natural frequencies for $L=12\text{ m}$ and $A_L=0.00729659\text{ m}^2$	86
4-4 Natural frequencies for $L=30\text{ m}$ and $A_L=0.00729659\text{ m}^2$	87

4-5 Natural frequencies for $L=60\text{ m}$ and $A_L=0.00729659\text{ m}^2$	88
4-6 Natural frequencies for $L=300\text{ m}$ and $A_L=0.00729659\text{ m}^2$	89
4-7 Natural frequencies for $L=12\text{ m}$ and $A_L=0.00024322\text{ m}^2$	90
4-8 Natural frequencies for $L=30\text{ m}$ and $A_L=0.00024322\text{ m}^2$	91
4-9 Natural frequencies for $L=60\text{ m}$ and $A_L=0.00024322\text{ m}^2$	92
4-10 Natural frequencies for $L=300\text{ m}$ and $A_L=0.00024322\text{ m}^2$	93
4-11 Experimental and theoretical natural frequencies in Hz.....	94
D-1 Nodal reactions for the rotational and displacement components.....	162

Nomenclature

A_L, A_d, A_b	=cross-sectional area of longerons, diagonals and battens
$A^{(k)}$	=cross-sectional area of member k
$A_{eq.}$	=cross sectional area of the equivalent continuum model
c	=wave speed
c_L, c_b, c_d	=thermal capacity of longerons, diagonals and battens
d_j	= mode contribution factor
E_L, E_d, E_b	=modulus of elasticity of longerons, diagonals and battens
$E^{(k)}$	=modulus of elasticity of member k
$E_{eq.}$	=modulus of elasticity of the equivalent continuum model
f	=frequency (Hz)
I_x, I_y, I_z	=mass moments of inertia of the panel
I_b	=mass moment of inertia at the boundaries
$I_{eq.}$	=moment of inertia of the equivalent continuum model
K	=element stiffness matrix
K	=thermal conductivity
L_L, L_b, L_d	=length of longerons, diagonals, and battens
$L^{(k)}$	=length of member k
$l_i^{(k)} (i=1 \rightarrow 3)$	=directional cosines of member k
m_b	=mass at the boundaries
m_j	=mass of the joints
M_x, M_y, M_z	=moments at the cross section of the truss element
m_p	=mass of panel distributed among the joints
m_{panel}	=mass of the panel on a truss element
N	=longitudinal force
Q_y, Q_z	=shear force
Q_b, Q_d	=heat transferred through the battens and diagonals
t	=time
T_e	=kinetic energy of the truss element
$T^{(k)}$	=kinetic energy of member k

T_j	=kinetic energy of the joints
T	=temperature
U, W, Ω	=mode vectors
U_e	=strain energy of the truss element
$U^{(k)}$	=strain energy of member k
U_{bt}, U_{bb}	=extensional and bending energy of battens
U_{Lt}, U_{Lb}	=extensional and bending energy of longerons
U_s	=strain energy of the joints
V_{ix}, V_{iy}, V_{iz}	=velocity components of node i of a bar member
u, v, w	=displacement components in (x, y, z) directions
u_0, v_0, w_0	=displacement components evaluated at the center of the cross section
x, y, z	=Cartesian coordinates
$\varepsilon_x, \varepsilon_y, \varepsilon_z,$ $\varepsilon_{xy}, \varepsilon_{yz}, \varepsilon_{xz}$	=strain components evaluated at the center of the cross section
$\varepsilon_{ij}^{(k)}$	=strain components of member k
Φ_x, Φ_y, Φ_z	=rotational degrees of freedom
$\kappa_x, \kappa_y, \kappa_z$	=curvature components evaluated at the center of the cross section
K	=thermal diffusivity
α_i	=mode shape parameters
$(i:1 \rightarrow 6)$	
λ	=wave length
$\rho^{(k)}$	=density of member k
$\rho_{eq.}$	=density of the equivalent continuum model
$\theta_{Ly_i}, \theta_{Lz_i}$	=bending angles of longerons in y and z direction
θ_{ib}	=bending angles of battens
ω	=natural frequency (rad/sec)

Chapter 1

Introduction

1.1 Literature Review

During the past few years there has been increasing interest to enable in orbit nonstop surveillance of moving ground targets on earth. The Innovative Space Based Radar Antenna Technology (ISAT) program funded by the Defense Advanced Research Projects Agency (DARPA) is an example of this program. A schematic of a proposed configuration for the ISAT structure (a 300 m truss) is shown in Figure 1-1. It is desirable for the satellites designed for this purpose to operate in a Medium Earth Orbit (MEO) to provide improved coverage. Such technology will require fewer satellites for global coverage and thus reduce the overall system cost. Generally, large low mass density orbiting structures have proved promising for space applications. A radar antenna operating at MEO, in particular, must be so large that it can not be launched on existing rockets. Space inflatable structures which can be compressed into far smaller packages and easily deployed into their load-bearing configurations provide one possible approach for placing large metrology systems in space. Figure 1-2 shows an inflatable fundamental element for a space truss. Inflatable structures have many advantages compared to

mechanically installed structures, such as lower weight, higher packaging efficiency, and easier maintenance. Such structures have a long history of use in aerospace applications, from the ECHO series of satellites in the 1960's to L'Garde's space shuttle launched Inflatable Antenna Experiment (IAE) in May 1996.¹ Many proposed inflatable designs for space applications consist of truss-like or lattice structures with repeated patterns since they are simple to construct and they have large stiffness to mass ratios. Therefore, an approach for studying the dynamic response of these structures has been a topic of importance.

In this regard, two approaches that have received attention are the finite element method (FEM) and the continuum model. While the FEM is a popular approach and sometimes an indispensable tool for analyzing complex systems, it also requires thousands of elements to represent a large structure with many components. Hence, FEM requires significant amount of time and computing capacity to obtain reliable solutions. Therefore, they naturally lead to models that may become too large for control design. Finally, in a dynamic analysis the FEM usually produces more modes of vibration than are actually needed.² Alternatively, it has been shown that the dynamics of repeated lattice structures can be approximated well by a continuum models.³ Therefore, equivalent continuum modeling methodology offers an attractive alternative to the discrete finite element approaches for the analysis of repetitive and quasi-repetitive lattice structures. Continuum modeling techniques have the advantage of reduced number of modal parameters, and can be an efficient method for static and dynamic analysis of large lattice type structures. On the other hand, analytical solutions provide enhanced understanding into dominant structural physics and underlying mechanics and can be used as a strong tool for preliminary design. Additionally, the existing methods for the design of control systems for distributed parameter models⁴ can be applied effectively if an appropriate continuum model and analytical

solution of the structure can be found. For example an analytical solution in the form of a beam or a plate model for lattice type structures opens the possibility of constructing input-output transfer functions between the sensing and actuation points⁵, thus enabling the use of many well-established frequency-based control methods.

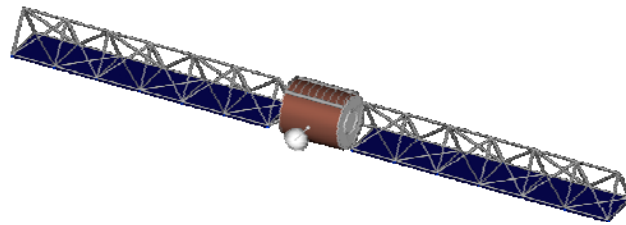


Figure 1-1 A 3-dimensional schematic of a proposed configuration for ISAT
(Courtesy of Pablo Tarazaga)



Figure 1-2 A schematic of an inflatable truss element

-What is continuum modeling?

Briefly, continuum modeling is a methodology that takes advantage of the periodicity in the pattern of a structure to produce a geometrically reduced order model (a PDE in a single spatial variable) of the system. This has the benefit of avoidance of a modal order reduction as opposed to the FEM. The continuum modeling technique captures the global dynamics of the structure only, which makes it a strong tool for very large, complex structures, where the overall dynamics of the system are dominant. In contrast to the FEM where the approximate shape functions and

interpolating polynomials are used to obtain a solution, in continuum modeling the solution to the PDE of the system are used to describe the dynamics of the system.

An extensive list of some notable research in the analysis of lattice structures by continuum modeling is presented in [6, 7, 8, 108 and 109]. A review of the literature reveals that the continuum modeling techniques can be classified as: 1) the discrete field analysis^{8, 9, 10, 11, 12, 13} and 2) the substitute continuum approach.^{14, 15, 16, 17, 18, 19}

In the discrete field approach the repeated pattern of the structure is taken into account. The method involves writing equilibrium and compatibility equations at nodes which result in the finite difference equations for the system. The discrete field analysis can be categorized in to two different classes⁸: Micro method, by which one constructs and solves difference equation models (or difference differential equations for mixed discrete-continuous systems), and the Macro method, by which one constructs and solves the summation equation models (or summation integral equations for mixed discrete continuous systems).

The substitute continuum approach can be further classified as methods that employ either 1) the energy equivalence^{14, 15, 16, 17, 18, 19} or 2) the stiffness equivalence concepts. For the stiffness equivalent approach, there are two methods used in the literature. It is either the direct approach to find the stiffness of an isolated lattice and relate that to the equivalent stiffness of a continuum,^{2, 20, 21, 22, 23, 24, 25, 26, 27} or, the use of the transformation matrices to relate the contribution of the elements in a truss system to the global stiffness of the structure.^{28, 29, 30}

The continuum modeling of structures received much attention in the early 1960's.^{11, 12, 31} Wah studied the free lateral oscillation of supported grillages by deriving a finite difference based continuum approach.³¹ Later Renton studied the dynamic behavior of plane grids using a more rigorous technique.¹¹ In his analysis he uses a Taylor series expansion, to transform the

stiffness equations written in terms of the finite difference operators into differential equations for the system. In another example a discrete field analysis is used to find the continuum model for spatial anisotropic beam-like trusses with pin connections.¹³ The static deformation of a quasi-repetitive planar truss is studied in another work.¹⁰ The authors use a finite difference approach to find the nodal balance equations as well as the force displacement relation to find the equivalent continuum model for the system.

Some other works done by Noor involves derivations of energy equivalence based continuum models for double layered grids and spatial beam-like trusses to perform thermo-elastic stress analysis and to find reduced order FEM models for the structures.^{15, 17} The difference between the approaches in [15] and [17] is that certain local effects are included in [17] to simulate the dynamic responses more accurately. This author in a related work extends this method to the fundamental truss elements with four longerons to account for the warping of the cross sections.¹⁶ The bucking and stability of the same type of structures using energy equivalence based continuum models are presented in another article.¹⁸ The effects of the asymmetric geometrical configurations (an orthogonal tetrahedral pattern) on the coupling between different modes of vibration are also studied by Noor.²⁷ In a different study a polynomial representation is used to transform the nodal coordinates to the strain variables.¹⁹ In this article, the strain energy expression is reduced and written in the form of the variables for a continuum model by explicitly eliminating the secondary strain variables. Additionally, the structural defects are introduced to the continuum model to study their effect on coupling between the various deformations modes. In a study performed by Burgardt, the average of the strain and stress values over a planar truss cell is used to find an energy equivalent continuum model.¹⁴

There are a few ad hoc schemes where the equivalent stiffness approach is used for deriving equivalent continuum models of lattice structures.^{2, 16, 20, 21, 22, 23, 24, 25, 29, and 30}

In the equivalent stiffness approach, the effective shear and bending stiffness' of the repeating cell are found and related to the reduced order strain variables of the continuum model. They use either a unit load approach or employ a transformation matrix to find the contribution of the individual components stiffness' to the overall stiffness of the element.^{28, 29, 30} In a related work, these effective continuum properties are then used to study the relative structural efficiencies (e.g., modulus-to-density ratios) of various truss configurations.²⁵ An inverse method is used to identify the dynamic properties of a plate-like structure in another research effort.³² The authors build a maximum likelihood estimator to estimate the physical parameters of the equivalent plate model based on a known response (an inverse approach). The continuum modeling techniques are extended in a research study to model material nonlinearities and to present lattices which have similar behavior as the elasto-plastic constitutive behavior.³³

During the past few years, continuum modeling techniques have found many applications in other engineering fields such as materials science^{34, 35, and 36}, civil engineering^{37, 38, and 39} and biomechanics.⁴⁰ In addition, the continuum methodology has been combined with multi-scale modeling techniques for adaptive modeling of molecular systems behavior.³⁵ In another work the mechanical anisotropic plastic behavior of the lattice materials has been modeled using standard homogenizations techniques.³⁶ The stated work, [36], involves building micromechanics based finite strain constitutive models for the truss lattice materials. In Ref. 34, lattice block materials (LBM) are modeled as continuum plates to find their effective constitutive and mass properties. In Ref. 40 the equivalent continuum mechanical model for the microstructures of bones are found. Additionally, the homogenization techniques have received much attention by

mathematicians. There are examples of some rigorous mathematical techniques for homogenization of structures with periodic patterns.^{41, 42} In Ref. 41, the authors develop a mathematical equivalent continuum model for hexagonal configuration lattices. In Ref. 42 the periodic unfolding method is used as a tool for multi-scale homogenization of grids.

Most of the work done on the continuum modeling for the truss type structures assumes hinge connections between the members. There are a few existing articles in the literature where joints are modeled as rigid connections for trusses,^{43, 44, 45} and grids^{12, 46}. A difficulty pertaining to the derivation of the continuum models for inflatable deployable structures are the connections. The joints for these structures are different connection types than pin or rigid joints studied in the previous research. In addition, an experimental effort made for a small scale metal truss based on the assumption of hinge connections revealed the need for an alternative modeling.

The work presented in this dissertation aims to fill this gap. In the presented work we develop a somewhat rigorous mathematical technique to find a very simple micropolar continuum model for a truss structure with flexible joints.

In addition, very few of the previously published efforts on continuum modeling of repeated lattice structures have been validated experimentally.^{48, 49} Due to the large size and flexibility of the space structures they cannot be tested under the laboratory conditions. However, it is possible to ground test the individual components of these structures in their inflated and rigidized state as previously done in some of the research.^{50, 51, 52} Once the physical parameters of these components are tested and known, it is desirable to be able to build a model of the system made of these components. In a research performed to validate a continuum modeling approach by Webster et. al., the nonlinear model for the joints of a NASA Mini-Mast truss element is

presented, and an experiment is conducted for the purpose of model validation.⁴⁸ The errors for the first two bending frequencies in this study are about 11%. In some other related work⁴⁹, the authors present a very simple model for a 19 ft. lattice structure, which is a slender beam with a tip mass. The results show a frequency error around 92% for the first two frequencies. The micropolar continuum methodology developed in this effort is validated experimentally for a metal truss and results in much more accurate frequencies and the frequency response functions.

1.2 Research Summary

The following outlines a summary of the presented research and its contributions. In Chapter 2, as a preliminary analysis, hinge joint connections are assumed for the 3D structure shown in Figure 1-1. The approach taken here is to use the repeated lattice nature of the design to provide continuum models of the structure resulting in low order modal modes which can be useful for design and control. These models are computationally much cheaper and analytically simpler to design with. The assumptions for the linear displacement and strain fields as previously made in [17] are used for the strain energy derivation and to find a reduced order model. Taylor series expansions are used to account for the local effects within the element. A continuum model for the space truss with asymmetric mass distribution is derived. The effects of the asymmetry due to the addition of the radar panel, which weighs 12 times more than the actual truss structure, are investigated. The results for the continuum model are then compared to the FEM for the purpose of validation. The relations for the characteristics of a dynamically equivalent continuum model of this structure are also presented. In Chapter 3, the approach presented in Chapter 2 has been modified for a truss structure with a planar configuration. The experimental results for this truss are used for the purpose of validation. Chapter 4 presents a methodology for a micropolar continuum modeling for the truss with flexible joints. This modeling technique includes higher

order strain field components compared to the model presented in Chapter 2. Necessary assumptions are made to reduce the order of the strain variables while retaining the effects of the micro-rotation strain states that are coupled to the primary strain terms. The effects of various torsional stiffness values for structures of different lengths are compared and investigated. The approach is then applied to the planar truss configuration for the purpose of experimental validation. In Chapter 5, the continuum model used for the truss has been employed to analyze the thermally-induced vibrations resulting from passing the eclipse line in space and the instantaneous temperature gradients. An extensive literature review of the thermally induced disturbances and their effects on space structures is presented in Chapter 5. As presented in that chapter, the continuum models can effectively be used to predict the thermal oscillations in space. It is also shown that contrary to the statement previously made by Thornton,^{57, 70} the limiting assumption regarding the isothermal members for the continuum models is not necessary when a decoupled thermal structural analysis is of interest. Finally, the summary and conclusion of the conducted research are presented in Chapter 6.

Chapter 2

Homogenization Modeling of the Lattice

This chapter introduces a method for deriving a continuum model for a repeated lattice structure with an asymmetric mass distribution due to the addition of the radar panel. Motivated by the current ISAT technology, the truss structure has a triangular cross-section and is made of double-bay elements shown in Figure 2-1. The battens, diagonals and the longerons shown are constructed of tubes. Following [110], the material and geometrical properties presented in Table 2-1 are used as a starting point for the present analysis. The structure is a 300 (m) truss with the radar panel mounted to the side. Because the structure has a repeated pattern, determining the kinetic and strain energy expressions of the fundamental repeating element is the first step in finding an equivalent 1-D model. Necessary assumptions are made while preserving the effects of the three-dimensional strain field, to couple and express these strain values in terms of the independent strain states. The independent strain states are similar for those of the homogenized model. Subsequently, the effective dynamic coefficients for the equivalent beam type model of the structure are found. Hamilton's principle is then used to find the equations of motion for six coordinates of vibration.

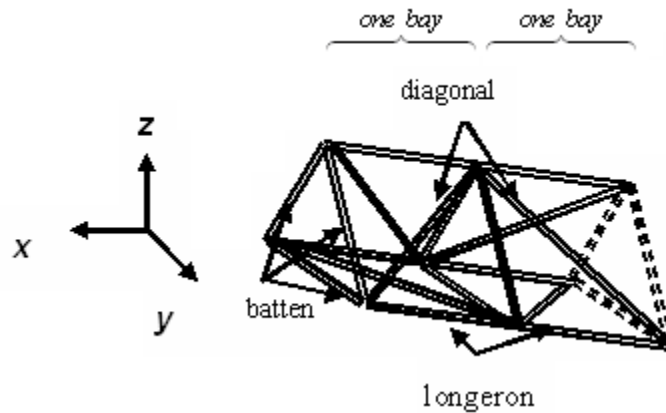


Figure 2-1 Truss element and the reference coordinate system

Table 2-1 Material and geometrical properties of the truss

Truss Properties	Values
Length of the antenna truss	300 m
Length of battens and longeron members	3 m
Modulus of Elasticity of batten, longeron and diagonal	6.8948×10^4 Mpa
Mass density of batten, longeron and diagonal	1799 Kg/m ³
Diameter of diagonal and batten	25.4×10^{-3} m
Diameter of longeron	76.2×10^{-3} m
Thickness of diagonal and batten	0.508×10^{-3} m
Thickness of longeron	1.016×10^{-3} m
Total mass of the radar panel	6000 Kg
Mass of the truss	550 Kg

2.1 Strain Energy Derivations

As a preliminary analysis we assume that the truss elements are made of pin joints. This assumption is modified in Chapter 4 where a more complex design for the joints is presented. The method presented in this chapter extends the earlier work of Noor (for symmetric configurations) who pioneered homogenization methods in the late 70's and early 80's.¹⁷ Considering we have a truss element shown in Figure 2-1 which is made of pin joints, we assume

linear variations for displacement components at the plane of the cross-section. The displacement components for any point along a bar member at the cross section can be expanded linearly in terms of the displacement components at the center of the cross section. Such displacement components are shown in Figure 2-2. Also the effect of the extensional and the shear strains on the displacement components are included in this formulation. So making an assumption for a linearly varying displacement field we get,¹⁷

$$\begin{aligned}
 u(x, y, z) &= u_0(x) - y\phi_z(x) + z\phi_y(x) \\
 v(x, y, z) &= v_0(x) + y\varepsilon_y(x) + z\left[-\phi_x(x) + \frac{1}{2}(2\varepsilon_{yz}(x))\right] \\
 w(x, y, z) &= w_0(x) + y\left[\phi_x(x) + \frac{1}{2}(2\varepsilon_{yz}(x))\right] + z\varepsilon_z(x)
 \end{aligned} \tag{2.1}$$

where u_0, v_0, w_0 are the displacement components at the center, ϕ_x, ϕ_y, ϕ_z are the rotations about the x, y, z axes shown in Figure 2-2, and $\varepsilon_y, \varepsilon_{yz}, \varepsilon_z$ are the extensional and the shear strain components at the center of the cross-section. To find the equivalent homogenized model, it is necessary to write the strain energy of an element in terms of the strain values of a beam $\varepsilon_x, \varepsilon_{xz}, \varepsilon_{xy}$ and the curvature components. Such strain components should be evaluated at the center of the element. As mentioned earlier, the assumptions in Ref. 17 with regards to a shear deformation type beam, the compatibility conditions and the free local deformations are used for the strain energy derivation of a reduced order model. A complete derivation for this is presented in the Appendix A.

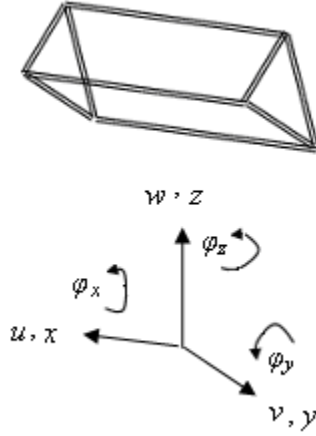


Figure 2-2 Displacement and rotational components of the repeating element

Finally the strain energy of the repeating element can be found in terms of the strain and curvature components at the center as follow,

$$\begin{aligned}
 U = & 3A_L E_L L_L (\varepsilon_x)^2 + \frac{1}{2} A_L E_L L_b^2 L_L \left((\kappa_y)^2 + (\kappa_z)^2 \right) + \frac{24A_d A_L E_d E_L L_b^2 L_d L_L^2}{A_d E_d L_d L_L^3 + 4A_L E_L (L_b^2 + L_L^2)^2} \left((\varepsilon_{xy})^2 + (\varepsilon_{xz})^2 \right) \\
 & + \frac{A_d A_L E_d E_L L_b^4 L_d L_L^2}{4 \left(A_d E_d L_d L_L^3 + A_L E_L (L_b^2 + L_L^2)^2 \right)} (\kappa_x)^2
 \end{aligned} \tag{2.2}$$

Using the spatial derivative of the displacement components in Eq. (2.1), one can easily found,

$$\varepsilon_x = \frac{\partial u_0}{\partial x}, \varepsilon_{xy} = \frac{1}{2} \left(\frac{\partial v_0}{\partial x} - \phi_z \right), \varepsilon_{xz} = \frac{1}{2} \left(\frac{\partial w_0}{\partial x} + \phi_y \right), \kappa_y = \frac{\partial \phi_z}{\partial x}, \kappa_z = \frac{\partial \phi_y}{\partial x}, \kappa_x = \frac{\partial \phi_x}{\partial x} \tag{2.3}$$

From Eqs. (2.2) and (2.3) we get the expression for the strain energy of the element shown in the Figure 2-1,

$$U = c_1 \left(\frac{\partial u_0}{\partial x} \right)^2 + c_2 \left(\frac{\partial \phi_z}{\partial x} \right)^2 + c_3 \left(\frac{\partial \phi_y}{\partial x} \right)^2 + c_4 \left(\frac{\partial v_0}{\partial x} - \phi_z \right)^2 + c_5 \left(\frac{\partial w_0}{\partial x} + \phi_y \right)^2 + c_6 \left(\frac{\partial \phi_x}{\partial x} \right)^2 \tag{2.4}$$

where,

$$\begin{aligned}
c_1 &= 3A_L E_L L_L \\
c_2 = c_3 &= \frac{1}{2} A_L E_L L_b^2 L_L \\
c_4 = c_5 &= \frac{6A_d A_L E_d E_L L_b^2 L_d L_L^2}{A_d E_d L_d L_L^3 + 4A_L E_L (L_b^2 + L_L^2)^2} \\
c_6 &= \frac{A_d A_L E_d E_L L_b^4 L_d L_L^2}{4 \left(A_d E_d L_d L_L^3 + A_L E_L (L_b^2 + L_L^2)^2 \right)}
\end{aligned} \tag{2.5}$$

Here A , L , E and ρ are the cross-sectional area, length, modulus of elasticity and the density of the pin-connected bar members, and the subscripts L , d and b refer to the longerons, diagonals and the battens in Figure 2-1. The strain energy expression in Eq. (2.4) is for a shearable model which is equivalent of a Timoshenko beam model. A simpler Euler Bernoulli equivalent model can be found by ignoring the shear strain terms in the strain energy as follow,

$$U = c_1 \left(\frac{\partial u_0}{\partial x} \right)^2 + c_2 \left(\frac{\partial^2 v_0}{\partial x^2} \right)^2 + c_3 \left(\frac{\partial^2 w_0}{\partial x^2} \right)^2 + c_6 \left(\frac{\partial \phi_x}{\partial x} \right)^2 \tag{2.6}$$

2.2 Kinetic Energy Derivations

As previously mentioned, the fundamental truss element in this study consists of the bar members shown in the Figure 2-2 with the radar panel mounted on the bottom. Since the radar panel mostly contains the electronic parts and is not made of a homogenous material, its elastic nature is complicated. Therefore in our formulation the strain energy stored in the panel is ignored, and the panel segments mounted on elements are modeled as additional masses. Also we assume that there is no connection between panel segments on adjacent elements. The kinetic energy of a bar member can be simply written in terms of its nodal velocities in the following form,

$$T = \frac{1}{6} \rho A l (V_{1x}^2 + V_{1y}^2 + V_{1z}^2 + V_{2x}^2 + V_{2y}^2 + V_{2z}^2 + V_{1x}V_{2x} + V_{1y}V_{2y} + V_{1z}V_{2z}) \quad (2.7)$$

where subscripts x, y, z show the velocity components along the Cartesian coordinates shown in Figure 2-2, and subscripts 1 and 2 refer to each of the two ends of the bar members (battens, longerons and diagonals) shown in Figure 2-3.

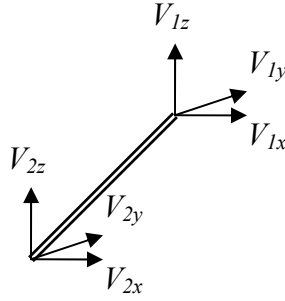


Figure 2-3 Nodal velocity components of a bar

Using Eq. (2.7) and the displacement components in Eq. (2.1) the kinetic energy of the bar member (k) in the truss element can be found as,

$$\begin{aligned} T_k = & \frac{1}{6} \rho_k A_k L_k \left(\left(\frac{\partial u_0}{\partial t} - y_{1,k} \frac{\partial \phi_z}{\partial t} + z_{1,k} \frac{\partial \phi_y}{\partial t} \right)^2 + \left(\frac{\partial v_0}{\partial t} - z_{1,k} \frac{\partial \phi_x}{\partial t} \right)^2 \right. \\ & + \left(\frac{\partial u_0}{\partial t} - y_{1,k} \frac{\partial \phi_z}{\partial t} + z_{1,k} \frac{\partial \phi_y}{\partial t} \right) \left(\frac{\partial u_0}{\partial t} - y_{2,k} \frac{\partial \phi_z}{\partial t} + z_{2,k} \frac{\partial \phi_y}{\partial t} \right) \\ & + \left(\frac{\partial w_0}{\partial t} + y_{1,k} \frac{\partial \phi_x}{\partial t} \right)^2 + \left(\frac{\partial u_0}{\partial t} - y_{2,k} \frac{\partial \phi_z}{\partial t} + z_{2,k} \frac{\partial \phi_y}{\partial t} \right)^2 \\ & + \left(\frac{\partial v_0}{\partial t} - z_{2,k} \frac{\partial \phi_x}{\partial t} \right)^2 + \left(\frac{\partial w_0}{\partial t} + y_{2,k} \frac{\partial \phi_x}{\partial t} \right)^2 \\ & + \left(\frac{\partial v_0}{\partial t} - z_{1,k} \frac{\partial \phi_x}{\partial t} \right) \left(\frac{\partial v_0}{\partial t} - z_{2,k} \frac{\partial \phi_x}{\partial t} \right) \\ & \left. + \left(\frac{\partial w_0}{\partial t} + y_{1,k} \frac{\partial \phi_x}{\partial t} \right) \left(\frac{\partial w_0}{\partial t} + y_{2,k} \frac{\partial \phi_x}{\partial t} \right) \right) \quad \text{where,} \quad k:1 \rightarrow 18 \end{aligned} \quad (2.8)$$

Here subscript k refers to each of the 18 bar members shown in Figure 2-1. Therefore, the total kinetic energy of the truss element can be found as,

$$T_{total} = \sum_{k=1}^{18} T_k = 3(A_b L_b \rho_b + A_d L_d \rho_d + A_L L_L \rho_L) \left(\left(\frac{\partial u_0}{\partial t} \right)^2 + \left(\frac{\partial v_0}{\partial t} \right)^2 + \left(\frac{\partial w_0}{\partial t} \right)^2 \right) + \frac{L_b^2 (A_b L_b \rho_b + A_d L_d \rho_d + 2A_L L_L \rho_L)}{4} \left(2 \left(\frac{\partial \phi_x}{\partial t} \right)^2 + \left(\frac{\partial \phi_y}{\partial t} \right)^2 + \left(\frac{\partial \phi_z}{\partial t} \right)^2 \right) \quad (2.9)$$

Note that the terms containing ϕ_y and ϕ_z (rotations of the cross section) are related to the rotatory inertia terms in a beam. It is shown later in this chapter that excluding these terms and the shear strains in the strain energy relation will result in a simpler model which is the same as an Euler-Bernoulli beam model. Next, consider the effects of adding a metrology panel to the ISAT like truss structure, running along the “bottom” side of the truss as indicated in Figure 1-1 by a shaded area. The function of the ISAT is measurement and the panel segments are radar devices which are simply modeled here as both plates and lumped masses as shown in Figures 2-4 and 2-5.

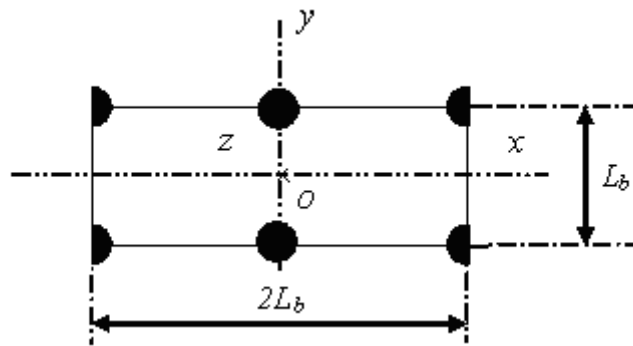


Figure 2-4 Radar panel modeled as lumped masses

Using Eq. (2.1) the kinetic energy of the panel can be found as,

$$\begin{aligned}
T_p = & \frac{m_p}{2} \left(\left(\frac{\partial u_0}{\partial t} + \frac{L_b}{2} \frac{\partial \phi_z}{\partial t} - \frac{L_b \sqrt{3}}{6} \frac{\partial \phi_y}{\partial t} \right)^2 + \left(\frac{\partial v_0}{\partial t} + \frac{L_b \sqrt{3}}{6} \frac{\partial \phi_x}{\partial t} \right)^2 + \left(\frac{\partial w_0}{\partial t} - \frac{L_b}{2} \frac{\partial \phi_x}{\partial t} \right)^2 \right) \\
& + \frac{m_p}{2} \left(\left(\frac{\partial u_0}{\partial t} - \frac{L_b}{2} \frac{\partial \phi_z}{\partial t} - \frac{L_b \sqrt{3}}{6} \frac{\partial \phi_y}{\partial t} \right)^2 + \left(\frac{\partial v_0}{\partial t} + \frac{L_b \sqrt{3}}{6} \frac{\partial \phi_x}{\partial t} \right)^2 + \left(\frac{\partial w_0}{\partial t} + \frac{L_b}{2} \frac{\partial \phi_x}{\partial t} \right)^2 \right)
\end{aligned} \tag{2.10}$$

where m_p is the mass of the panel distributed among the joints along one side,

$$m_p = \frac{m_{panel}}{2} \tag{2.11}$$

The expression (2.10) can be further simplified in the following form,

$$\begin{aligned}
T_p = & m_p \left(\left(\frac{\partial w_0}{\partial t} \right)^2 + \left(\frac{\partial u_0}{\partial t} \right)^2 + \left(\frac{\partial v_0}{\partial t} \right)^2 + \frac{\sqrt{3}}{3} L_b \frac{\partial v_0}{\partial t} \frac{\partial \phi_x}{\partial t} \right) \\
& + m_p \left(-\frac{\sqrt{3}}{3} L_b \frac{\partial u_0}{\partial t} \frac{\partial \phi_y}{\partial t} + \frac{L_b^2}{12} \left(4 \left(\frac{\partial \phi_x}{\partial t} \right)^2 + \left(\frac{\partial \phi_y}{\partial t} \right)^2 + 3 \left(\frac{\partial \phi_z}{\partial t} \right)^2 \right) \right)
\end{aligned} \tag{2.12}$$

The total kinetic energy of the truss element and the panel can be found using,

$$T = T_p + \sum_{k=1}^{18} T_k \tag{2.13}$$

A simpler model can be derived by ignoring the terms including the rotations of the cross section which is equivalent of an Euler-Bernoulli assumption. So we get,

$$\begin{aligned}
T = & \left(3(A_b L_b \rho_b + A_d L_d \rho_d + A_L L_L \rho_L) + m_p \right) \left(\left(\frac{\partial u_0}{\partial t} \right)^2 + \left(\frac{\partial v_0}{\partial t} \right)^2 + \left(\frac{\partial w_0}{\partial t} \right)^2 \right) \\
& + \left(\frac{L_b^2 (A_b L_b \rho_b + A_d L_d \rho_d + 2A_L L_L \rho_L)}{2} + m_p \frac{L_b^2}{3} \right) \left(\frac{\partial \phi_x}{\partial t} \right)^2 \\
& + m_p \left(\frac{\sqrt{3}}{3} L_b \frac{\partial v_0}{\partial t} \frac{\partial \phi_x}{\partial t} \right)
\end{aligned} \tag{2.14}$$

For the second kinetic energy model, the radar panel is modeled as a solid plate with a constant density. Figure 2-5 shows the bottom and the cross section view of the element and the panel. The kinetic energy of the plate can be written in terms of the velocity components of the center and the rotational velocities around the center, and we get,

$$T_p = \frac{1}{2} m_{\text{panel}} \left[\left(\frac{\partial u_0}{\partial t} - \frac{L_b \sqrt{3}}{6} \frac{\partial \phi_y}{\partial t} \right)^2 + \left(\frac{\partial v_0}{\partial t} + \frac{L_b \sqrt{3}}{6} \frac{\partial \phi_x}{\partial t} \right)^2 + \left(\frac{\partial w_0}{\partial t} \right)^2 \right] + \frac{1}{2} I_x \left(\frac{\partial \phi_x}{\partial t} \right)^2 + \frac{1}{2} I_y \left(\frac{\partial \phi_y}{\partial t} \right)^2 + \frac{1}{2} I_z \left(\frac{\partial \phi_z}{\partial t} \right)^2 \quad (2.15)$$

Here m_{panel} is the mass of the segment of the radar panel on a truss element. The mass moments of inertia I_x , I_y and I_z are measured around axes x, y, z and can be simply written as

$$I_x = \frac{m_{\text{panel}} L_b^2}{12} \quad I_y = \frac{m_{\text{panel}} L_b^2}{3} \quad I_z = \frac{5m_{\text{panel}} L_b^2}{12} \quad (2.16)$$

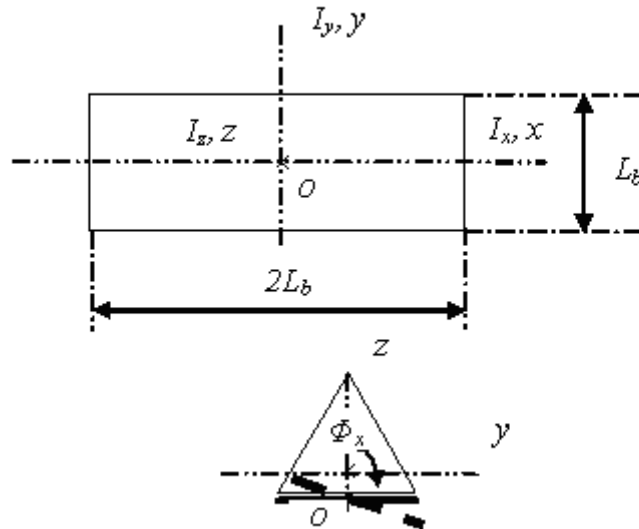


Figure 2-5 Schematic view of the structure cross-section and bottom view of the element

The relation in (2.15) can be further simplified in the form of,

$$\begin{aligned}
T_p = & \frac{m_{panel}}{2} \left(\left(\frac{\partial u_0}{\partial t} \right)^2 + \left(\frac{\partial v_0}{\partial t} \right)^2 + \left(\frac{\partial w_0}{\partial t} \right)^2 \right) + \frac{1}{2} I_x \left(\frac{\partial \phi_x}{\partial t} \right)^2 + \frac{1}{2} I_y \left(\frac{\partial \phi_y}{\partial t} \right)^2 + \frac{1}{2} I_z \left(\frac{\partial \phi_z}{\partial t} \right)^2 \\
& + \frac{L_b m_{panel}}{2\sqrt{3}} \left(\frac{\partial v_0}{\partial t} \frac{\partial \phi_x}{\partial t} - \frac{\partial u_0}{\partial t} \frac{\partial \phi_y}{\partial t} \right) + \frac{1}{24} L_b^2 m_{panel} \left(\left(\frac{\partial \phi_x}{\partial t} \right)^2 + \left(\frac{\partial \phi_y}{\partial t} \right)^2 \right)
\end{aligned} \tag{2.17}$$

Similarly, an Euler-Bernoulli kinetic energy expression can be found for the whole element by ignoring the effects of the rotatory inertia (rotations of the cross section). Therefore, we get,

$$\begin{aligned}
T = & 3(A_b L_b \rho_b + A_d L_d \rho_d + A_L L_L \rho_L) \left(\left(\frac{\partial u_0}{\partial t} \right)^2 + \left(\frac{\partial v_0}{\partial t} \right)^2 + \left(\frac{\partial w_0}{\partial t} \right)^2 \right) \\
& + \frac{L_b^2 (A_b L_b \rho_b + A_d L_d \rho_d + 2A_L L_L \rho_L)}{4} \left(2 \left(\frac{\partial \phi_x}{\partial t} \right)^2 \right) \\
& + \frac{1}{2} I_x \left(\frac{\partial \phi_x}{\partial t} \right)^2 + \frac{L_b m_{panel}}{2\sqrt{3}} \left(\frac{\partial v_0}{\partial t} \frac{\partial \phi_x}{\partial t} \right) + \frac{1}{24} L_b^2 m_{panel} \left(\left(\frac{\partial \phi_x}{\partial t} \right)^2 \right) \\
& + \frac{m_{panel}}{2} \left(\left(\frac{\partial u_0}{\partial t} \right)^2 + \left(\frac{\partial v_0}{\partial t} \right)^2 + \left(\frac{\partial w_0}{\partial t} \right)^2 \right)
\end{aligned} \tag{2.18}$$

2.3 Equations of Motion

As mentioned before, the structure under study has a repeated pattern, therefore, by having the kinetic and strain energy expressions of the truss element, Hamilton's principle can be used to find the equations of motion for the 6 coordinates of vibrations $\phi_x, \phi_y, \phi_z, u_0, v_0$ and w_0 . These displacement components are functions of x only and are the same as the displacement components of the equivalent 1-D continuum model. The equations of motion are derived for the truss-panel assembly and the truss without the panel using Timoshenko and Euler-Bernoulli formulations and for both kinetic energy models.

2.3.1 Lumped Mass Model

The equations of motion along the 6 coordinates of vibrations $u_0, v_0, w_0, \phi_x, \phi_y, \phi_z$ (longitudinal, bending, torsion and rotations of the cross section) for this model are presented in this section. Both effects of the shear strain and the rotatory inertia are included here which results in an equivalent Timoshenko type beam. As will be shown, these equations decouple in to two sets of equations for u_0, w_0, ϕ_y and v_0, ϕ_x, ϕ_z respectively. The coupling between these coordinates is shown in Figures 2-6 and 2-7. From Figure 2-6, it is clear that because of the asymmetry due to the addition of the mass at the bottom of the structure, the rotation of the cross section ϕ_y and the longitudinal vibrations are coupled. It is shown later in this chapter that for the truss with no panel there is no coupling between the longitudinal motion and the bending. The equations of motion for these coordinates can be found as,

$$\begin{cases} -2\sqrt{3}L_b m_p \frac{\partial^2 u_0}{\partial t^2} + 12c_5 \left(\frac{\partial w_0}{\partial x} + \phi_y \right) + \left(3L_b^2 (A_b L_b \rho_b + A_d L_d \rho_d + 2A_L L_L \rho_L) + L_b^2 m_p \right) \frac{\partial^2 \phi_y}{\partial t^2} - 12c_3 \frac{\partial^2 \phi_y}{\partial x^2} = 0 \\ \left(3(A_b L_b \rho_b + A_d L_d \rho_d + A_L L_L \rho_L) + m_p \right) \frac{\partial^2 w_0}{\partial t^2} - c_5 \frac{\partial^2 w_0}{\partial x^2} - c_5 \frac{\partial \phi_y}{\partial x} = 0 \\ - \left(m_p + 3(A_b L_b \rho_b + A_d L_d \rho_d + A_L L_L \rho_L) \right) \frac{\partial^2 u_0}{\partial t^2} + c_1 \frac{\partial^2 u_0}{\partial x^2} + \frac{\sqrt{3}}{6} L_b m_p \frac{\partial^2 \phi_y}{\partial t^2} = 0 \end{cases} \quad (2.19)$$

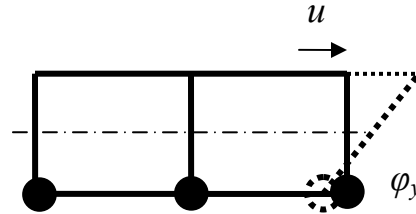


Figure 2-6 Coupled longitudinal and bending motion for the truss panel assembly

Figure 2-7 depicts the coupling of the torsional mode with the bending in the y direction. For the three coordinates v_0, Φ_x, Φ_z shown in Figure 2-7, we get,

$$\left\{ \begin{aligned} & \left(6m_p + 18(A_b L_b \rho_b + A_d L_d \rho_d + A_L L_L \rho_L) \right) \frac{\partial^2 v_0}{\partial t^2} + \sqrt{3} L_b m_p \frac{\partial^2 \phi_x}{\partial t^2} + 6c_4 \left(\frac{\partial \phi_z}{\partial x} - \frac{\partial^2 v_0}{\partial x^2} \right) = 0 \\ & \sqrt{3} L_b m_p \frac{\partial^2 v_0}{\partial t^2} + \left(3L_b^2 (A_b L_b \rho_b + A_d L_d \rho_d + 2A_L L_L \rho_L) + 2L_b^2 m_p \right) \frac{\partial^2 \phi_x}{\partial t^2} - 6c_6 \frac{\partial^2 \phi_x}{\partial x^2} = 0 \\ & \left(L_b^2 (A_b L_b \rho_b + A_d L_d \rho_d + 2A_L L_L \rho_L) + L_b^2 m_p \right) \frac{\partial^2 \phi_z}{\partial t^2} - 4c_2 \frac{\partial^2 \phi_z}{\partial x^2} + 4c_4 \left(\phi_z - \frac{\partial v_0}{\partial x} \right) = 0 \end{aligned} \right. \quad (2.20)$$

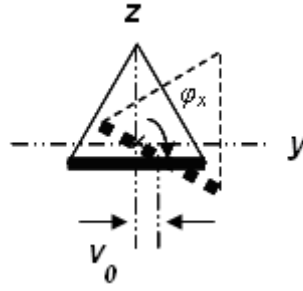


Figure 2-7 Coupled torsional and bending motion for the truss panel assembly

A simpler formulation can be found by ignoring the effects of rotatory inertia (i.e., by excluding the rotations of the cross-sections Φ_y and Φ_z in the kinetic energy terms as well as the shear strain components in the strain energy or,

$$\varepsilon_{xy} = \varepsilon_{xz} = \varepsilon_{yz} = 0 \quad (2.21)$$

Therefore, the Euler-Bernoulli equations of motion for this structure for this kinetic energy model are,

$$\begin{cases}
\left(3(A_b L_b \rho_b + A_d L_d \rho_d + A_L L_L \rho_L) + 2m_p\right) \frac{\partial^2 u_0}{\partial t^2} - 3A_L E_L L_L \frac{\partial^2 u_0}{\partial x^2} = 0 \\
2\left(3(A_b L_b \rho_b + A_d L_d \rho_d + A_L L_L \rho_L) + 2m_p\right) \frac{\partial^2 w_0}{\partial t^2} + A_L E_L L_b^2 L_L \frac{\partial^4 w_0}{\partial x^4} = 0 \\
-2L_b \left(3A_b L_b \rho_b + 3A_d L_d \rho_d + 6A_L L_L \rho_L + 4m_p\right) \frac{\partial^2 \phi_x}{\partial t^2} + \frac{3A_d A_L E_d E_L L_b^3 L_L^2 L_d}{A_d E_d L_L^3 L_d + A_L E_L L_d^4} \frac{\partial^2 \phi_x}{\partial x^2} - 4\sqrt{3}m_p \frac{\partial^2 v_0}{\partial t^2} = 0 \\
4m_p \left(\frac{\sqrt{3}}{2} L_b \frac{\partial^2 \phi_x}{\partial t^2} + 3 \frac{\partial^2 v_0}{\partial t^2}\right) + 3 \left(6(A_b L_b \rho_b + A_d L_d \rho_d + A_L L_L \rho_L) \frac{\partial^2 v_0}{\partial t^2} + A_L E_L L_b^2 L_L \frac{\partial^4 v_0}{\partial x^4}\right) = 0
\end{cases} \quad (2.22)$$

2.3.2 Plate Model

Using Hamilton's principle, the equations of motion for the plate model can also be found. The equations of motion along 3 coordinates of vibrations u_0, w_0, ϕ_y are:

$$\begin{cases}
-\left(6m_{panel} + 36(A_b L_b \rho_b + A_d L_d \rho_d + A_L L_L \rho_L)\right) \frac{\partial^2 u_0}{\partial t^2} + 12c_1 \frac{\partial^2 u_0}{\partial x^2} + \sqrt{3}L_b m_{panel} \frac{\partial^2 \phi_y}{\partial t^2} = 0 \\
-\sqrt{3}L_b m_{panel} \frac{\partial^2 u_0}{\partial t^2} + 12c_5 \left(\frac{\partial w_0}{\partial x} + \phi_y\right) + 3 \left(L_b^2 (A_b L_b \rho_b + A_d L_d \rho_d + 2A_L L_L \rho_L) + \frac{5L_b^2 m_{panel}}{6}\right) \frac{\partial^2 \phi_y}{\partial t^2} - 12c_3 \frac{\partial^2 \phi_y}{\partial x^2} = 0 \\
\left(6(A_b L_b \rho_b + A_d L_d \rho_d + A_L L_L \rho_L) + m_{panel}\right) \frac{\partial^2 w_0}{\partial t^2} - 2c_5 \left(\frac{\partial^2 w_0}{\partial x^2} + \frac{\partial \phi_y}{\partial x}\right) = 0
\end{cases} \quad (2.23)$$

and for the other 3 coordinates v_0, Φ_x, Φ_z we have:

$$\begin{cases}
6\left(6(A_b L_b \rho_b + A_d L_d \rho_d + A_L L_L \rho_L) + m_{panel}\right) \frac{\partial^2 v_0}{\partial t^2} - 12c_4 \frac{\partial^2 v_0}{\partial x^2} + \sqrt{3}L_b m_{panel} \frac{\partial^2 \phi_x}{\partial t^2} + 12c_4 \frac{\partial \phi_z}{\partial x} = 0 \\
2\sqrt{3}L_b m_{panel} \frac{\partial^2 v_0}{\partial t^2} + \left(12\left(I_x + L_b^2 (A_b L_b \rho_b + A_d L_d \rho_d + 2A_L L_L \rho_L)\right) + L_b^2 m_{panel}\right) \frac{\partial^2 \phi_x}{\partial t^2} - 24c_6 \frac{\partial^2 \phi_x}{\partial x^2} = 0 \\
-\left(I_z + \frac{L_b^2 (A_b L_b \rho_b + A_d L_d \rho_d + 2A_L L_L \rho_L)}{2}\right) \frac{\partial^2 \phi_z}{\partial t^2} + 2c_2 \frac{\partial^2 \phi_z}{\partial x^2} + 2c_4 \left(\frac{\partial v_0}{\partial x} - \phi_z\right) = 0
\end{cases} \quad (2.24)$$

Equations (2.19) and (2.23) are identical to the bending equation of motion for the anisotropic Timoshenko beam theory. The conventional Timoshenko beam theory was derived for

homogenous isotropic materials. For the case of an orthotropic material a more general form of this theory is required in which the bending and rotation of the cross section are coupled with the longitudinal motion. For the structure in this study, this coupling occurs because of the addition of the panel which induces an asymmetry on the mass distribution for the structure. Finally, for the simpler form of these equations (Euler-Bernoulli equivalent model) we get,

$$\left\{ \begin{array}{l} \left(6(A_b L_b \rho_b + A_d L_d \rho_d + A_L L_L \rho_L) + m_{panel} \right) \frac{\partial^2 u_0}{\partial t^2} - 6A_L E_L L_L \frac{\partial^2 u_0}{\partial x^2} = 0 \\ \left(6(A_b L_b \rho_b + A_d L_d \rho_d + A_L L_L \rho_L) + m_{panel} \right) \frac{\partial^2 w_0}{\partial t^2} + A_L E_L L_b^2 L_L \frac{\partial^4 w_0}{\partial x^4} = 0 \\ m_{panel} \left(\sqrt{3} L_b \frac{\partial^2 \phi_x}{\partial t^2} + 6 \frac{\partial^2 v_0}{\partial t^2} \right) + 6 \left(6(A_b L_b \rho_b + A_d L_d \rho_d + A_L L_L \rho_L) \frac{\partial^2 v_0}{\partial t^2} + A_L E_L L_b^2 L_L \frac{\partial^4 v_0}{\partial x^4} \right) = 0 \\ L_b \left(A_b L_b \rho_b + A_d L_d \rho_d + 2A_L L_L \rho_L + \frac{m_{panel}}{6} \right) \frac{\partial^2 \phi_x}{\partial t^2} - \frac{A_d A_L E_d E_L L_b^3 L_L^2 L_d}{2(A_d E_d L_L^3 L_d + A_L E_L L_d^4)} \frac{\partial^2 \phi_x}{\partial x^2} + \frac{\sqrt{3} m_{panel}}{6} \frac{\partial^2 v_0}{\partial t^2} = 0 \end{array} \right. \quad (2.25)$$

In an Euler-Bernoulli beam model it is assumed that the cross section remains perpendicular to the neutral axis, therefore the rotations of the cross section are dependent coordinates of vibrations and are identical to the bending slopes in the y and z directions. Therefore, this formulation does not contain the rotational terms. Also, bending in the z direction (i.e., perpendicular to the panel surface) and the longitudinal coordinate remain identical for the two kinetic energy models. This is expected because the rotation of the cross section Φ_y is the only term in the set of coupled coordinates u_0, w_0, Φ_y that is accounted for differently in the two kinetic energy expressions. This is shown more clearly using the relation for the difference between these two kinetic energy expressions as,

$$T_{(plate)} - T_{(mp)} = \frac{1}{6} L_b^2 m_p \left(-\phi_x^2 + 2\phi_y^2 + \phi_z^2 \right)$$

Therefore, by eliminating the coordinate Φ_y , the equations of motion for u_0 , w_0 , Φ_y coordinates will be identical for both models. The bending coordinate v_0 will be different for the two kinetic energy models though. This is because the v_0 coordinate is coupled with both Φ_z and Φ_x . So even though the rotation of the cross section Φ_z is neglected in the Euler Bernoulli assumptions, the two kinetic energy models for the Euler Bernoulli formulation will still be different because of their coupling with the coordinate Φ_x which is included in the derivations.

2.4 Truss Structure (No Panel)

For the case of the truss with no panel the equations of motion take a simpler form. Because of the mass symmetry and the symmetric pattern of the diagonal members, there is no coupling between the longitudinal or the torsional vibration and the bending coordinates. The equations of motion for the two bending coordinates v_0 and w_0 are identical. Equation (2.19) for the coordinates Φ_y , w_0 , reduces to the form:

$$\begin{cases} -(A_b L_b \rho_b + A_d L_d \rho_d + 2A_L L_L \rho_L) \frac{\partial^2 \phi_y}{\partial t^2} - A_L E_L L_L \left(\frac{24A_d E_d L_d L_L}{A_d E_d L_d L_L^3 + 4A_L E_L (L_b^2 + L_L^2)} \left(\phi_y + \frac{\partial w_0}{\partial x} \right) - 2 \frac{\partial^2 \phi_y}{\partial x^2} \right) = 0 \\ -(A_b L_b \rho_b + A_d L_d \rho_d + A_L L_L \rho_L) \frac{\partial^2 w_0}{\partial t^2} + \frac{2A_d A_L E_d E_L L_b^2 L_d L_L^2}{A_d E_d L_d L_L^3 + 4A_L E_L (L_b^2 + L_L^2)} \left(\frac{\partial^2 w_0}{\partial x^2} + \frac{\partial \phi_y}{\partial x} \right) = 0 \end{cases} \quad (2.26)$$

and for the Φ_z, v_0 we get the following,

$$\begin{cases} -(A_b L_b \rho_b + A_d L_d \rho_d + 2A_L L_L \rho_L) \frac{\partial^2 \phi_z}{\partial t^2} - A_L E_L L_L \left(\frac{24A_d E_d L_d L_L}{A_d E_d L_d L_L^3 + 4A_L E_L (L_b^2 + L_L^2)} \left(\phi_z - \frac{\partial v_0}{\partial x} \right) - 2 \frac{\partial^2 \phi_z}{\partial x^2} \right) = 0 \\ -(A_b L_b \rho_b + A_d L_d \rho_d + A_L L_L \rho_L) \frac{\partial^2 v_0}{\partial t^2} + \frac{2A_d A_L E_d E_L L_b^2 L_d L_L^2}{A_d E_d L_d L_L^3 + 4A_L E_L (L_b^2 + L_L^2)} \left(\frac{\partial^2 v_0}{\partial x^2} - \frac{\partial \phi_z}{\partial x} \right) = 0 \end{cases} \quad (2.27)$$

The equations for the torsional and longitudinal coordinates decouple from the bending equations for the truss. These equations have a form similar to those of a bar in tension or torsion as,

$$\frac{2L_b(A_bL_b\rho_b + A_dL_d\rho_d + 2A_L L_L \rho_L)}{L_L} \frac{\partial^2 \phi_x}{\partial t^2} = \frac{A_d A_L E_d E_L L_b^3 L_d L_L}{A_d E_d L_d L_L^3 + A_L E_L (L_b^2 + L_L^2)^2} \frac{\partial^2 \phi_x}{\partial x^2} \quad (2.28)$$

$$(A_b L_b \rho_b + A_d L_d \rho_d + A_L L_L \rho_L) \frac{\partial^2 u_0}{\partial t^2} = A_L E_L L_L \frac{\partial^2 u_0}{\partial x^2} \quad (2.29)$$

As shown in the above, the equations for the bending and the rotations of the cross section are coupled. Following the procedure presented in the Appendix B, these equations can be decoupled and presented in the following form:

$$\begin{aligned} \eta \frac{\partial^4 w_0}{\partial t^4} + \alpha \frac{\partial^4 w_0}{\partial x^4} + \gamma \frac{\partial^2 w_0}{\partial t^2} + \xi \frac{\partial^4 w_0}{\partial t^2 \partial x^2} &= 0 \\ \eta \frac{\partial^4 v_0}{\partial t^4} + \alpha \frac{\partial^4 v_0}{\partial x^4} + \gamma \frac{\partial^2 v_0}{\partial t^2} + \xi \frac{\partial^4 v_0}{\partial t^2 \partial x^2} &= 0 \end{aligned} \quad (2.30)$$

It is clear that equations in (2.30) are of the same form as the bending vibrations for a Timoshenko beam. Using this similarity, equations for these coefficients can be found in terms of the material and geometrical properties of longerons, battens and diagonals as follow:

$$\begin{aligned} \eta &= \frac{\rho_{eq}^2 I_{eq.}}{\kappa_{eq}^2 G_{eq.}} = \frac{(A_b L_b \rho_b + A_d L_d \rho_d + 2A_L L_L \rho_L)(A_b L_b \rho_b + A_d L_d \rho_d + A_L L_L \rho_L)}{(A_L E_L + A_b E_b + A_d E_d)} \\ \alpha &= E_{eq.} I_{eq.} = \frac{4A_d A_L^2 E_d E_L^2 L_b^2 L_d L_L^3}{\left(A_d E_d L_d L_L^3 + 4A_L E_L (L_b^2 + L_L^2)^2 \right) (A_L E_L + A_b E_b + A_d E_d)} \\ \gamma &= \rho_{eq.} A_{eq.} = \frac{24A_d E_d L_d L_L^2 A_L E_L (A_b L_b \rho_b + A_d L_d \rho_d + A_L L_L \rho_L)}{\left(A_d E_d L_d L_L^3 + 4A_L E_L (L_b^2 + L_L^2)^2 \right) (A_L E_L + A_b E_b + A_d E_d)} \\ \xi &= -\rho_{eq.} I_{eq.} \left(1 + \frac{E_{eq.}}{\kappa_{eq.}^2 G_{eq.}} \right) = -\frac{2A_d A_L E_d E_L L_b^2 L_d L_L^2 (A_b L_b \rho_b + A_d L_d \rho_d + 2A_L L_L \rho_L)}{\left(A_d E_d L_d L_L^3 + 4A_L E_L (L_b^2 + L_L^2)^2 \right) (A_L E_L + A_b E_b + A_d E_d)} \\ &\quad - \frac{2(A_b L_b \rho_b + A_d L_d \rho_d + A_L L_L \rho_L) A_L E_L L_L}{(A_L E_L + A_b E_b + A_d E_d)} \end{aligned} \quad (2.31)$$

where subscript *eq.* denotes the properties for the equivalent continuum model. These relations provide a simple tool for comparing the dynamic characteristics of lattices with various material and geometrical properties. It is worthwhile to note that the material and geometrical properties for an equivalent model are not unique.

For the diagonal pattern shown in Figure 2-1, the coefficients c_2 and c_3 (the bending stiffness terms in the y and z direction) are identical; so are the coefficients c_4 and c_5 (the shear stiffness). As a result of this equivalence, the bending equations for v_0 and w_0 in Eqs. (2.26) to Eq. (2.27) are similar. Also, note that there is a sign difference for the rotation of the cross section terms (ϕ_y and ϕ_z) in these equations; this is simply because of the sign convention for the coordinates of vibration. Following the procedure presented in the Appendix B the decoupled equations are identical for both bending coordinates.

2.5 PDE Solution

The partial differential equations of motion for each of the two sets of coordinates of vibration can be easily found using the approach by Sun et. al.²² Following this approach we assume a harmonic solution for the coupled coordinates of vibrations. The solution presented here pertains to the u_0 , w_0 and Φ_y . A similar approach is taken to find the solution for the other coordinates. We have,

$$\left. \begin{aligned} u_0 &= U e^{\alpha x} e^{i\omega t} \\ w_0 &= W e^{\alpha x} e^{i\omega t} \\ \phi_y &= \Omega e^{\alpha x} e^{i\omega t} \end{aligned} \right\} \Rightarrow \begin{Bmatrix} u_0 \\ w_0 \\ \phi_y \end{Bmatrix} = \begin{Bmatrix} U \\ W \\ \Omega \end{Bmatrix} e^{\alpha x} e^{i\omega t} \quad (2.32)$$

where U , W , and Ω are the amplitudes of vibration, α is the mode shape parameter, and ω is the natural frequency. Making the substitution for Eq. (2.32) in (2.19), we get the following eigenvalue problem,

$$\underbrace{\begin{bmatrix} -a_5\omega^2 & a_3\alpha & a_3 + a_4\alpha^2 - a_1\omega^2 \\ 0 & -a_3\alpha^2 - a_2\omega^2 & -a_3\alpha \\ a_6\alpha^2 - a_2\omega^2 & 0 & -a_5\omega^2 \end{bmatrix}}_H \begin{Bmatrix} U \\ W \\ \Omega \end{Bmatrix} = 0 \quad (2.33)$$

where,

$$\begin{aligned} a_1 &= 2L_b^2 \left(3(A_b L_b \rho_b + A_d L_d \rho_d + 2A_L L_L \rho_L) + m_p \right) \\ a_2 &= 24 \left(3(A_b L_b \rho_b + A_d L_d \rho_d + A_L L_L \rho_L) + m_p \right) \\ a_3 &= \frac{144 A_d A_L E_d E_L L_b^2 L_d L_L^2}{A_d E_d L_d L_L^3 + 4 A_L E_L (L_b^2 + L_L^2)^2} \\ a_4 &= -12 A_L E_L L_b^2 L_L \\ a_5 &= -4\sqrt{3} m_p L_b \\ a_6 &= -72 A_L E_L L_L \end{aligned} \quad (2.34)$$

For a nontrivial solution the determinant of the matrix H should vanish, i.e.,

$$\text{Det}(H) = 0 \Rightarrow K_1 \alpha^6 + K_2 \alpha^4 + K_3 \alpha^2 + K_4 = 0 \quad (2.35)$$

where,

$$\begin{aligned} K_1 &= a_3 a_4 a_6 \\ K_2 &= (-a_2 a_3 a_4 - a_1 a_3 a_6 + a_2 a_4 a_6) \omega^2 \\ K_3 &= a_2 a_3 a_6 \omega^2 + (a_1 a_2 a_3 - a_2^2 a_4 - a_3 a_5^2 - a_1 a_2 a_6) \omega^4 \\ K_4 &= -a_2^2 a_3 \omega^4 + (a_1 a_2^2 - a_2 a_5^2) \omega^6 \end{aligned} \quad (2.36)$$

The above equation is a cubic polynomial in α^2 and the roots of this polynomial can be found in terms of the natural frequencies ω . Therefore, for each frequency ω , we have 6 roots of α_i . Also from (2.33), the solution for the mode vectors can be expressed in the form,

$$\begin{aligned}
U_i &= \begin{vmatrix} a_3\alpha_i & a_3 + a_4\alpha_i^2 - a_1\omega^2 \\ -a_3\alpha_i^2 - a_2\omega^2 & -a_3\alpha_i \end{vmatrix} \\
&= a_3a_4\alpha_i^4 + a_2a_3\omega^2 - a_1a_3\alpha_i^2\omega^2 + a_2a_4\alpha_i^2\omega^2 - a_1a_2\omega^4 \\
W_i &= - \begin{vmatrix} -a_5\omega^2 & a_3 + a_4\alpha_i^2 - a_1\omega^2 \\ 0 & -a_3\alpha_i \end{vmatrix} = -a_3a_5\alpha_i\omega^2 \\
\Omega_i &= \begin{vmatrix} -a_5\omega^2 & a_3\alpha_i \\ 0 & -a_3\alpha_i^2 - a_2\omega^2 \end{vmatrix} = a_3a_5\alpha_i^2\omega^2 + a_2a_5\omega^4 \quad i: 1 \rightarrow 6
\end{aligned} \tag{2.37}$$

The vibration solution can be expanded in terms of the mode vectors and the natural frequencies in the following form,

$$\begin{Bmatrix} u_0(x,t) \\ w_0(x,t) \\ \phi_y(x,t) \end{Bmatrix} = \sum_{j=1}^6 d_j \begin{Bmatrix} U_j \\ W_j \\ \Omega_j \end{Bmatrix} e^{\alpha_j x} e^{i\omega t} \tag{2.38}$$

where the constants d_j (modal contribution factors) and the frequencies are found from the boundary conditions. A free-free boundary condition for this structure requires that,

$$\begin{bmatrix} N(0,t) \\ Q_z(0,t) \\ M_y(0,t) \end{bmatrix} = \begin{bmatrix} N(L_t,t) \\ Q_z(L_t,t) \\ M_y(L_t,t) \end{bmatrix} = \begin{bmatrix} 0 \\ 0 \\ 0 \end{bmatrix} \tag{2.39}$$

where N , Q_z , and M_y are the longitudinal force, shear force in z direction and the bending moment around the y axis. Using the relation for the strain energy, Eq. (2.4), the stiffness matrix for an element can be easily found and the force-displacement relation for an element can be written as,

$$\begin{bmatrix} N \\ Q_y \\ Q_z \\ M_z \\ M_y \\ M_x \end{bmatrix} = \frac{1}{2L_L} \underbrace{\begin{bmatrix} c_1 & 0 & 0 & 0 & 0 & 0 \\ 0 & c_2 & 0 & 0 & 0 & 0 \\ 0 & 0 & c_3 & 0 & 0 & 0 \\ 0 & 0 & 0 & c_4 & 0 & 0 \\ 0 & 0 & 0 & 0 & c_5 & 0 \\ 0 & 0 & 0 & 0 & 0 & c_6 \end{bmatrix}}_K \begin{bmatrix} \frac{\partial u_0}{\partial x} \\ -\phi_z + \frac{\partial v_0}{\partial x} \\ \phi_y + \frac{\partial w_0}{\partial x} \\ \frac{\partial \phi_z}{\partial x} \\ \frac{\partial \phi_y}{\partial x} \\ \frac{\partial \phi_x}{\partial x} \end{bmatrix} \quad (2.40)$$

From (2.38), (2.39) and (2.40), we get 6 linear algebraic equations that can be written in a matrix form,

$$[f(\omega)]\{d_j\} = 0 \quad (2.41)$$

A nontrivial solution requires that,

$$|f(\omega)| = 0 \quad (2.42)$$

The solution to (2.42) results in the natural frequencies for this structure for the free-free boundary condition.

2.6 Frequencies and Wavelengths

It is interesting to find the errors of the frequency estimations with respect to their wavelengths. Because the torsional, bending and the longitudinal waves travel at different speeds, the wavelength of the frequency of interest is different for the same frequency values for each of these coordinates. The equivalent beam model for this structure provides a simple tool to find the wave speeds for different coordinates. For example, the relation for the bending wave speed, a dispersive wave, is given by,

$$c = 4 \sqrt{\frac{E_{eq} \cdot I_{eq}}{\rho_{eq} \cdot A_{eq}}} \cdot \sqrt{\omega} = 4 \sqrt{\frac{A_L E_L L_b^2 L_L}{6(A_b L_b \rho_b + A_d L_d \rho_d + A_L L_L \rho_L)}} \sqrt{2\pi f} \quad (2.43)$$

for the longitudinal wave (a non-dispersive wave) speed we get,

$$c = \sqrt{\frac{A_L E_L L_L}{(A_b L_b \rho_b + A_d L_d \rho_d + A_L L_L \rho_L)}} \quad (2.44)$$

and the relation for the torsional wave speed (non-dispersive) can be written as,

$$c = \sqrt{\frac{A_d A_L E_d E_L L_b^2 L_d L_L^2}{2(A_b L_b \rho_b + A_d L_d \rho_d + 2A_L L_L \rho_L)(A_d E_d L_d L_L^3 + A_L E_L L_d^4)}} \quad (2.45)$$

where f is the frequency in (Hz). Using the above and knowing the relation for the frequency and wavelength ($\lambda=c/f$), the wavelengths for frequencies of different coordinates of vibrations can be found which are presented in the following section.

2.7 Numerical Results

An equivalent beam-like continuum model, and the governing partial differential equations of motion are found for both structures (with and without panel) in this study. A finite element model was developed in MATLAB to validate the accuracy of the natural frequencies for the continuum model. Material and geometrical properties for this structure are presented in Table 2-1. A comparison of the natural frequencies for the Timoshenko, Euler-Bernoulli, and the FEM for different coordinates of vibration are presented in Tables 2-2 to 2-5 for the structure with the mounted radar panel. The results for the truss without the panel are also shown in Tables 2-6 to 2-8. Two kinetic energy models are presented to account for the inertia effects of the panel. As shown the equivalent Timoshenko model has better accuracy in predicting the natural frequencies when compared to the Euler-Bernoulli. In the Euler-Bernoulli model, the shear strains are ignored, which is equivalent to making the assumption that the shear modulus is equal

to infinity. Therefore, the stiffness is always overestimated in this model which results in overestimating the frequencies. This is particularly more noticeable for the higher mode numbers and is shown to be the case for both structures (truss-panel and the truss w/o panel). For the (W_0, U_0, Φ_y) coordinates, the average error of the Timoshenko model is 0.57 % for both kinetic energy models and for the (V_0, Φ_x, Φ_z) , this error is about 1.58%. While, for the Euler-Bernoulli model the value is 17.17%. For the truss (no panel) the average error is 0.96% for the Timoshenko model and 8.07% for the Euler-Bernoulli.

As it is shown in Tables 2-2 to 2-5, the natural frequencies are very close for the two sets of coordinates (V_0, Φ_x, Φ_z) and (W_0, U_0, Φ_y) for lower frequencies and this difference grows for the higher modes; whereas, for the truss without the panel, these frequencies are the same. This is because the symmetry of the structure is lost due to the added panel and therefore the frequencies of the bending coordinates deviate from each other which are more noticeable for the higher modes. Also, it is shown that the frequencies of the (V_0, Φ_x, Φ_z) coordinates change more significantly due to the addition of the panel, and therefore their frequencies are lower compared to the (W_0, U_0, Φ_y) frequencies for both kinetic energy models. Moreover, from the relations for the two kinetic energy models, it can be seen that the kinetic energy term related to the coordinate Φ_y is bigger for the plate model compared to the lumped mass model. As a result, the natural frequencies for the coupled coordinates (W_0, U_0, Φ_y) is smaller for this model. Additionally, in the lumped mass model, the mass of the panel is distributed along the edges. This will result in overestimating the kinetic energy term due to torsion, therefore the frequencies for this coordinate are underestimated compared to the plate model. Figure 2-13 shows a comparison for the torsional frequencies of these two models.

It is also interesting to examine the frequency estimations with respect to their wavelengths. The results for the frequency estimations with respect to the wavelengths are plotted in Figures 2-8 to 2-11 and 2-15 for both structures. As it can be observed the error gets larger for the smaller wavelengths. This is because the error is related to the wavelength to element span ratio. As the frequency of interest increases, the wavelength decreases and the numbers of truss elements in the span of a wavelength decreases; this results in a higher error. It should be noted that because different coordinates of vibration travel at different speeds, the wavelengths for the same frequency values for the torsional, longitudinal and the bending modes are also different. This is shown clearly in Figures 2-8 to 2-11 where the longitudinal and the torsional modes have higher wavelengths.

In the Euler-Bernoulli model the coordinates Φ_y and Φ_z are ignored, hence, there will be no difference between the kinetic energy terms for the $(W_\theta, U_\theta, \Phi_y)$ and these two models. Therefore, the frequencies are the same which is clear from the results shown in Tables 2-2 and 2-3. Finally, for both structures the longitudinal frequencies are larger than both the torsional and bending frequencies which is expected for the large length of the structure.

Table 2-2 Natural frequencies of the lumped mass model for bending, longitudinal, and rotation of the cross section (W_0, U_0, Φ_y) in (rad/sec)

FEM	Timoshenko	Error%	Euler-Ber.	Error%
0	0	0	0	0
0.4633	0.4604	0.6259	0.4621	0.2590
1.2646	1.2567	0.6247	1.2737	0.7196
2.4425	2.4272	0.6264	2.4970	2.2313
3.9587	3.9343	0.6164	4.1277	4.2691
5.7737	5.7380	0.6183	6.1661	6.7963
7.8445	7.7974	0.6004	8.6122	9.7865
10.1287	10.0687	0.5924	11.4659	13.2021
12.5860	12.5165	0.5522	14.7274	17.0141
15.1802	15.0895	0.5975	18.3965	21.1875
16.3500 ^L	15.8940 ^L	2.7890 ^L	15.8933 ^L	2.7933 ^L
17.8796	17.7986	0.4530	22.4733	25.6924
20.6570	20.5828	0.3592	26.9577	30.5015
23.4899	23.4209	0.2937	31.8498	35.5893
26.3596	26.3152	0.1684	37.1497	40.9342
29.2511	29.2238	0.0933	42.8572	46.5148

Table 2-3 Natural frequencies of the solid panel model for bending, longitudinal, and rotation of the cross section (W_0, U_0, Φ_y) in (rad/sec)

FEM	Timoshenko	Error%	Euler-Ber.	Error%
0	0	0	0	0
0.4634	0.4600	0.7337	0.4621	0.2590
1.2644	1.2547	0.7672	1.2737	0.7196
2.4406	2.4210	0.8031	2.4970	2.2313
3.9524	3.9200	0.8198	4.1277	4.2691
5.7587	5.7110	0.8283	6.1661	6.7963
7.8149	7.7530	0.7921	8.6122	9.7865
10.0768	10.0026	0.7363	11.4659	13.2021
12.5026	12.4254	0.6175	14.7274	17.0141
15.0541	14.9729	0.5394	18.3965	21.1875
16.3540 ^L	15.8919 ^L	2.8256 ^L	15.8933 ^L	2.7933 ^L
17.6976	17.6515	0.2605	22.4733	25.6924
20.4036	20.4072	0.0176	26.9577	30.5015
23.1472	23.2172	0.3024	31.8498	35.5893
25.9071	26.0849	0.6863	37.1497	40.9342
28.6657	28.9695	1.0598	42.8572	46.5148

Table 2-4 Natural frequencies of the lumped mass model for bending, torsional, and rotation of the cross section (V_0, Φ_x, Φ_z) in (rad/sec)

FEM	Timoshenko	Error%	Euler-Ber.	Error%
0	0	0	0	0
0.4628	0.4595	0.7131	0.4614	0.3025
1.2572	1.2480	0.7318	1.2657	0.6761
2.1883 ^T	2.1267 ^T	2.8150 ^T	2.1269 ^T	2.8058 ^T
2.4111	2.3926	0.7673	2.4623	2.1235
3.8714	3.8396	0.8214	4.0239	3.9391
4.3839 ^T	4.2617 ^T	2.7875 ^T	4.2638 ^T	2.7396 ^T
5.5834	5.5334	0.8955	5.9151	5.9408
6.5920 ^T	6.4124 ^T	2.7245 ^T	6.4245 ^T	2.5410 ^T
7.4924	7.4172	1.0037	8.0795	7.8359
8.8151 ^T	8.5858 ^T	2.6012 ^T	8.6303 ^T	2.0964 ^T
9.5497	9.4388	1.1613	10.4355	9.2757
11.0531 ^T	10.7878 ^T	2.4002 ^T	10.9103 ^T	1.2919 ^T
11.7173	11.5557	1.3792	12.8912	10.0185
13.2972 ^T	13.0155 ^T	2.1185 ^T	13.2978 ^T	0.0045 ^T
13.9759	13.7456	1.6478	15.3719	9.9886

Table 2-5 Natural frequencies of the solid panel model for bending, torsional, and rotation of the cross section (V_0, Φ_x, Φ_z) in (rad/sec)

FEM	Timoshenko	Error%	Euler-Ber.	Error%
0	0	0	0	0
0.4630	0.4593	0.7991	0.4614	0.3456
1.2583	1.2475	0.8583	1.2662	0.6278
2.4144	2.3920	0.9278	2.4650	2.0958
3.4073 ^T	3.3119 ^T	2.7999 ^T	3.3128 ^T	2.7735 ^T
3.8827	3.8440	0.9967	4.0374	3.9843
5.5954	5.5365	1.0527	5.9380	6.1229
6.8379 ^T	6.6498 ^T	2.7508 ^T	6.6615 ^T	2.5797 ^T
7.5165	7.4361	1.0696	8.1637	8.6104
9.5880	9.4865	1.0586	10.0349	4.6610
10.2790 ^T	10.0035 ^T	2.6802 ^T	10.6558 ^T	3.6657 ^T
11.7728	11.6534	1.0142	13.3713	13.5779
13.6530 ^T	13.3401 ^T	2.2918 ^T	13.4713 ^T	1.3308 ^T
14.1314	13.9593	1.2179	16.2639	15.0905
16.2021	16.0510	0.9326	16.9874	4.8469
17.3992 ^T	16.9964 ^T	2.3150 ^T	19.2925 ^T	10.8815 ^T

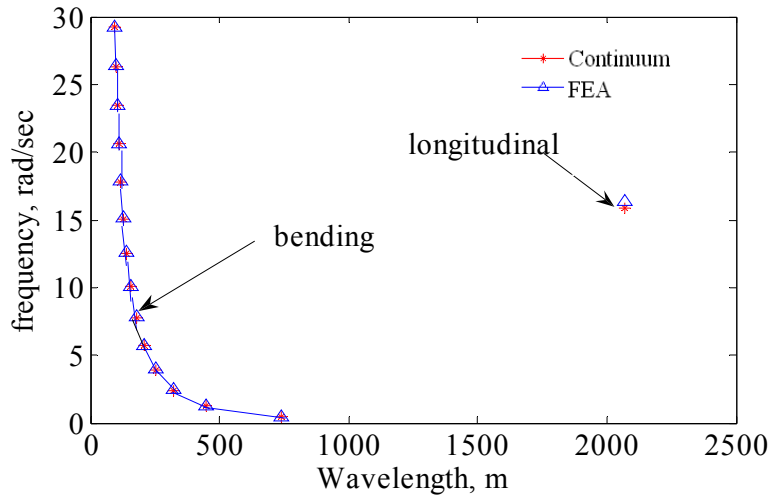


Figure 2-8 Natural frequencies of the lumped mass model (W_0, U_0, Φ_y) (FEM, blue-Continuum, red)

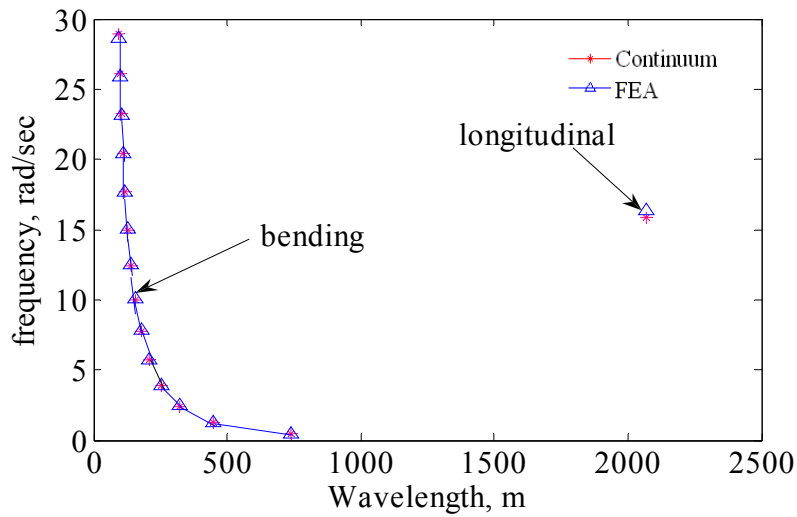


Figure 2-9 Natural frequencies of the solid panel model (W_0, U_0, Φ_y) (FEM, blue-Continuum, red)

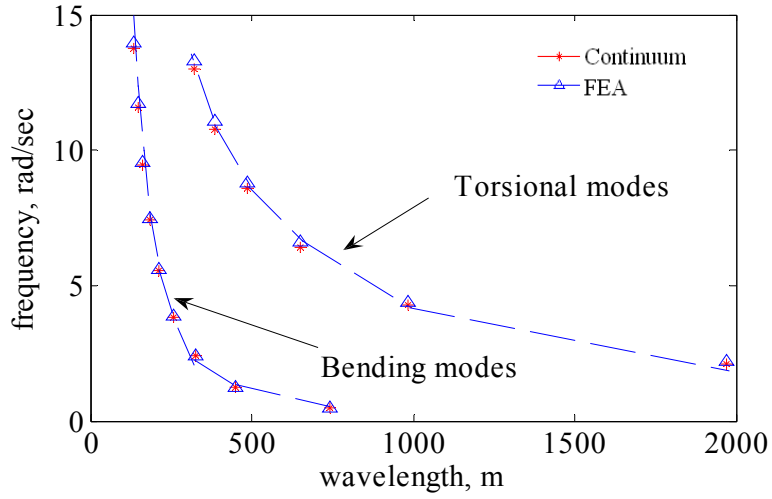


Figure 2-10 Natural frequencies of the lumped mass model (V_θ, Φ_x, Φ_z) (FEM, blue-Continuum, red)

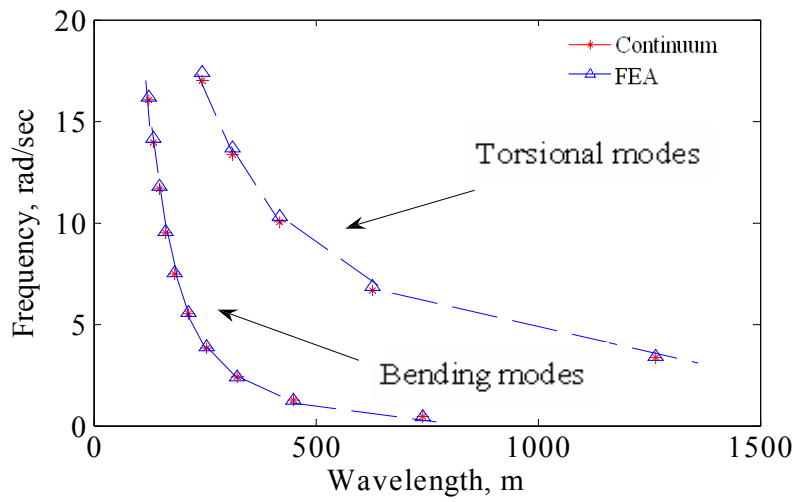


Figure 2-11 Natural frequencies of the solid panel model (V_θ, Φ_x, Φ_z) (FEM, blue-Continuum, red)

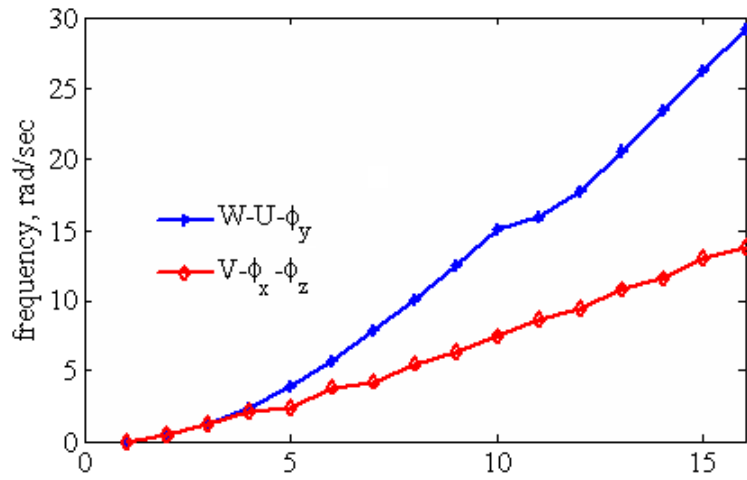


Figure 2-12 Comparison of the frequencies of lumped mass model for (V_0, Φ_x, Φ_z) and (W_0, U_0, Φ_y)

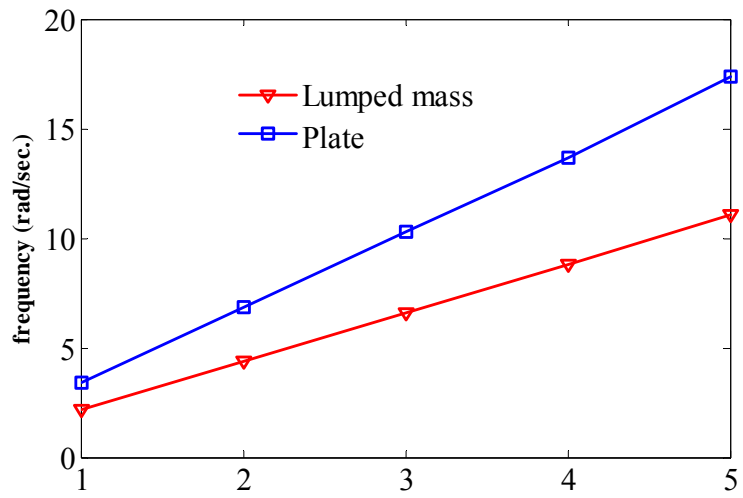


Figure 2-13 Comparison of the torsional frequency for the lumped mass and plate model

Table 2-6 Natural frequencies of the truss w/o panel for bending in (rad/sec)

FEM	Timoshenko	Error%	Euler-Ber.	Error%
0	0	0	0	0
1.5959	1.5852	0.6693	1.5915	0.2756
4.3580	4.3272	0.7065	4.3869	0.6632
8.4207	8.3573	0.7536	8.6004	2.1340
13.6559	13.5409	0.8420	14.2176	4.1134
19.9309	19.7468	0.9237	21.2384	6.5603
27.1044	26.8279	1.0200	29.6642	9.4441
35.0363	34.6417	1.1262	39.4923	12.7183
43.5940	43.0543	1.2381	50.7260	16.3602
52.6600	51.9462	1.3554	63.3634	20.3255

Table 2-7 Longitudinal natural frequencies of the truss w/o panel (rad/sec)

FEM	Continuum model
0	0
56.3332	54.7391
112.6770	109.4782
169.0422	164.2236
225.4388	218.9627
281.8781	273.7081
338.3703	328.4472
394.9258	383.1863
451.5549	437.9317
508.2689	492.6708

Table 2-8 Torsional natural frequencies of the truss w/o panel (rad/sec)

FEA	Continuum model
0	0
7.1817	6.9743
14.3571	13.9487
21.5388	20.9293
28.7267	27.9036
35.9147	34.8780
43.1027	41.8586
50.3032	48.8329
57.5037	55.8073
64.7105	62.7879

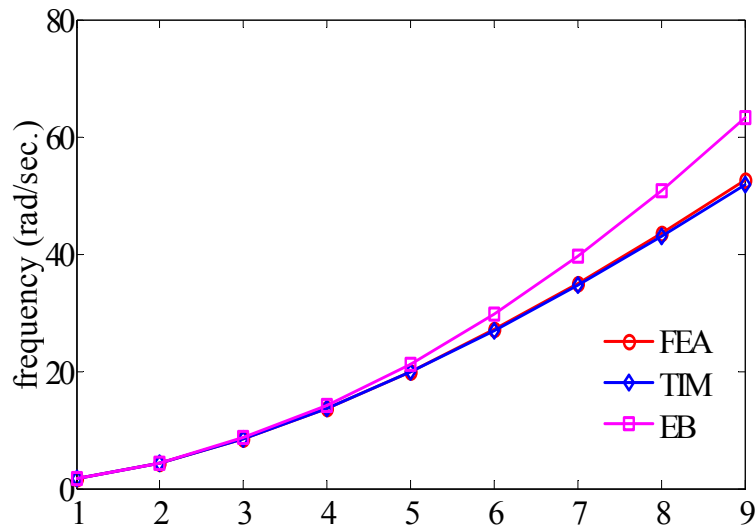


Figure 2-14 Bending frequencies of the Timoshenko, FEM and the Euler Bernoulli model of the truss w/o panel

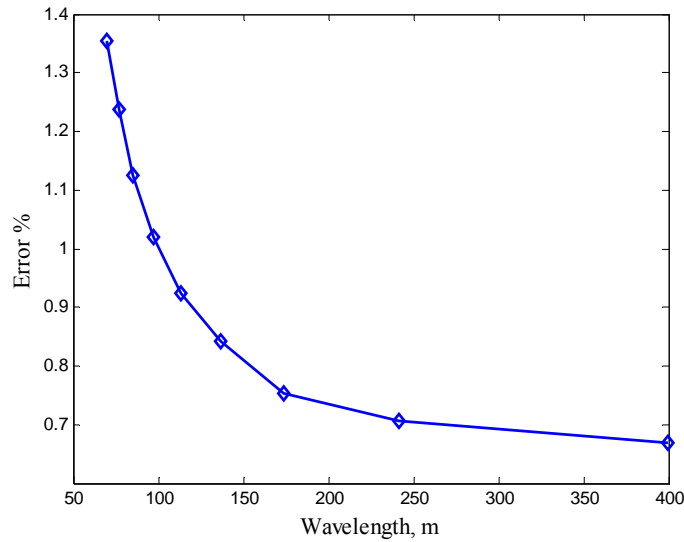


Figure 2-15 Error in frequency estimations with respect to the wavelength for the truss w/o panel

2.8 Conclusion

A continuum modeling approach is presented for a structure which consists of repeated lattice elements supporting a radar panel. The governing partial differential equations of motion are derived for both the truss-panel assembly and the truss with no panel. Two kinetic energy models are suggested to account for the mass of the radar panel. In the first the mass of the panel is distributed among the bottom joints and in second, each segment of the panel is modeled as a solid plate with a constant density. The strain energy of the panel is ignored. Finally two equivalent continuum beam models are derived for the structure under study: Timoshenko equivalent and the Euler-Bernoulli equivalent. It is shown that as a result of the addition of the panel the symmetry of the structure is lost; therefore the torsional and the longitudinal coordinates of vibration are coupled with bending. The equations of motion have a form similar to an anisotropic Timoshenko beam theory. For the case of the truss with no panel, the bending equations of the equivalent model are similar to those of a conventional Timoshenko beam. The torsional

and longitudinal equations of motion for this structure decouple from the other coordinates and they are similar to the equations for a bar member. The material and geometrical properties of the equivalent continuum model can be found by comparing the coefficients in the equations of motion of the truss with those of a Timoshenko type beam. This provides a simple tool for comparing dynamic characteristics of lattices with different properties. The results for these models are compared to a standard FEM of the structure for the purpose of validation. The results for the continuum model are in good agreement with the FEM (within 2% error) and the CPU usage is 180 times less than the FEM. In addition, the reduced order continuum model provides an analytical solution that allows simplicity and physical insight into the structural mechanics and the dominant physics of the structure.

Chapter 3

Model Experimental Validation

3.1 Introduction

This chapter presents an experimental validation of the homogenization method described in the previous chapter. Due to the laboratory limitations a small scale metal planar truss (approximately 2 meters long) with Pratt Girder configuration⁴⁵ was built and tested. The assumptions for the strain and displacement field developed for a three-dimensional truss structure are modified and presented in a suitable form for the planar truss. Similar to the previous chapter the local effects for the fundamental element (variations of the strain values across the element) are included using a Taylor series expansion. Similar assumptions for reducing the strain states for this element are employed. This test structure is then used to validate the proposed method. The frequency response functions and the natural frequencies are found using the model and the experiment for comparison.



Figure 3-1 An inflatable rigidized boom

3.2 Equations of Motion

The structure studied in this work is a planar truss with Pratt Girder configuration. A schematic of the repeating element, joints and their interconnecting parts are shown in Figs. 3-2 and 3-3, respectively. The truss element consists of the shaded area shown in Fig. 3-2 and the remaining areas belong to the adjacent elements. The members in the truss element are modeled as bars with pin joints. Therefore, similar to the outlined derivation for the 3-D structure in Chapter 1, we assume linear variations for the displacement components (u, w) along the z axis around the center of the cross section.

For a planar truss the displacement field takes the following form:

$$\begin{aligned} u(x, z) &= u_0(x) + z\phi_y(x) \\ w(x, z) &= w_0(x) + z\varepsilon_z(x) \end{aligned} \quad (3.1)$$

Finally, the kinetic and strain energy expressions for the repeating element are found and the assumptions for the shear deformation type beam is made to solve for the strain

components in the 2-D structure is terms of the strains components in the 1-D beam type continuum. A complete derivation for the kinetic and strain energy expressions is presented in the Appendix C. Similarly, Hamilton's principle is employed to find the governing partial differential equations of motion for the 1-D model. These equations are then written in the form of an eigenvalue problem to solve for the Frequency Response Functions (FRF) and the natural frequencies of the system.

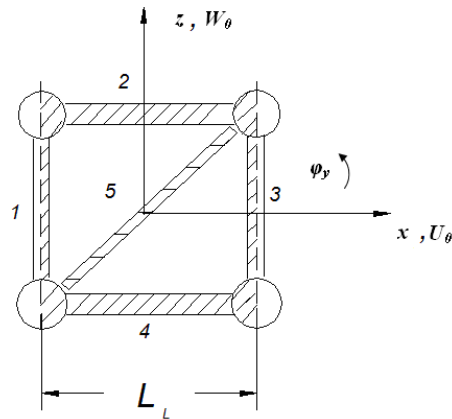


Figure 3-2 Schematic of bar members and joints in a truss element

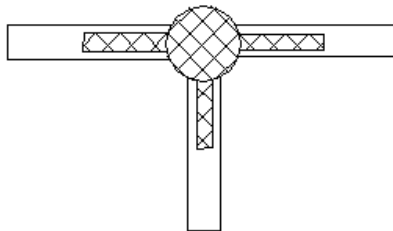


Figure 3-3 A view of the joint and the interconnecting parts

The equations of motion for this structure can be found in the following form:

$$\begin{cases} c_1 \left(\phi_y + \frac{\partial w_0}{\partial x} + \frac{\partial u_0}{\partial x} \right) + c_3 \frac{\partial^2 \phi_y}{\partial x^2} + c_4 \frac{\partial^2 \phi_y}{\partial t^2} = 0 \\ c_2 \frac{\partial^2 w_0}{\partial t^2} + c_5 \left(\frac{\partial \phi_y}{\partial x} + \frac{\partial^2 w_0}{\partial x^2} + \frac{\partial^2 u_0}{\partial x^2} \right) = 0 \\ c_2 \frac{\partial^2 u_0}{\partial t^2} + c_5 \left(\frac{\partial^2 w_0}{\partial x^2} + \frac{\partial \phi_y}{\partial x} \right) + c_6 \frac{\partial^2 u_0}{\partial x^2} = 0 \end{cases} \quad (3.2)$$

where,

$$\begin{aligned} c_1 &= 12A_d E_d L_d A_L E_L L_L \\ c_2 &= (3A_L L_L \rho_L + L_d A_d \rho_d + 2m_j)(A_d E_d L_d + 4A_L E_L L_L) \\ c_3 &= -6L_L^2 (A_d E_d L_d + 4A_L E_L L_L) A_L E_L L_L \\ c_4 &= L_L^2 (7A_L L_L \rho_L + 6m_j + L_d A_d \rho_d)(A_d E_d L_d + 4A_L E_L L_L) \\ c_5 &= -E_d A_d L_d A_L E_L L_L \\ c_6 &= -E_L A_L L_L (3E_d A_d L_d + 8E_L A_L L_L) \end{aligned} \quad (3.3)$$

where the displacement components $u_0(x)$, $w_0(x)$ and $\phi_y(x)$ are the longitudinal, bending and the rotation of the cross section respectively and are all evaluated at the center of the truss element. The symbol m_j represents the mass of the joints and the subscripts L , d and b refer to longerons, diagonals and battens respectively. This relation has a form similar to the anisotropic Timoshenko beam theory, a more general form of the ordinary Timoshenko beam equation.

3.3 Boundary Conditions

3.3.1 Mass and Moment of Inertia

As mentioned previously, the fundamental repeating truss element consists of the shaded area shown in the Figure 3-2; the remaining parts in the figure belong to the adjacent elements. Therefore, when assembling the 9 elements along the length of the structure, the two end parts shown in the Fig. 3-4 do not belong to any of these elements. These are

included as the boundary conditions for this structure. For the force and moment relation at the boundaries of this structure we get the following,

at $x=0$:

$$N(x,t) = m_b \frac{\partial^2 u_0(x,t)}{\partial t^2}, \quad Q_z(x,t) = m_b \frac{\partial^2 w_0(x,t)}{\partial t^2}, \quad M_y(x,t) = I_b \frac{\partial^2 \phi_y(x,t)}{\partial t^2} \quad (3.4-a)$$

at $x=L$:

$$N(x,t) = -m_b \frac{\partial^2 u_0(x,t)}{\partial t^2}, \quad Q_z(x,t) = -m_b \frac{\partial^2 w_0(x,t)}{\partial t^2}, \quad M_y(x,t) = -I_b \frac{\partial^2 \phi_y(x,t)}{\partial t^2} \quad (3.4-b)$$

Here m_b and I_b are the mass and the mass moment of inertia at the boundaries and N , Q_z and M_y are the longitudinal, shear force and the bending moment respectively. Failure to consider these at the boundary condition represents a flaw of the other previously published methods for lattice structures with repeated patterns. Figure 3-12 depicts a comparison between the FRFs without including the boundary conditions and the results from experiment. The figure clearly shows the non-negligible difference between the theory and the experiment. To include the effect of the boundaries, the stiffness matrix of the element is found in Eq. (3.5). The force-displacement relation at these boundaries can be found as,

$$\begin{bmatrix} N \\ Q_z \\ M_y \end{bmatrix} = L_L \underbrace{\begin{bmatrix} \frac{A_L E_L L_L (3A_d E_d L_d + 8A_L E_L L_L)}{L_L (A_d E_d L_d + 4A_L E_L L_L)} & \frac{A_L E_L L_L A_d E_d L_d}{L_L (A_d E_d L_d + 4A_L E_L L_L)} & 0 \\ \frac{A_L E_L L_L A_d E_d L_d}{L_L (A_d E_d L_d + 4A_L E_L L_L)} & \frac{A_L E_L L_L A_d E_d L_d}{L_L (A_d E_d L_d + 4A_L E_L L_L)} & 0 \\ 0 & 0 & \frac{A_L E_L L_L^2 (A_d E_d L_d + 4A_L E_L L_L)}{2(A_d E_d L_d + 4A_L E_L L_L)} \end{bmatrix}}_{\hat{K}} \begin{bmatrix} \frac{\partial u_0}{\partial x} \\ \phi_y + \frac{\partial w_0}{\partial x} \\ \frac{\partial \phi_y}{\partial x} \end{bmatrix} \quad (3.5)$$

Following the approach in Chapter 2 and using Eqs. (3.4) and (3.5) these equations can be written in the form of six linear algebraic equations in terms of the frequencies and the modal contribution factors as,

$$[g(\omega)]\{d_j\} = 0 \quad (3.6)$$

To get a nontrivial solution the following should hold,

$$|g(\omega)| = 0 \quad (3.7)$$

Finally, the solution of the above equation provides the natural frequencies of this structure.

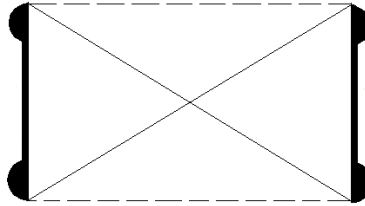


Figure 3-4 Boundaries of the planar truss

3.3.2 Strings at Boundaries

The structure was tested in a configuration hung from strings. To include the strings at the boundary conditions of the system a very simple single degree of freedom model for this structure is used. The transfer function for the translational mode of the truss is found using the second order system. Note that for the case that the stiffness of the strings is

zero this mode is equivalent of a rigid body mode. Figure 3-5 shows a schematic of the mass-stiffness system for this structure.

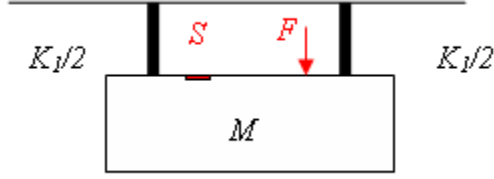


Figure 3-5 Schematic of the truss and the wires

The transfer function of the translational mode can be found using the relation,

$$X(s) = \frac{F(s)}{Ms^2 + K_1} \quad (3.8)$$

Assuming a linear system, the summation of this transfer function and the FRF for the distributed parameter system in a free-free boundary condition gives us the frequency response function of the system with strings at the boundaries.

3.4 Effect of Strain Variations on Kinetic Energy

A complete derivation for the kinetic energy of the element is presented in the Appendix C. In the original derivation, the strain values are ignored in the displacement components. For the case that the strain components are included in the kinetic energy expression, we get

$$T_e = \frac{1}{2} (3A_L \rho_L L_L + A_d \rho_d L_d + 2m_j) \left(\left(\frac{\partial u_0}{\partial t} \right)^2 + \left(\frac{\partial w_0}{\partial t} \right)^2 \right) + \frac{1}{24} L_L^2 (7A_L \rho_L L_L + A_d \rho_d L_d + 6m_j) \left(\frac{\partial \phi_y}{\partial t} \right)^2$$

$$+ \underbrace{\frac{(A_d E_d L_L L_d)^2}{24(A_d E_d L_d + 4A_L E_L L_L)^2} (7A_L \rho_L L_L + A_d \rho_d L_d + 6m_j) \left(\left(\frac{\partial^2 u_0}{\partial x \partial t} \right)^2 + \left(\frac{\partial^2 w_0}{\partial x \partial t} \right)^2 + \left(\frac{\partial \phi_y}{\partial t} \right)^2 \right)}_{\text{kinetic energy term related to the strain components}}$$

$$(3.9)$$

Using Hamilton's principle, the equations of motion for the system can be found as follows:

$$\begin{cases} c_1 \left(\phi_y + \frac{\partial w_0}{\partial x} + \frac{\partial u_0}{\partial x} \right) + c_3 \frac{\partial^2 \phi_y}{\partial x^2} + c_4 \frac{\partial^2 \phi_y}{\partial t^2} + c_7 \left(\frac{\partial^3 w_0}{\partial x \partial t^2} + \frac{\partial^3 u_0}{\partial x \partial t^2} + \frac{\partial^2 \phi_y}{\partial t^2} \right) = 0 \\ 12c_5 \left(\frac{\partial \phi_y}{\partial x} + \frac{\partial^2 w_0}{\partial x^2} + \frac{\partial^2 u_0}{\partial x^2} \right) + 12c_2 \frac{\partial^2 w_0}{\partial t^2} - c_7 \left(\frac{\partial^4 w_0}{\partial x^2 \partial t^2} + \frac{\partial^4 u_0}{\partial x^2 \partial t^2} + \frac{\partial^3 \phi_y}{\partial x \partial t^2} \right) = 0 \\ 12c_5 \left(\frac{\partial^2 w_0}{\partial x^2} + \frac{\partial \phi_y}{\partial x} \right) + 12c_2 \frac{\partial^2 u_0}{\partial t^2} + 12c_6 \frac{\partial^2 u_0}{\partial x^2} - c_7 \left(\frac{\partial^4 w_0}{\partial x^2 \partial t^2} + \frac{\partial^4 u_0}{\partial x^2 \partial t^2} + \frac{\partial^3 \phi_y}{\partial x \partial t^2} \right) = 0 \end{cases} \quad (3.10)$$

where the coefficients c_1 to c_6 are given in the Eq. (3.3). The inclusion of the strain values results in the terms with the coefficient c_7 as,

$$c_7 = \frac{(E_d A_d L_d L_L)^2}{(E_d A_d L_d + 4E_L A_L L_L)} (7A_L L_L \rho_L + \rho_d A_d L_d + 6m_j) \quad (3.11)$$

Finally, following the previous section the natural frequencies of the system are found and presented in Table-4.

3.5 Wavelengths and Frequencies

The natural frequencies from this model are compared with the values from the experiment as shown in the following sections. It is also interesting to examine the error in the frequency estimations with respect to the wavelengths. Using the PDE for this system the material and geometrical properties of the equivalent continuum model can be found. So we get,

$$\frac{E_{eq} I_{eq.}}{\rho_{eq.} A_{eq.}} = \frac{L_L^2 A_L E_L L_L}{2(3A_L L_L \rho_L + 2m_j + L_d A_d \rho_d)} \quad (3.12)$$

The bending wave speed can then be found as,

$$c = \sqrt[4]{\frac{E_{eq} I_{eq.}}{\rho_{eq} A_{eq.}}} \sqrt{\omega} \Rightarrow c = \sqrt[4]{\frac{L_L^2 A_L E_L L_L}{2(3A_L L_L \rho_L + 2m_j + L_d A_d \rho_d)}} \sqrt{\omega} \quad (3.13)$$

Finally, the wavelength for each frequency component has the following form,

$$\lambda = \sqrt[4]{\frac{L_L^2 A_L E_L L_L}{2(3A_L L_L \rho_L + 2m_j + L_d A_d \rho_d)}} \sqrt{\frac{2\pi}{f}} \quad (3.14)$$

where f is the frequency in (Hz).

3.6 Experimental Setup

This section presents the experimental setup for testing a two-dimensional laboratory truss to provide some element of validation for the concept of our homogenization method. The structure under test consists of 9 truss elements shown in Fig. 3-2. Each truss element is made of tubular bars and threaded aluminum ball joints as illustrated in Fig. 3-3. The longeron members are made of aluminum tubes and the diagonals are made of steel rods. Figure 3-6 depicts a schematic of the experiment with sensor and actuator locations. The truss structure was hung on wires from the ceiling at its ends. The truss dimensions are 1960 mm \times 217.6 mm. Other structural properties such as density and modulus of longerons and diagonals are provided in Tables 3-1 and 3-2.

To validate the results of the continuum model, the natural frequencies and the frequency response functions were obtained experimentally. Figure 3-7 shows a photo of the experimental setup. The setup includes the truss structure, a Windows 98 PC with Matlab 6.0, a Piezotron coupler model Kistler 5122, a SIGLAB unit 20-42 DSP data acquisition Board (V3.2), an accelerometer (PCB PIEZOTRONICS Model 352C22) with a sensitivity of 1 mV/(m/s²), a shaker, a high voltage amplifier model TREK 50/750 and a force transducer model 208 A SN 841 with a sensitivity of 112.410 V/KN. A chirp signal

of the frequency range of 1-500 (Hz) is used as an input excitation to this structure. This signal is provided by the SIGLAB unit which is fed to the shaker after passing through the amplifier. The resultant input force to the structure is then measured by the force transducer which is attached to the shaker. The accelerometer is used to measure the acceleration of measurement points in the truss. The PZT sensor in the accelerometer and the force transducer produce a charge and the impedance converter in these elements convert this charge to a voltage signal that can easily be measured. On the other hand the impedance converter requires a voltage and a current to operate. The Piezotron coupler is used to supply this current and voltage to the accelerometer and the force transducer. The data collected by the accelerometer and the force transducer was fed into the SigLab DSP Board which is a signal-processing plug-in compatible with MATLAB. Finally the ratio of the force and acceleration gives us the frequency response functions for the measurement points. ME'scopeVES (Visual Engineering Series) version 4.0 by Vibrant Technology Inc. is employed to plot the experimental mode shapes. A plot of the experimental mode shapes are presented in Figs. 3-8.

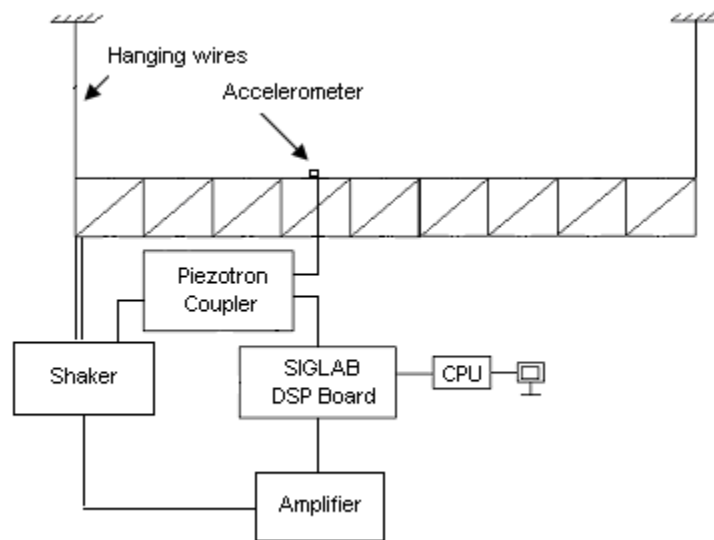


Figure 3-6 Schematic of the experimental setup

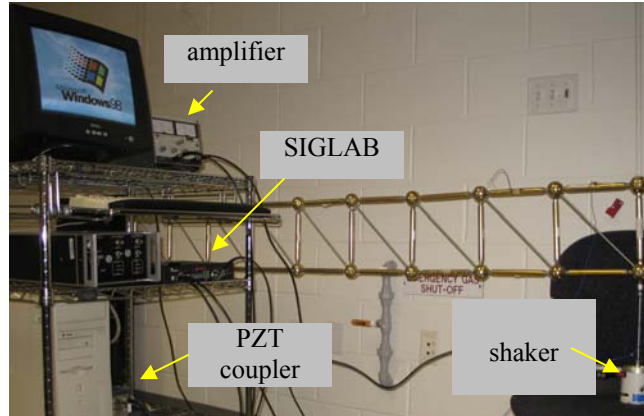


Figure 3-7 Photo of the experimental setup

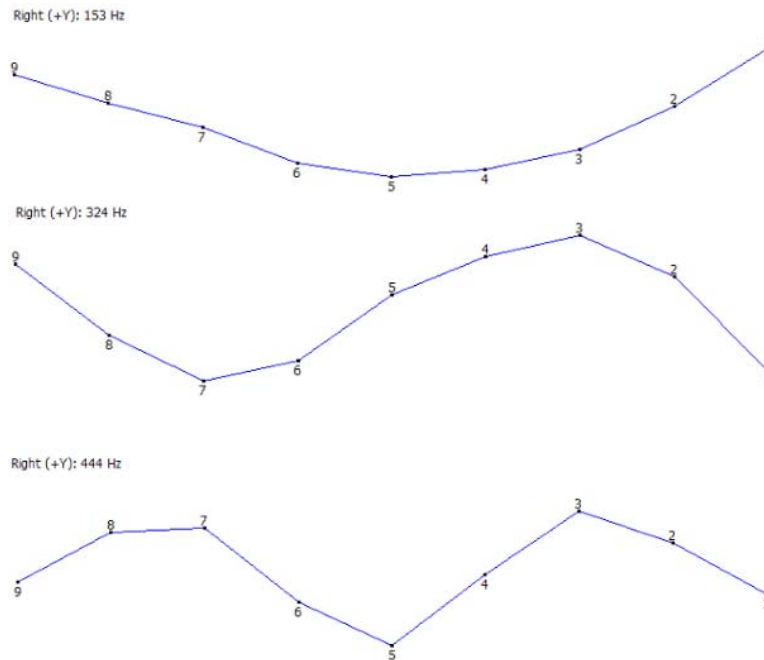


Figure 3-8 Animation snapshots of the experimental mode shapes

3.7 Numerical Results and Discussion

The experimental natural frequencies are found using the peak-peak method⁵³ and the results for the theory and the experiment are presented in Tables 3-3 and 3-4. The errors in the estimation of the first 4 natural frequencies (0-500 Hz) are 0.07%, 0.65%, 1.5% and 9.2%, respectively. Figure 3-9 shows the frequency response function, coherence and

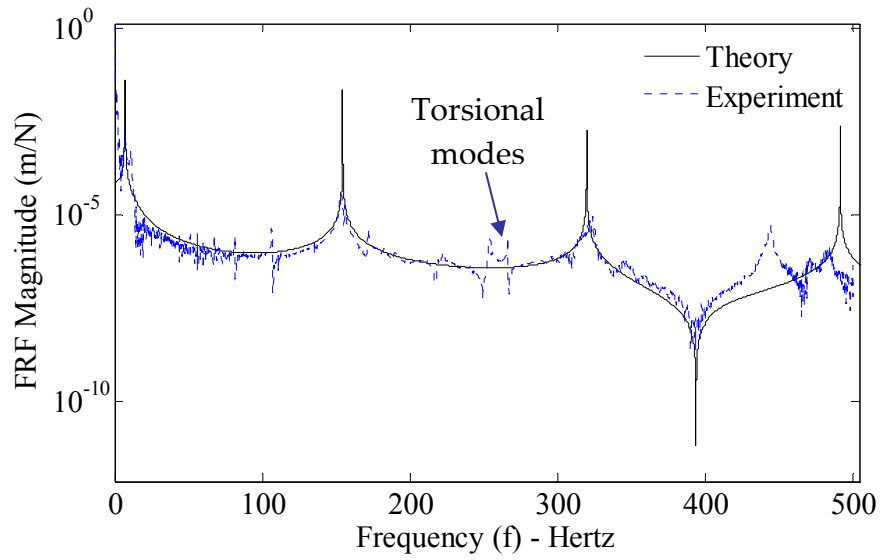
the phase plots from the experiment. Since the strings at the boundaries have a finite stiffness (a stiffness value of 4.5 kg/cm), the structure has a very small fundamental frequency around 7 (Hz) which is related to the translational mode of the truss. The second, third and the fourth natural frequencies are also shown in Figure 3-9. The two modes shown in the figure around the 250 (Hz) are related to the out of plane torsional modes, which are not estimated by the theory. Because we model the structure as a truss with hinge joints there would be no stiffness in the out of plane motion; i.e, the structure can fold but not bend in the y direction. The fact that these are the torsional modes has been tested by looking at the imaginary parts of the frequency response functions shown in Figure 3-9b. As shown in this figure the imaginary part of the frequency response functions around 250 (Hz) is very small. This clearly shows that the peaks around this frequency are related to the out of plane modes which are measured in a direction different from the accelerometer measurements. Therefore the accelerometer does not completely capture these peaks. Also, to assure these are the torsional modes and therefore, the peak around the 324 (Hz) is the second bending mode, snapshots of the experimental mode shapes using the ME'scopeVES software are presented in Fig. 3-8. As demonstrated in this figure the mode shape around the frequency of 324 (Hz) has clearly the form of the second bending mode shape. This confirms that neither of the two small peaks around the 250 (Hz) can be the second mode. Fig. 3-10 shows a comparison between the theoretical frequency response functions plots with and without including the effects of the strings at the boundaries. From the figure, this effect is more noticeable and needs to be included for the lowest frequency. However, the higher frequencies (i.e., the second, third and the fourth modes) do not change in this model. This is because the

translational mode in this structure is well separated from the vibrational modes. To account for the effect of the strings we consider that the mass of the truss is held by wires with very small stiffness (a single degree of freedom model) which results in a very small natural frequency for the equivalent mass-stiffness system (truss and the strings). This frequency has a very small value (≈ 7 Hz) which is clearly shown in the figure. Fig. 3-11 shows a comparison between the frequency response functions plots for the experiment and the theory for the case that the effects of the strings at the boundary conditions are not included. It is also clear from this figure that this effect needs to be included to obtain results in better agreement with the experiment. Also a comparison between the FRF from the theory and experiment when no mass and no strings are included at the boundaries (free-free) are presented in Fig. 3-12. As shown in this figure, ignoring the mass at the boundaries results in a significant discrepancy between the theory and experiment which indicates the importance of including the boundary conditions in the form presented in the section 2.4 (a flaw of the previously published methods)²².

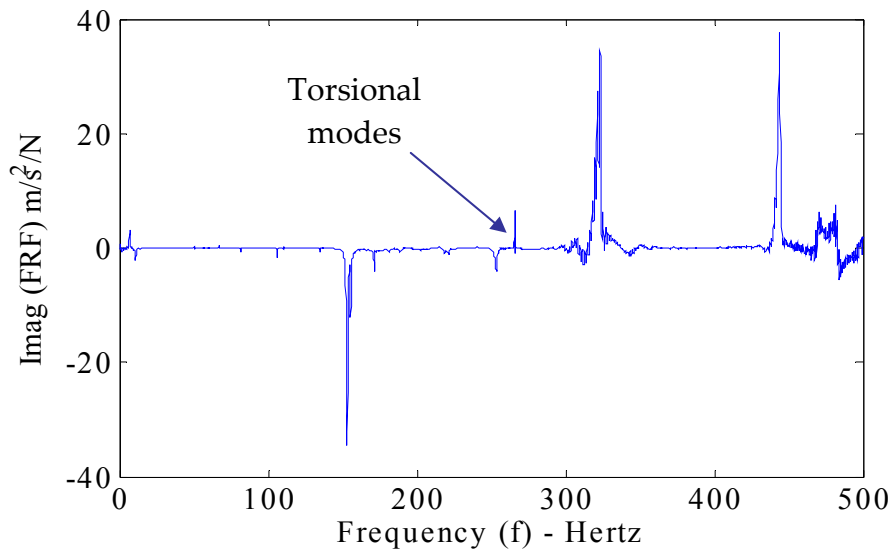
As it can be seen in Fig. 3-9d, the coherence values are excellent for this experiment, especially around the peaks (natural frequencies). There is a significant drop in the value of the coherence around the anti-resonance frequency which is expected due to a zero response in that region. Figure 3-13 provides an enlarged view of the coherence around the 4th natural frequency. An approximate value of 99% is obtained around this peak. Figure 3-14 shows the error of the frequency estimations with respect to the wavelengths which is higher for smaller wavelengths. This is because the error is dependent upon the ratio of the element span to the wavelength. When the wavelength spans a larger number of elements the estimations are more accurate. Likewise for the

wavelengths smaller than the size of the truss element the accuracy of the estimations can not be considered accurate. For the fundamental frequency the wavelength is 3 *m* which spans almost 15 elements and for the 4th natural frequency the wavelength is approximately 1.7 *m* which spans 8 elements. It is shown in this figure the error exponentially increases as the wavelength of the frequency of interest decreases.

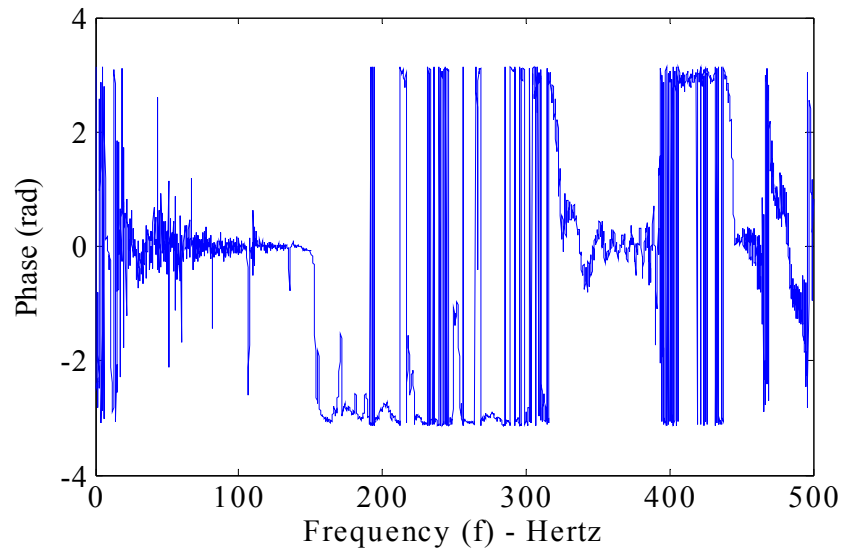
Finally, Table 3-4 presents the results for the case that the strain variations are included in the kinetic energy derivation for the truss element. As it can be observed, the frequencies do not change significantly as a result of this inclusion and only the 4th frequency changes slightly due to this effect. Therefore, for the analysis presented in the following chapters the effect of strain variation is considered to be negligible.



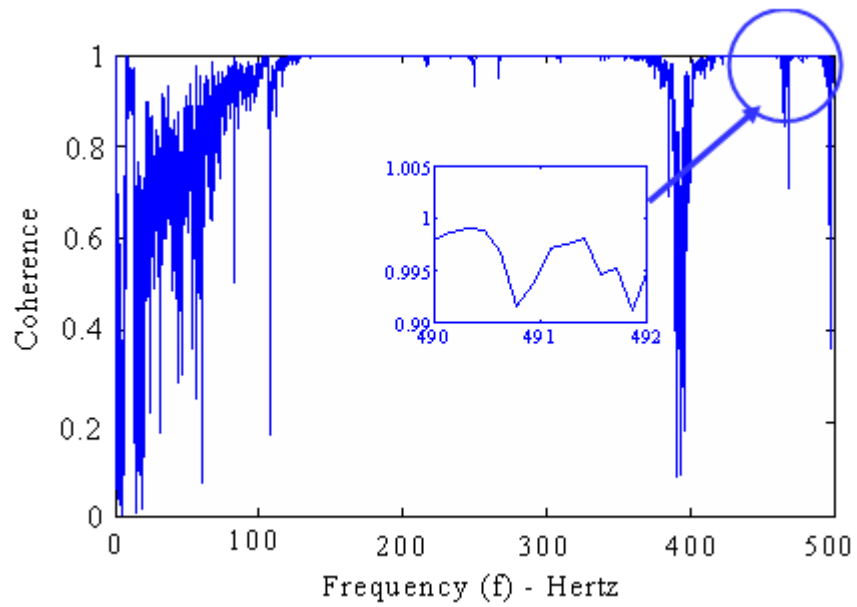
a)



b)



c)



d)

Figure 3-9 Experimental results: (a) Magnitude plot of the FRF, (b) Imaginary part of the FRF, (c) Phase plot, (d) Coherence plot

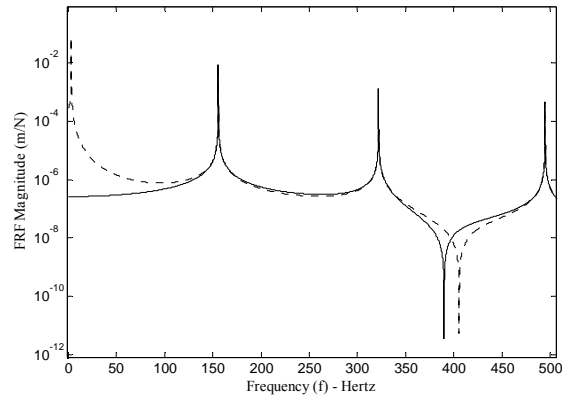


Figure 3-10 Magnitude of frequency response functions for the lattice with strings attached (dashed line) and without strings (smooth line)

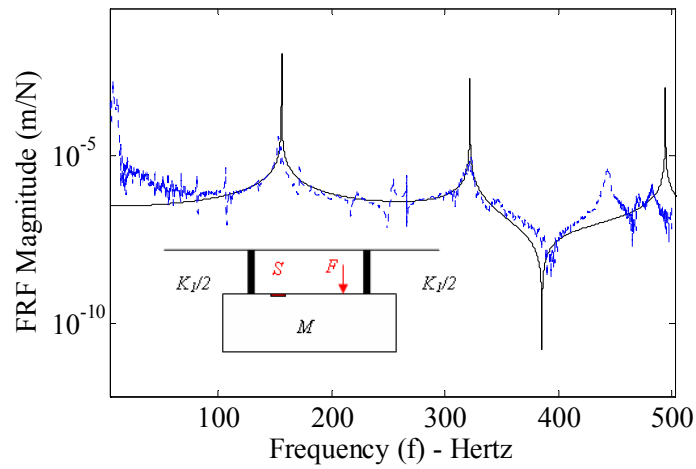


Figure 3-11 Magnitude of the frequency response functions for experiment (blue) and theory without strings (black)

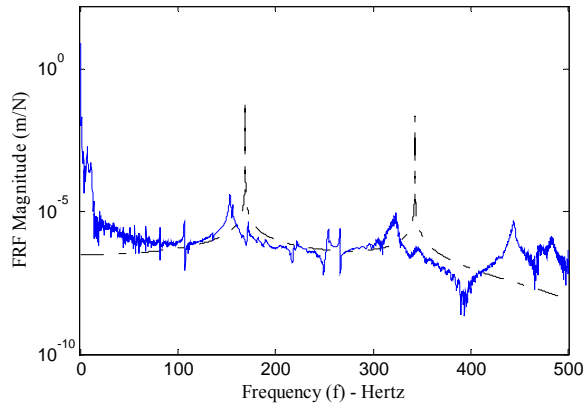


Figure 3-12 Magnitude of the frequency response functions for experiment (blue line) and theory with no mass-string at the boundaries (black line)

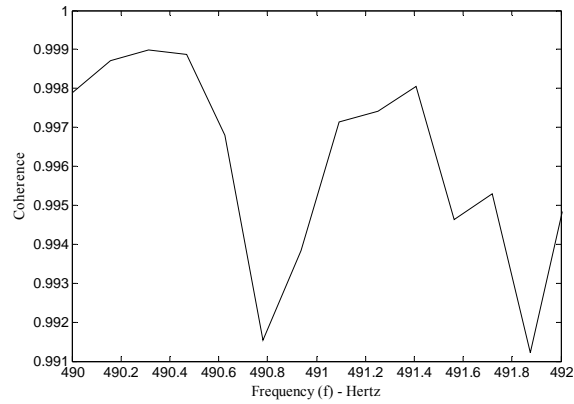


Figure 3-13 Coherence values around the fourth natural frequency

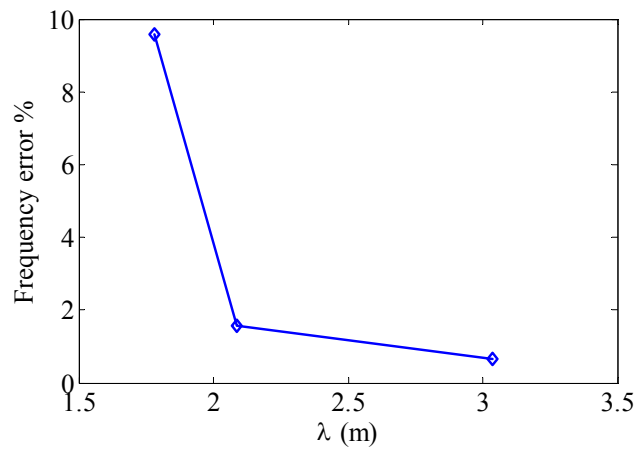


Figure 3-14 Error of the frequency estimations with respect to the wavelengths

Table 3-1 Material and geometrical properties of the bar members

Member	Cross-sectional area (m ²)	Modulus (N/m ²)	Density (Kg/m ³)	Length (m)
Longerons/battens	7.129×10 ⁻⁵	6.8948×10 ¹⁰	2416	217.6×10 ⁻³
Diagonal	2.107×10 ⁻⁵	2×10 ¹¹	7850	254.0×10 ⁻³

Table 3-2 Properties of the truss

Length of truss	Number of truss elements	Mass of the ball joint	Structure weight	Mass at boundary	Mass moment of inertia at boundary
1.96 m	9	0.1927 (Kg)	4.836 (Kg)	0.1392 (Kg)	0.0016 (Kgm ²)

Table 3-3 Theoretical and experimental natural frequencies

Mode	Theoretical frequency (Hz)	Experimental frequency (Hz)	Error (%)
1	6.88	6.87	0.07
2	154	153	0.65
3	319	324	1.54
4	491	444	10.6

Table 3-4 Theoretical and experimental natural frequencies (strain components included in the kinetic energy terms)

Mode	Theoretical frequency (Hz)	Experimental frequency (Hz)	Error (%)
1	6.88	6.87	0.07
2	154	153	0.65
3	319	324	1.57
4	489	444	9.20

3.8 Summary and Conclusion

Presented here are a homogenized methodology and the model experimental validation for a planar truss with Pratt Girder configuration. The governing PDE for the system consists of three coupled equations of motion for the longitudinal, bending and the rotation of the cross section. These equations have a form similar to an anisotropic Timoshenko beam theory. The natural frequencies and the frequency response functions of the system are found for both theory and the experiment. The results from the theory are shown to be in good agreement with the experiment (within 9% error for the frequencies). As a result, the method shows promise as a tool for use in the analysis and design of lattice structures of repeated patterns. The errors for the predicted natural frequencies of this model have better accuracy compared to the results of the previous research on modeling and experimental validation of the homogenization methods.^{48, 49}

Presented in the next chapter is a methodology to improve the results for the frequency response functions around higher frequencies.

Chapter 4

Micropolar Continuum Presentation

In the previous chapters, the continuum model derived for the truss assembly makes the assumption of the hinge joints. Another difficulty pertaining to finding equivalent continuum models for deployable structures occurs because of the joints between the inflatable members. This connection is different from pin or rigid joints that have been investigated in the previous research. The purpose of the presented work is to assume connections with torsional flexibility that can be measured prior to the construction of the lattice. Therefore, the beam members are assumed to bend and extend both, and none of the assumptions regarding the linearly varying displacement components presented in Chapter 2 are valid for this model. The strain energy of the fundamental repeating element is then found in terms of a new strain field and the micro-rotation of the members (See Figure 4-1). The assumptions made for deriving the strain energy of the beam members are inspired by the micropolar elasticity theory. The theory of micropolar elasticity was first proposed by Eringen (1966). It is assumed in this theory that the asymmetric stress tensor is determinate and the motion of the media is fully expressed

when the deformation and micro-rotation vectors are known. The couple stress theory is a special case of the micropolar theory where the micro-and macro rotations coincide. Figure 4-1 shows a comparison between the members of a regular continuum (hinge joints) and a micropolar continuum (bending members). Finally, necessary assumptions are made so that while the effect of the strain energy as a result of the micro-rotations are retained, they can be coupled to the primary strain states which are assumed to be independent and similar to those of the continuum model.

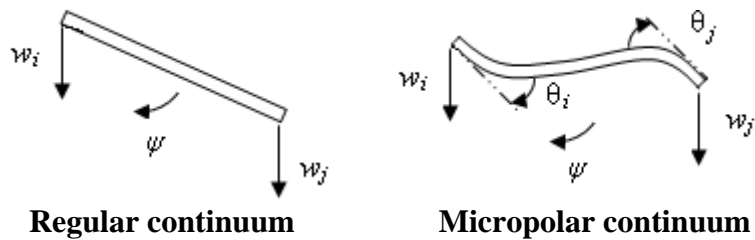


Figure 4-1 A comparison between a regular and a micropolar continuum
 (θ_i and θ_j micro-rotations) and (Ψ macro-rotation)

4.1 Strain Energy Derivations

Similar to the approach taken in Chapter 2, we start from the strain energy derivations of the fundamental element. Here, we model the joints of the fundamental element in Figure 4-2 as torsional joints with a constant stiffness to allow both bending and extension of the members. This is in contrast with the fundamental element in Chapter 2 which was assumed to be made of hinge joints and would allow tension and compression of the members only. Therefore, the strain energy for both bending and extension of the members as well as the strain energy stored in the joints are calculated to find the strain energy of the fundamental element.

4.1.1 Longerons (Tension, and Compression)

Figure 4-2 shows the longeron members in the fundamental frame element and their bending angles. Since all these members are aligned along the x axis, the only strain terms that contributes to the extension of these members are ε_x , κ_y and κ_z (the extension and the curvature for the cross section rotation around the y and z axis). Using the Taylor series expanded form of these strain components, the elongation of a longeron member can be found as,

$$\begin{aligned} \Delta L &= \int_0^{L_L} \varepsilon_x(x) dx = \int_0^{L_L} \left[(\varepsilon_x - y\kappa_y + z\kappa_z) + x^{(k)} (\partial\varepsilon_x - y\partial\kappa_y + z\partial\kappa_z) \right] dx \\ &= \left((\varepsilon_x - y\kappa_y + z\kappa_z)x + (\partial\varepsilon_x - y\partial\kappa_y + z\partial\kappa_z) \frac{x^2}{2} \right)_0^{L_L} \end{aligned} \quad (4.1)$$

where x , y and z are the Cartesian coordinates of the nodes on the longeron members. So the total elongation for each of the longeron members can be found. (A complete derivation for this is presented in the Appendix D). Consequently the strain energy as a result of the tension-compression of these members can be found as,

$$U_{Lt} = \frac{E_L A_L L_L}{8} \left(24\varepsilon_x^2 + 4L_b^2 (\kappa_y^2 + \kappa_z^2) + L_L^2 \left(6\delta\varepsilon_x^2 + L_b^2 (\delta\kappa_y^2 + \delta\kappa_z^2) \right) \right) \quad (4.2)$$

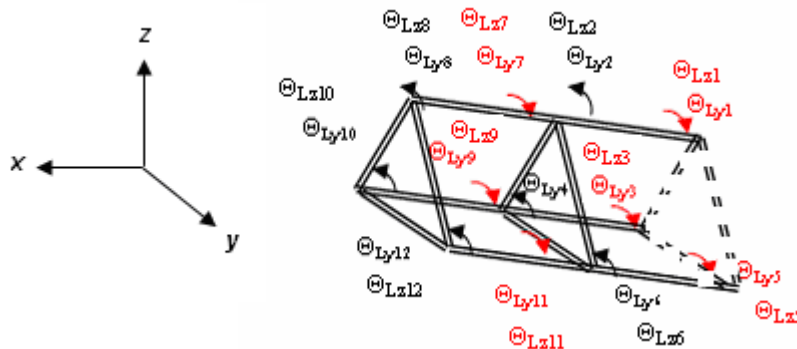


Figure 4-2 Longeron members in bending and the angular coordinates

4.1.2 Longerons (Bending)

Figure 4-3 shows the nodal forces and bending moments of a beam member in bending. Using the stiffness method in Timoshenko the reaction forces and moments can be found in terms of the deflection and angular components V_1 , V_2 , θ_1 , and θ_2 shown in the figure (See appendix D for derivations).⁵⁴ The strain energy of this member can be found using the displacements and their resultant forces and moment as,

$$U = \frac{EI}{L} \left(\frac{6(V_1 - V_2)^2}{L^2} - \frac{6(V_1 - V_2)(\theta_1 - \theta_2)}{L} + 2(\theta_1^2 + \theta_2^2 - \theta_1\theta_2) \right) \quad (4.3)$$



Figure 4-3 Deflection components of a member in bending

To find the nodal bending deflections V_1 and V_2 , the strain components that contribute to the bending of the nodes of a longeron member should be identified. For example ϵ_x contributes to the extension of the element in the x direction only and therefore will not appear in the bending relation of any of the longerons. Also, none of the strain components κ_y , κ_z appear in the bending equations for these members. So the strain components that appear in the bending deflections along the y and z directions for each of the longeron members can be identified. For instance, the bending along the z coordinate of node 1 in Figure 4-2 is caused by the strain component ϵ_z (extension along the z axis) and ϵ_{xz} (shear strain along the z axis). The results for the displacements along the y and z coordinates of the 9 nodes shown in Figure 4-2 are found and presented in Table 4-1. In

addition to such displacements the members have angular rotations around coordinates y and z also (micro-rotations). Such rotations for the coordinate y are shown in Figure 4-3.

Using the nodal deflections in Table 4-1 and the micro-rotations for the beam members the bending strain energy of the longeron members can be found as:

$$\begin{aligned}
 U_{Lb} = & \frac{1}{L_b^2 L_L} (E_L I_L (36 L_L^2 (\varepsilon_{xy}^2 + \varepsilon_{xz}^2) + L_b^2 (2\theta_{Ly1}^2 + 2\theta_{Ly2}^2 + 2(\theta_{Ly3}^2 - \theta_{Ly3}\theta_{Ly4} + \theta_{Ly4}^2 + \theta_{Ly5}^2 - \theta_{Ly5}\theta_{Ly6} + \theta_{Ly6}^2 \\
 & + \theta_{Ly7}^2 - \theta_{Ly7}\theta_{Ly8} + \theta_{Ly8}^2 + \theta_{Ly9}^2 - \theta_{Ly9}\theta_{Ly10} + \theta_{Ly10}^2 + \theta_{Ly11}^2 - \theta_{Ly11}\theta_{Ly12} + \theta_{Ly12}^2 + \theta_{Lz1}^2 - \theta_{Lz1}\theta_{Lz2} \\
 & + \theta_{Lz2}^2 + \theta_{Lz3}^2 - \theta_{Lz3}\theta_{Lz4} + \theta_{Lz4}^2 + \theta_{Lz5}^2 - \theta_{Lz5}\theta_{Lz6} + \theta_{Lz6}^2 + \theta_{Lz7}^2 - \theta_{Lz7}\theta_{Lz8} + \theta_{Lz8}^2 + \theta_{Lz9}^2 - \theta_{Lz9}\theta_{Lz10} \\
 & + \theta_{Lz10}^2 + \theta_{Lz11}^2 - \theta_{Lz11}\theta_{Lz12} + \theta_{Lz12}^2) - 2\sqrt{3} L_L \theta_{Ly2} \kappa_x - L_L (3\theta_{Ly3} - 3\theta_{Ly4} + 3\theta_{Ly5} - 3\theta_{Ly6} - 2\sqrt{3}\theta_{Ly7} \\
 & + 2\sqrt{3}\theta_{Ly8} + 3\theta_{Ly9} - 3\theta_{Ly10} + 3\theta_{Ly11} - 3\theta_{Ly12} + \sqrt{3}(\theta_{Lz3} - \theta_{Lz4} - \theta_{Lz5} + \theta_{Lz6} + \theta_{Lz9} - \theta_{Lz10} - \theta_{Lz11} \\
 & + \theta_{Lz12})) \kappa_x + 12 L_L^2 \kappa_x^2 - 2\theta_{Ly1}(\theta_{Ly2} - \sqrt{3} L_L \kappa_x) + 2 L_b L_L (-3(\theta_{Lz1} - \theta_{Lz2} + \theta_{Lz3} - \theta_{Lz4} + \theta_{Lz5} - \theta_{Lz6} \\
 & + \theta_{Lz7} - \theta_{Lz8} + \theta_{Lz9} - \theta_{Lz10} + \theta_{Lz11} - \theta_{Lz12}) \varepsilon_{xz} + \varepsilon_{xy} (-3\theta_{Ly1} + 3(\theta_{Ly2} - \theta_{Ly3} + \theta_{Ly4} - \theta_{Ly5} + \theta_{Ly6} \\
 & - \theta_{Ly7} + \theta_{Ly8} - \theta_{Ly9} + \theta_{Ly10} - \theta_{Ly11} + \theta_{Ly12}) - 4(-3 + \sqrt{3}) L_L \kappa_x))
 \end{aligned}
 \tag{4.4}$$

Table 4-1 Nodal bending deflection components of the fundamental element

Node	V	w
1	$\frac{L_b \sqrt{3}}{3} \varepsilon_{yz} - L_L \varepsilon_{xy} + \kappa_x L_L \frac{L_b \sqrt{3}}{3}$	$\frac{L_b \sqrt{3}}{3} \varepsilon_z - L_L \varepsilon_{xz}$
2	$\frac{L_b \sqrt{3}}{3} \varepsilon_{yz}$	$\frac{L_b \sqrt{3}}{3} \varepsilon_z$
3	$L_L \varepsilon_{xy} + \frac{L_b \sqrt{3}}{3} \varepsilon_{yz} - \kappa_x L_L \frac{L_b \sqrt{3}}{3}$	$\frac{L_b \sqrt{3}}{3} \varepsilon_z + L_L \varepsilon_{xz}$
4	$\frac{L_b}{2} \varepsilon_y - L_L \varepsilon_{xy} - \frac{L_b \sqrt{3}}{6} \varepsilon_{yz} - \frac{\sqrt{3}}{2} \kappa_x L_L \frac{L_b \sqrt{3}}{2}$	$-\frac{L_b \sqrt{3}}{6} \varepsilon_z - L_L \varepsilon_{xz} + \frac{L_b}{2} \varepsilon_{yz} - \frac{1}{2} \kappa_x L_L \frac{L_b \sqrt{3}}{3}$
5	$\frac{L_b}{2} \varepsilon_y - \frac{L_b \sqrt{3}}{6} \varepsilon_{yz}$	$-\frac{L_b \sqrt{3}}{6} \varepsilon_z + \frac{L_b}{2} \varepsilon_{yz}$
6	$\frac{L_b}{2} \varepsilon_y + L_L \varepsilon_{xy} - \frac{L_b \sqrt{3}}{6} \varepsilon_{yz} + \frac{\sqrt{3}}{2} \kappa_x L_L \frac{L_b \sqrt{3}}{2}$	$-\frac{L_b \sqrt{3}}{6} \varepsilon_z + L_L \varepsilon_{xz} + \frac{L_b}{2} \varepsilon_{yz} + \frac{1}{2} \kappa_x L_L \frac{L_b \sqrt{3}}{3}$
7	$-\frac{L_b}{2} \varepsilon_y - L_L \varepsilon_{xy} - \frac{L_b \sqrt{3}}{6} \varepsilon_{yz} - \frac{\sqrt{3}}{2} \kappa_x L_L \frac{L_b \sqrt{3}}{2}$	$-\frac{L_b \sqrt{3}}{6} \varepsilon_z - L_L \varepsilon_{xz} - \frac{L_b}{2} \varepsilon_{yz} + \frac{1}{2} \kappa_x L_L \frac{L_b \sqrt{3}}{3}$
8	$-\frac{L_b}{2} \varepsilon_y - \frac{L_b \sqrt{3}}{6} \varepsilon_{yz}$	$-\frac{L_b \sqrt{3}}{6} \varepsilon_z - \frac{L_b}{2} \varepsilon_{yz}$
9	$-\frac{L_b}{2} \varepsilon_y + L_L \varepsilon_{xy} - \frac{L_b \sqrt{3}}{6} \varepsilon_{yz} + \frac{\sqrt{3}}{2} \kappa_x L_L \frac{L_b \sqrt{3}}{2}$	$-\frac{L_b \sqrt{3}}{6} \varepsilon_z + L_L \varepsilon_{xz} - \frac{L_b}{2} \varepsilon_{yz} - \frac{1}{2} \kappa_x L_L \frac{L_b \sqrt{3}}{3}$

4.1.3 Battens (Tension, and Compression)

To find the strain energy of the battens, we use a similar approach used for the longeron members. We first identify the strain values that should appear in the extension of these members. It is clear that the strain component ϵ_x (extension along the length of the element) does not contribute the extension of the battens since these members are at the cross section. Also the strain values ϵ_{xy} and ϵ_{xz} do not appear in the extension of these members. This is because the nodal displacement for such strain values can be found using the relations $x.\epsilon_{xy}$ and $x.\epsilon_{xz}$. Since all the nodes at a cross section have the same coordinate x (shown in Figure 4-2), the displacements as a result of these strain components are the same for all the nodes. As a result, there will be no strain in a batten member for ϵ_{xy} and ϵ_{xz} since all the nodes deflect in the same amount. Finally, the only strain components that contribute to the extension and bending of the battens are ϵ_y , ϵ_z and ϵ_{yz} . Figure 4-4 shows how the strain ϵ_y results in the extension of the batten members.

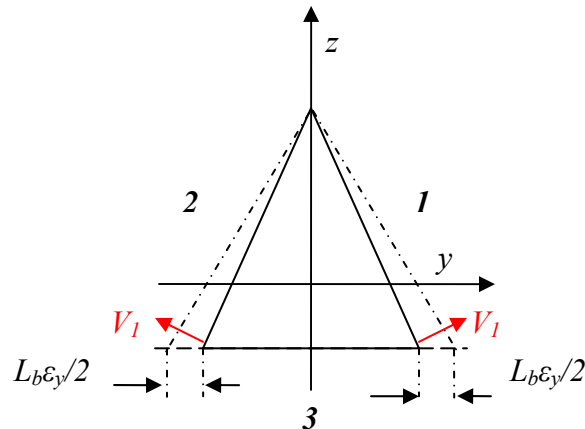


Figure 4-4 Bending and extension of battens for ϵ_y

For members 1 and 2 shown in this figure we get,

$$y^2 + \underbrace{z^2}_{\text{constant}} = l^2 \quad (4.5)$$

where l is the initial length of each member, therefore we get:

$$y.dy = l.dl \rightarrow \frac{dl}{dy} = \frac{y}{L_b} \rightarrow \frac{dl}{dy} = \frac{L_b}{2} = \frac{1}{2} \quad (4.6)$$

So for the extension of members 1 and 2 we have,

$$dl = \frac{dy}{2} = \frac{\frac{L_b \varepsilon_y}{2}}{2} = \frac{L_b \varepsilon_y}{4} \quad (4.7)$$

Also the extension of the third member can be found as,

$$dl_3 = L_b \varepsilon_y \quad (4.8)$$

The bending deflection components can also be identified. Since nodal bending displacement is measured in a perpendicular direction to each member, the projection of the deflection (V_1) should be found. So for the bending component as a result of the ε_y we get:

$$V_1 = \frac{L_b}{2} \varepsilon_y \cos(30) = \frac{\sqrt{3}}{4} L_b \varepsilon_y \quad (4.9)$$

Equation (4.9) is used to find the bending strain energy of the batten members. A complete derivation for the bending and extensional components of the batten members is presented in the Appendix D. Finally, for the extensional energy of the battens we get:

$$\begin{aligned} U_{bt} = & \frac{1}{128} A_b E_b L_b \left(16 \left(L_L^2 \frac{\partial^2 \varepsilon_y}{\partial x^2} + 2L_L \frac{\partial \varepsilon_y}{\partial x} + 2\varepsilon_y \right) + 24(3\varepsilon_y^2 + 2\varepsilon_y \varepsilon_z + 3\varepsilon_z^2 + 4\varepsilon_{yz}^2) \right. \\ & + \left(L_L^2 \left(\frac{\partial^2 \varepsilon_y}{\partial x^2} + 3 \frac{\partial^2 \varepsilon_z}{\partial x^2} - 2\sqrt{3} \frac{\partial^2 \varepsilon_{yz}}{\partial x^2} \right) + 2L_L \left(\frac{\partial \varepsilon_y}{\partial x} + 3 \frac{\partial \varepsilon_z}{\partial x} - 2\sqrt{3} \frac{\partial \varepsilon_{yz}}{\partial x} \right) \right. \\ & + 2(\varepsilon_y + 3\varepsilon_z - 2\sqrt{3}\varepsilon_{yz})^2 + \left. \left. \left(L_L^2 \left(\frac{\partial^2 \varepsilon_y}{\partial x^2} + 3 \frac{\partial^2 \varepsilon_z}{\partial x^2} + 2\sqrt{3} \frac{\partial^2 \varepsilon_{yz}}{\partial x^2} \right) \right. \right. \\ & \left. \left. + 2L_L \left(\frac{\partial \varepsilon_y}{\partial x} + 3 \frac{\partial \varepsilon_z}{\partial x} + 2\sqrt{3} \frac{\partial \varepsilon_{yz}}{\partial x} \right) + 2(\varepsilon_y + 3\varepsilon_z + 2\sqrt{3}\varepsilon_{yz})^2 \right) \right) \end{aligned} \quad (4.10)$$

4.1.4 Batten (Bending)

Figure 4-5 shows the bending deflection components (V_{11} , V_{12} ,... etc.) of the batten members as a result of the strain values ε_y , ε_z and ε_{yz} . The first index represents each of the two nodes of the beam member and the second index denotes the bar member shown in the figure. The angular deflections of the battens are also shown in Figure 4-6. Similar to the previous section, the bending components shown in Figure 4-5 can be found. A complete derivation for these is presented in the Appendix D. For the bending displacements of the first batten member shown in Figure 4-5 we get,

$$\begin{aligned} V_{11} &= -\frac{L_b\sqrt{3}}{6}\varepsilon_z - \frac{L_b}{2}\varepsilon_{yz} \\ V_{21} &= -\frac{L_b\sqrt{3}}{4}\varepsilon_y + \frac{L_b\sqrt{3}}{12}\varepsilon_z \end{aligned} \quad (4.11)$$

Similarly for the second and the third members, we have,

$$\begin{aligned} V_{12} &= -\frac{L_b\sqrt{3}}{4}\varepsilon_y + \frac{L_b\sqrt{3}}{12}\varepsilon_z & \text{and,} & & V_{13} &= \frac{L_b}{2}\varepsilon_{yz} + \frac{L_b\sqrt{3}}{6}\varepsilon_z \\ V_{22} &= -\frac{L_b\sqrt{3}}{6}\varepsilon_z + \frac{L_b}{2}\varepsilon_{yz} & & & V_{23} &= -\frac{L_b}{2}\varepsilon_{yz} + \frac{L_b\sqrt{3}}{6}\varepsilon_z \end{aligned} \quad (4.12)$$

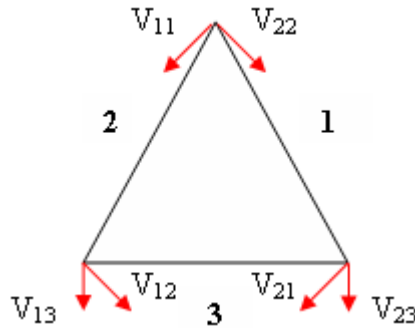


Figure 4-5 Bending deflection components of the battens

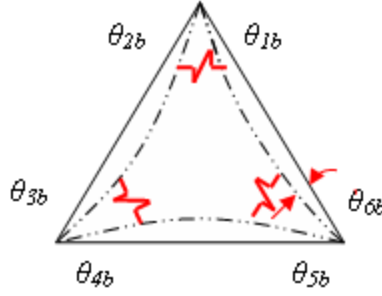


Figure 4-6 Angular deflections of the battens and the torsional joints

Finally the total bending strain energy of the batten members for this element shown in Figure 4-2 can be found as,

$$\begin{aligned}
 U_{bb} = \frac{1}{4L_b} (E_b I_b (8(\theta_{1b}^2 + \theta_{2b}^2 + \theta_{3b}^2 + \theta_{4b}^2 + \theta_{5b}^2 + \theta_{6b}^2 + \theta_{7b}^2 + \theta_{8b}^2 \\
 + \theta_{9b}^2 + \theta_{10b}^2 + \theta_{11b}^2 + \theta_{12b}^2 - \theta_{2b}\theta_{3b} + \theta_{4b}\theta_{5b} - \theta_{8b}\theta_{9b} + \theta_{10b}\theta_{11b}) \\
 + 6\sqrt{3}(\theta_{3b} + \theta_{9b})(\varepsilon_y - \varepsilon_z) + 12(\theta_{9b} + \theta_{3b} - 2(\theta_{10b} + \theta_{11b} + \theta_{4b} + \theta_{5b}))\varepsilon_{yz} \\
 + (\theta_{2b} + \theta_{8b})(-6\sqrt{3}\varepsilon_y + 6\sqrt{3}\varepsilon_z - 12\varepsilon_{yz}) - 8(\theta_{1b}\theta_{6b} + \theta_{7b}\theta_{12b}) \\
 + (\theta_{1b} + \theta_{6b} + \theta_{7b} + \theta_{12b})(-6\sqrt{3}\varepsilon_y + 6\sqrt{3}\varepsilon_z + 12\varepsilon_{yz}) \\
 + 18((\varepsilon_y - \varepsilon_z)^2 + 4\varepsilon_{yz}^2)))
 \end{aligned} \tag{4.13}$$

4.1.5 Joints

In this model we assume that the joints are elements with torsional stiffness. The strain energy stored in the joints can be easily found using the angular displacements of the members and is written in the following form:

$$\begin{aligned}
 U_S = \frac{1}{2}K_t(\theta_{2b} - \theta_{1b})^2 + \frac{1}{2}K_t(\theta_{4b} - \theta_{3b})^2 + \frac{1}{2}K_t(\theta_{6b} - \theta_{5b})^2 + \frac{1}{2}K_t(\theta_{8b} - \theta_{7b})^2 + \frac{1}{2}K_t(\theta_{10b} - \theta_{9b})^2 \\
 + \frac{1}{2}K_t(\theta_{12b} - \theta_{11b})^2 + \frac{1}{2}K_t \sum_{i=1}^{12} (\theta_{Ly_i}^2 + \theta_{Lz_i}^2)
 \end{aligned} \tag{4.14}$$

where θ_{Lzi} , θ_{Lyi} , and θ_{ib} define the rotation of the longerons around the y and z axes and the angular deflection of the battens respectively as shown in Figures 4-2 and 4-6. The strain energy of the diagonal members can be found in a very similar manner. Using (4.14) and the relations for the bending and the extensional strain energy of all the members, the total strain energy of the repeating frame element can be found. This relation contains both the strain components evaluated at the center of the element and the angular displacement components.

4.2 Reduced Order Strain Energy

Similar to the approach in Chapter 2, necessary assumptions should be made to find the strain energy of the reduced order model of this structure. As can be seen from the relations in the previous section, the strain energy is a function of the strain values such as ε_y , ε_z and ε_{yz} as well as the angular displacement components of the members. To find an equivalent 1-D model, the strain energy should be a function of the strain values similar to a beam member only. Therefore, necessary assumptions should be made to reduce the independent strain components and strain gradients as well as the angular deflections. Some of these assumptions were used in Chapter 2. Additional assumptions need to be made to express the bending angles in terms of the strain values of a beam element. To establish an understanding of such relations a simple example for a multiple degree of freedom mass-spring system is presented here. Figure 4-7 shows schematic of a mass-spring system.

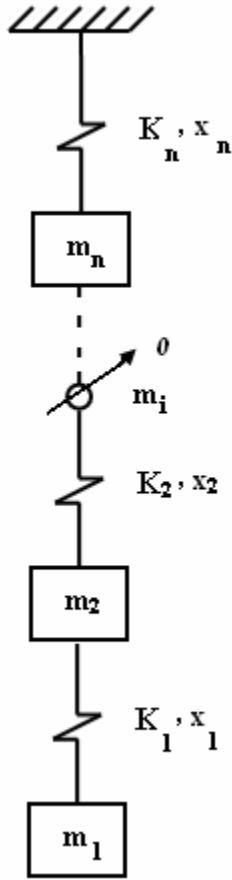


Figure 4-7 Schematic of an n-degree of freedom mass-spring system

The relation for the strain energy of this system can be found as,

$$U = \frac{1}{2} \sum_{i=1}^{n-1} K_i (x_i - x_{i+1})^2 + \frac{1}{2} K_n x_n^2 \quad (4.15)$$

The internal force applied to the inertia m_i can be found using the derivative of the strain energy with respect to the coordinate x_i .

$$F_i = \frac{\partial U}{\partial x_i} \quad (4.16)$$

Therefore, having the total strain energy of the system as a function of all the coordinates,

$$U = f(x_1, x_2, \dots, x_i, \dots, x_n) \quad (4.17)$$

in the absence of the external forces, the Newton's second law for the coordinate x_i of negligible inertia will require that:

$$m_i \rightarrow 0 \Rightarrow \frac{\partial U}{\partial x_i} = 0 \quad (4.18)$$

This is equivalent of the assumption of a nodal force balance in the system at coordinate x_i which results in a relation between coordinate x_i and the other coordinates as follows:

$$x_i = g(x_1, x_2, \dots, x_{i-1}, x_{i+1}, \dots, x_n) \quad (4.19)$$

For the truss structure in this study, we make a similar assumption to this example to ignore not the mass of the members but the mass moment of inertia of the beam members and the joints in the element shown in Figure 4-2. Because both the mass and the geometry of the members are small compared to the overall length of the structure, the mass moment of inertia is by orders of magnitude smaller than the whole structure. For example the mass moment of inertia of the longeron member is 2×10^{-6} % of the whole structure. Therefore, we neglect the mass moment of inertia of all members in Figure 4-2. As a result the related torque values for the rotational degrees of freedom should vanish. This assumption for the batten members results in the following:

$$\frac{\partial U_e}{\partial \theta_{ib}} = 0 \quad \text{for } i = 1 \rightarrow 12 \quad (4.20)$$

So we get,

$$\left\{ \begin{array}{l}
4L_b K_t (\theta_{1b} - \theta_{2b}) + E_b I_b (8\theta_{1b} - 4\theta_{6b} + 3\sqrt{3}\varepsilon_y - 3\sqrt{3}\varepsilon_z - 6\varepsilon_{yz}) = 0 \\
4L_b K_t (\theta_{1b} - \theta_{2b}) + E_b I_b (-8\theta_{1b} + 4\theta_{6b} + 3\sqrt{3}\varepsilon_y - 3\sqrt{3}\varepsilon_z + 6\varepsilon_{yz}) = 0 \\
4L_b K_t (\theta_{3b} - \theta_{4b}) + E_b I_b (-4\theta_{2b} + 8\theta_{3b} + 3\sqrt{3}\varepsilon_y - 3\sqrt{3}\varepsilon_z + 6\varepsilon_{yz}) = 0 \\
L_b K_t (\theta_{3b} - \theta_{4b}) - E_b I_b (2\theta_{4b} + \theta_{5b} - 3\varepsilon_{yz}) = 0 \\
L_b K_t (\theta_{5b} - \theta_{6b}) + E_b I_b (\theta_{4b} + 2\theta_{5b} - 3\varepsilon_{yz}) = 0 \\
4L_b K_t (\theta_{5b} - \theta_{6b}) + E_b I_b (4\theta_{1b} - 8\theta_{6b} + 3\sqrt{3}\varepsilon_y - 3\sqrt{3}\varepsilon_z - 6\varepsilon_{yz}) = 0 \\
4L_b K_t (\theta_{7b} - \theta_{8b}) + E_b I_b (8\theta_{7b} - 4\theta_{12b} + 3\sqrt{3}\varepsilon_y - 3\sqrt{3}\varepsilon_z - 6\varepsilon_{yz}) = 0 \\
4L_b K_t (\theta_{7b} - \theta_{8b}) + E_b I_b (-8\theta_{7b} + 4\theta_{12b} + 3\sqrt{3}\varepsilon_y - 3\sqrt{3}\varepsilon_z + 6\varepsilon_{yz}) = 0 \\
4L_b K_t (\theta_{9b} - \theta_{10b}) + E_b I_b (-4\theta_{8b} + 8\theta_{9b} + 3\sqrt{3}\varepsilon_y - 3\sqrt{3}\varepsilon_z + 6\varepsilon_{yz}) = 0 \\
L_b K_t (\theta_{9b} - \theta_{10b}) - E_b I_b (2\theta_{10b} + \theta_{11b} - 3\varepsilon_{yz}) = 0 \\
L_b K_t (\theta_{11b} - \theta_{12b}) + E_b I_b (\theta_{10b} + 2\theta_{11b} - 3\varepsilon_{yz}) = 0 \\
4L_b K_t (\theta_{11b} - \theta_{12b}) + E_b I_b (4\theta_{7b} - 8\theta_{12b} + 3\sqrt{3}\varepsilon_y - 3\sqrt{3}\varepsilon_z - 6\varepsilon_{yz}) = 0
\end{array} \right. \quad (4.21)$$

For the bending of longerons around the y axis and their moments we get,

$$\frac{\partial U_e}{\partial \theta_{Ly_i}} = 0 \quad \text{for } i = 1 \rightarrow 12 \quad (4.22)$$

Therefore, we have,

$$\begin{cases}
L_b L_L K_t \theta_{Ly1} + E_L I_L (2L_b \theta_{Ly1} - L_b \theta_{Ly2} - 3L_L \varepsilon_{xy} + \sqrt{3} L_b L_L \kappa_x) = 0 \\
E_L I_L (-3L_L \varepsilon_{xy} + L_b (\theta_{Ly1} - 2\theta_{Ly2} + \sqrt{3} L_L \kappa_x)) - L_b L_L K_t \theta_{Ly2} = 0 \\
2L_b L_L K_t \theta_{Ly3} + E_L I_L (4L_b \theta_{Ly3} - 2L_b \theta_{Ly4} - 6L_L \varepsilon_{xy} - 3L_b L_L \kappa_x) = 0 \\
2L_b L_L K_t \theta_{Ly4} + E_L I_L (-2L_b \theta_{Ly3} + 4L_b \theta_{Ly4} + 6L_L \varepsilon_{xy} + 3L_b L_L \kappa_x) = 0 \\
2L_b L_L K_t \theta_{Ly5} + E_L I_L (4L_b \theta_{Ly5} - 2L_b \theta_{Ly6} - 6L_L \varepsilon_{xy} - 3L_b L_L \kappa_x) = 0 \\
2L_b L_L K_t \theta_{Ly6} + E_L I_L (-2L_b \theta_{Ly5} + 4L_b \theta_{Ly6} + 6L_L \varepsilon_{xy} + 3L_b L_L \kappa_x) = 0 \\
L_b L_L K_t \theta_{Ly7} + E_L I_L (2L_b \theta_{Ly7} - L_b \theta_{Ly8} - 3L_L \varepsilon_{xy} + \sqrt{3} L_b L_L \kappa_x) = 0 \\
-L_b L_L K_t \theta_{Ly8} + E_L I_L (-3L_L \varepsilon_{xy} + L_b (\theta_{Ly7} - 2\theta_{Ly8} + \sqrt{3} L_L \kappa_x)) = 0 \\
2L_b L_L K_t \theta_{Ly9} + E_L I_L (4L_b \theta_{Ly9} - 2L_b \theta_{Ly10} - 6L_L \varepsilon_{xy} - 3L_b L_L \kappa_x) = 0 \\
2L_b L_L K_t \theta_{Ly10} + E_L I_L (-2L_b \theta_{Ly9} + 4L_b \theta_{Ly10} + 6L_L \varepsilon_{xy} + 3L_b L_L \kappa_x) = 0 \\
2L_b L_L K_t \theta_{Ly11} + E_L I_L (4L_b \theta_{Ly11} - 2L_b \theta_{Ly12} - 6L_L \varepsilon_{xy} - 3L_b L_L \kappa_x) = 0 \\
2L_b L_L K_t \theta_{Ly12} + E_L I_L (-2L_b \theta_{Ly11} + 4L_b \theta_{Ly12} + 6L_L \varepsilon_{xy} + 3L_b L_L \kappa_x) = 0
\end{cases} \tag{4.23}$$

and finally for the bending angles of the longerons along z axis we have,

$$\frac{\partial U_e}{\partial \theta_{Lzi}} = 0 \quad \text{for } i = 1 \rightarrow 12 \tag{4.24}$$

$$\begin{cases}
L_b L_L K_t \theta_{Lz1} + E_L I_L (2L_b \theta_{Lz1} - L_b \theta_{Lz2} - 3L_L \varepsilon_{xz}) = 0 \\
L_b L_L K_t \theta_{Lz2} + E_L I_L (-L_b \theta_{Lz1} + 2L_b \theta_{Lz2} + 3L_L \varepsilon_{xz}) = 0 \\
-2L_b L_L K_t \theta_{Lz3} + E_L I_L (-4L_b \theta_{Lz3} + 2L_b \theta_{Lz4} + 6L_L \varepsilon_{xz} + \sqrt{3}L_b L_L \kappa_x) = 0 \\
2L_b L_L K_t \theta_{Lz4} + E_L I_L (-2L_b \theta_{Lz3} + 4L_b \theta_{Lz4} + 6L_L \varepsilon_{xz} + \sqrt{3}L_b L_L \kappa_x) = 0 \\
2L_b L_L K_t \theta_{Lz5} + E_L I_L (4L_b \theta_{Lz5} - 2L_b \theta_{Lz6} - 6L_L \varepsilon_{xz} + \sqrt{3}L_b L_L \kappa_x) = 0 \\
-2L_b L_L K_t \theta_{Lz6} + E_L I_L (2L_b \theta_{Lz5} - 4L_b \theta_{Lz6} - 6L_L \varepsilon_{xz} + \sqrt{3}L_b L_L \kappa_x) = 0 \\
L_b L_L K_t \theta_{Lz7} + E_L I_L (2L_b \theta_{Lz7} - L_b \theta_{Lz8} - 3L_L \varepsilon_{xz}) = 0 \\
L_b L_L K_t \theta_{Lz8} + E_L I_L (-L_b \theta_{Lz7} + 2L_b \theta_{Lz8} + 3L_L \varepsilon_{xz}) = 0 \\
-2L_b L_L K_t \theta_{Lz9} + E_L I_L (-4L_b \theta_{Lz9} + 2L_b \theta_{Lz10} + 6L_L \varepsilon_{xz} + \sqrt{3}L_b L_L \kappa_x) = 0 \\
2L_b L_L K_t \theta_{Lz10} + E_L I_L (-2L_b \theta_{Lz9} + 4L_b \theta_{Lz10} + 6L_L \varepsilon_{xz} + \sqrt{3}L_b L_L \kappa_x) = 0 \\
2L_b L_L K_t \theta_{Lz11} + E_L I_L (4L_b \theta_{Lz11} - 2L_b \theta_{Lz12} - 6L_L \varepsilon_{xz} + \sqrt{3}L_b L_L \kappa_x) = 0 \\
-2L_b L_L K_t \theta_{Lz12} + E_L I_L (2L_b \theta_{Lz11} - 4L_b \theta_{Lz12} - 6L_L \varepsilon_{xz} + \sqrt{3}L_b L_L \kappa_x) = 0
\end{cases} \tag{4.25}$$

These equations in addition to the assumptions regarding the compatibility condition, free local deformations and the shear deformation type beam in Chapter 2 (See Appendix D) are used to find the strain energy of the equivalent beam model. This results in a total of 51 equations and 57 variables (rotational degrees of freedom, strain components and their gradients). Therefore, all the strain values and subsequently the strain energy relation can be found in terms of 6 independent strain components (ε_x , ε_{xy} , ε_{xz} , κ_y , κ_z , and κ_x) as follows:

$$U_e = C_1 \varepsilon_x^2 + C_2 \varepsilon_{xy}^2 + C_3 \varepsilon_{xz}^2 + C_4 \kappa_y^2 + C_5 \kappa_z^2 + C_6 \kappa_x^2 + C_7 \varepsilon_{xy} \kappa_x \tag{4.26}$$

where the coefficients C_1 to C_7 can be found as,

$$C_1 = 3L_L A_L E_L$$

$$\begin{aligned}
C_2 = C_3 = & \frac{12L_L^2 E_L \left(3A_d E_d L_d L_L^4 I_L K_t^2 + 2A_L \left(36A_d E_d L_b^4 L_d E_L^2 I_L^2 + A_d E_d L_b^4 L_d L_L^2 K_t^2 + 6L_L E_L I_L K_t \left(2A_d E_d L_b^4 L_d + (L_b^2 + L_L^2)^2 K_t \right) \right) \right)}{L_b^2 \left(A_d E_d L_d L_L^3 + 4(L_b^2 + L_L^2)^2 A_L E_L \right) (6E_L I_L + L_L K_t)^2} \\
& + \frac{54L_L^2 E_L^2 I_L^2 K_t (36E_L^2 I_L^2 + 30L_L E_L I_L K_t + 5L_L^2 K_t^2)}{L_b^2 (3E_L I_L + L_L K_t)^2 (6E_L I_L + L_L K_t)^2} \\
C_4 = C_5 = & \frac{1}{2} L_b^2 L_L A_L E_L \\
C_6 = & \frac{\left(L_L^2 E_L \left(48A_d E_d L_d L_L^4 I_L K_t^2 + A_L \left(36A_d E_d L_b^4 L_d E_L^2 I_L^2 + A_d E_d L_b^4 L_d L_L^2 K_t^2 + 12L_L E_L I_L K_t \left(A_d E_d L_b^4 L_d + 4(L_b^2 + L_L^2)^2 K_t \right) \right) \right) \right)}{\left(\left(A_d E_d L_d L_L^3 + (L_b^2 + L_L^2)^2 A_L E_L \right) (6E_L I_L + L_L K_t)^2 \right)} \\
& + \frac{72L_L^2 E_L^2 I_L^2 K_t (36E_L^2 I_L^2 + 30L_L E_L I_L K_t + 5L_L^2 K_t^2)}{(3E_L I_L + L_L K_t)^2 (6E_L I_L + L_L K_t)^2} \\
C_7 = & -\frac{8(-3 + \sqrt{3}) L_b^3 E_L I_L K_t^2}{L_b (6E_L I_L + L_L K_t)^2} + \frac{6L_L^2 E_L^2 I_L^2 K_t (36E_L^2 I_L^2 + 30L_L E_L I_L K_t + 5L_L^2 K_t^2) (-2(-3 + \sqrt{3}) L_b)}{L_b^2 (3E_L I_L + L_L K_t)^2 (6E_L I_L + L_L K_t)^2}
\end{aligned} \tag{4.27}$$

As shown in Eq. (4.26) the strain energy includes a non-quadratic term which is related to the coupling between the shear force (τ_{xy}) and the torsion (κ_x) in the structure. As a result, the structure loses its symmetry for the bending along the y and z coordinates.

4.3 Equations of Motion

Having the expressions for the strain and kinetic energy of the fundamental element, the governing equations of motion can be found. As shown in the previous section there is a coupling between the shear strain ε_{xy} and the torsion which results in a coupling between the coordinates Φ_x , Φ_z and v . This coupling is shown more clearly in Figure 4-8. Finally, the equations for the six coordinates of vibrations (evaluated at the center of the element)

decouple into three sets of the equations shown here. For the Φ_x , Φ_z and v coordinates we get,

$$\begin{cases} C_7 \frac{\partial \phi_x}{\partial x} - 4m_2 \frac{\partial^2 \phi_z}{\partial t^2} + C_4 \frac{\partial^2 \phi_z}{\partial x^2} + C_2 \left(-\phi_z + \frac{\partial v^0}{\partial x} \right) = 0 \\ 4(m_2 + m_3) \frac{\partial^2 \phi_x}{\partial t^2} - C_6 \frac{\partial^2 \phi_x}{\partial x^2} + C_7 \left(\frac{\partial \phi_z}{\partial x} - \frac{\partial^2 v^0}{\partial x^2} \right) = 0 \\ C_7 \frac{\partial^2 \phi_x}{\partial x^2} - 4m_1 \frac{\partial^2 v^0}{\partial t^2} + C_2 \left(-\frac{\partial \phi_z}{\partial x} + \frac{\partial^2 v^0}{\partial x^2} \right) = 0 \end{cases} \quad (4.28)$$

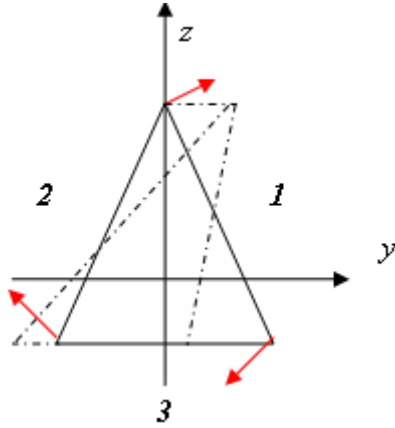


Figure 4-8 Schematic of the coupling between twist and bending in y direction

For the Φ_y , w coordinates we have,

$$\begin{cases} C_3 \left(\phi_y + \frac{\partial w^0}{\partial x} \right) + 4m_3 \frac{\partial^2 \phi_y}{\partial t^2} - C_5 \frac{\partial^2 \phi_y}{\partial x^2} = 0 \\ 4m_1 \frac{\partial^2 w^0}{\partial t^2} - C_3 \left(\frac{\partial^2 w^0}{\partial x^2} + \frac{\partial \phi_y}{\partial x} \right) = 0 \end{cases} \quad (4.29)$$

and for the longitudinal motion, u , the equation of motion has the following form,

$$4m_1 \frac{\partial^2 u^0}{\partial t^2} - C_1 \frac{\partial^2 u^0}{\partial x^2} = 0 \quad (4.30)$$

where,

$$m_1 = \frac{3}{L_L} (A_d L_d \rho_d + A_L L_L \rho_L + A_b L_b \rho_b)$$

$$m_2 = m_3 = \frac{1}{4L_L} L_b^2 (A_d L_d \rho_d + 2A_L L_L \rho_L + A_b L_b \rho_b) \quad (4.31)$$

For the case that the torsional stiffness is really small ($K_t \rightarrow 0$), the joints can be modeled as hinge joints. Therefore, the coefficient C_7 in (4.26) vanishes which results in decoupling the bending along the y coordinate and the torsion. Note that there is no coupling for the bending along the z direction and the torsion. These equations are solved to find the natural frequencies of the system for different joint stiffness values which are presented in the numerical results section. To validate the results experimentally and to compare them against the hinge model, this method is also applied to the planar truss with Pratt Girder configuration. The following section presents the derivations for the lattice structure with this configuration.

4.4 Strain Energy of Pratt Girder Truss

The assumptions regarding the joints with torsional stiffness and the nodal torque balance stated in the previous section is applied to the planar truss of our experiment. Similarly, the strain energy of these members for the tension and bending are calculated. A complete derivation for the bending and extensional strain energy terms are presented in the Appendix E. For the extensional strain energy we have,

$$U_{ext} = \frac{1}{2} A_b E_b L_b \varepsilon_z^2 + \frac{A_d E_d \left(\frac{L_b \varepsilon_x}{\sqrt{2}} + \frac{L_b \varepsilon_z}{\sqrt{2}} + \sqrt{2} L_b \varepsilon_{xz} \right)^2}{2\sqrt{2} L_b} + \frac{A_b E_b \left(L_b^2 \left(\varepsilon_x - \frac{1}{2} L_b \kappa_z \right)^2 + L_b^2 \left(\varepsilon_x + \frac{1}{2} L_b \kappa_z \right)^2 \right)}{2L_b} \quad (4.32)$$

The angles of rotation around the y axis for the longeron and batten members are shown in Figure 4-9.

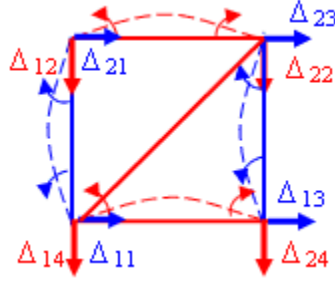


Figure 4-9 Schematic of the planar truss element with members in bending

In a very similar manner to the 3D truss, the strain energy of the longerons and the joints can be found.

4.5 Reduced Order Strain Energy for Pratt girder Truss

Similar to the approach presented in section 4.2, the assumptions for the nodal torque balance must hold to find the reduced order form of the strain energy for the truss element. A beam type theory requires that,

$$\frac{\partial U_e}{\partial \varepsilon_z} = 0 \quad (4.33)$$

where, U_e is the strain energy of the fundamental element. The nodal torque balance assumption can be written in the form:

$$\frac{\partial U_e}{\partial \Theta_i} = 0 \quad (4.34)$$

where, Θ_i 's are the bending angles of the longeron and the batten members in a truss element. Equations (4.33) and (4.34) can be used to solve for the ε_z strain and the rotational components in terms of 3 independent strain components (shear strain, the extensional strain in the x direction and the bending curvature of the cross section). Finally, the relation for the strain energy of the fundamental element can be found as:

$$U_e = G_1 \varepsilon_x^2 + G_2 \varepsilon_{xz}^2 + G_3 \kappa_z^2 + G_4 \kappa_z \varepsilon_x + G_5 \varepsilon_{xz} \varepsilon_x + G_6 \varepsilon_{xz} \kappa_z \quad (4.35)$$

where G_1 to G_7 are constants which depend on the material and geometrical properties of the longerons, battens and the diagonal members. Following Chapter 3 and using the kinematic relations, the strain values can be found in terms of the displacement components. So we get,

$$\begin{aligned}
 U_e = & G_1 \left(\frac{\partial u}{\partial x} \right)^2 + \frac{G_2}{2} \left(\frac{\partial w}{\partial x} + \phi_y \right)^2 + G_3 \left(\frac{\partial \phi_y}{\partial x} \right)^2 + G_4 \frac{\partial \phi_y}{\partial x} \frac{\partial u}{\partial x} + \frac{G_5}{2} \left(\frac{\partial w}{\partial x} + \phi_y \right) \frac{\partial u}{\partial x} \\
 & + \frac{G_6}{2} \left(\frac{\partial w}{\partial x} + \phi_y \right) \frac{\partial \phi_y}{\partial x}
 \end{aligned} \tag{4.36}$$

4.6 Equations of Motion for Pratt Girder Truss

Using the relations for the strain and kinetic energy the governing equations of motion for the structure can be found. These equations for the three coordinates of vibrations are in the form of,

$$\left\{ \begin{aligned}
 & -\frac{L_L^2}{6} (6m_j + 7A_L L_L \rho_L + A_d L_d \rho_d) \frac{\partial^2 \phi_y}{\partial t^2} - G_2 \left(\phi_y + \frac{\partial w}{\partial x} \right) + G_6 \frac{\partial^2 w}{\partial x^2} + 4G_3 \frac{\partial^2 \phi_y}{\partial x^2} - G_5 \frac{\partial u}{\partial x} + 2G_4 \frac{\partial^2 u}{\partial x^2} = 0 \\
 & -2(2m_j + 3A_L L_L \rho_L + A_d L_d \rho_d) \frac{\partial^2 w}{\partial t^2} + G_2 \left(\frac{\partial^2 w}{\partial x^2} + \frac{\partial \phi_y}{\partial x} \right) + G_6 \frac{\partial^2 \phi_y}{\partial x^2} + G_5 \frac{\partial^2 u}{\partial x^2} = 0 \\
 & G_5 \left(\frac{\partial^2 w}{\partial x^2} + \frac{\partial \phi_y}{\partial x} \right) + 2G_4 \frac{\partial^2 \phi_y}{\partial x^2} - 2(2m_j + 3A_L L_L \rho_L + A_d L_d \rho_d) \frac{\partial^2 u}{\partial t^2} + 4G_1 \frac{\partial^2 u}{\partial x^2} = 0
 \end{aligned} \right. \tag{4.37}$$

Using the strain energy relation the stiffness matrix of the element can also be found.

Therefore, the boundary conditions can be rewritten in the following form:

$$\begin{bmatrix} N \\ Q_z \\ M_y \end{bmatrix} = \underbrace{\begin{bmatrix} 2G_1 & \frac{G_5}{2} & G_4 \\ \frac{G_5}{2} & \frac{G_2}{2} & \frac{G_6}{2} \\ G_4 & \frac{G_6}{2} & 2G_3 \end{bmatrix}}_K \begin{bmatrix} \frac{\partial u_0}{\partial x} \\ \frac{\partial w_0}{\partial x} + \phi_y \\ \frac{\partial \phi_y}{\partial x} \end{bmatrix} \quad (4.38)$$

The PDE shown in (4.37) with the boundary conditions in (4.38) are solved to find the natural frequencies and the frequency response functions for this model. Such results are presented in the numerical results section.

4.7 Experimental Setup

To measure the torsional stiffness of the joints for the planar truss a very simple experiment was conducted in the lab. Figures 4-10 and 4-11 show the schematic and the photo of this experimental setup respectively.

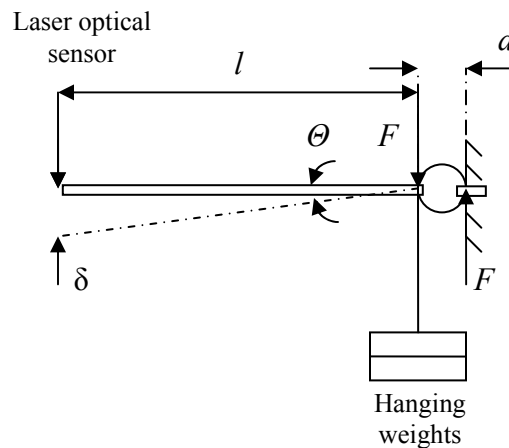


Figure 4-10 A schematic of the experimental setup

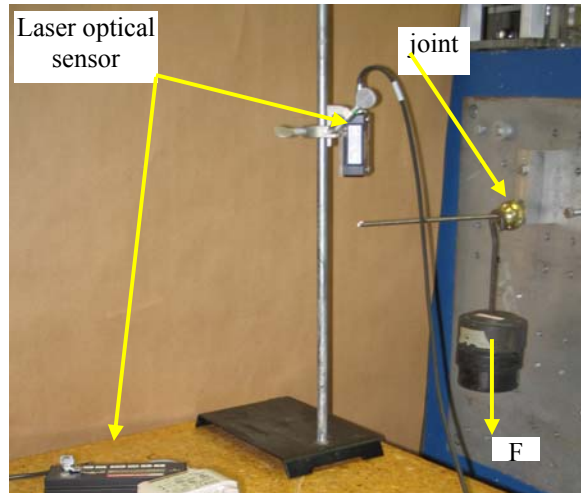


Figure 4-11 Photo of the experimental setup

In this experiment, four static deflection measurements were taken for different weights using a laser optical sensor. The relation for the joint stiffness was simply found using the following relations,

$$T = Fd \quad (4.39)$$

$$K_t = \frac{T}{\theta} \quad (4.40)$$

$$\theta = \frac{\delta}{l} \quad (4.41)$$

where T is the torque, F is the force applied to the joint using the weights shown in the figure, d is the diameter of the joint, l is the length of the steel rod, δ is the static deflection at the tip of the rod, and θ is the angular rotation of the joint. From (4.39), (4.40), and (4.41), the torsional stiffness of the joint can be found as,

$$K_t = \frac{Fdl}{\delta} \quad (4.42)$$

where,

$$d = 1.615(\text{in}) = 0.0410(\text{m}) \quad l = 9\frac{5}{8}(\text{in}) = 0.2445(\text{m}) \quad (4.43)$$

Table 4-2 shows the weights and the static deflection values for four measurements. Using a polyfit function in MATLAB shown in Figure 4-12, the torsional stiffness can easily be found as,

$$K_t \cong 470 \left(\frac{\text{Nm}}{\text{rad}} \right) \quad (4.44)$$

Table 4-2 Static deflection measurements and weight values

Weight- F (grams)	Displacement- δ (mm)
1339	0.172
2239	0.348
4156	0.824
4618	0.939

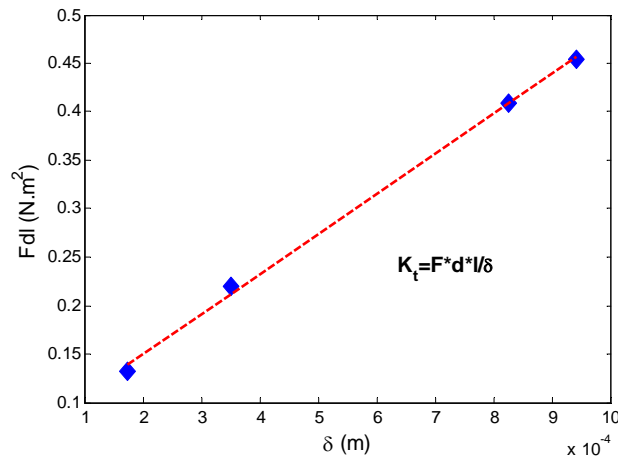


Figure 4-12 A polynomial fit of the torque and torsional strain values

4.8 Numerical Results

The natural frequencies for the 3D truss structure of different lengths, longeron cross-sectional area and joint stiffness values are presented in Tables 4-3 to 4-10. The results here are presented for the coupled torsional-bending system. As can be seen from these results, the smaller the length of the truss the more sensitive the natural frequencies to the variation of the joints stiffness. Therefore, for smaller lengths modeling the joints becomes more significant. Also, it can be observed that the frequencies are smaller for the structures with a larger cross-sectional area. This is because the longerons contribute more to the mass of the truss than to the stiffness. Therefore, as a result of increasing the cross section, the change in the mass of the truss is more significant than the stiffness and the frequencies decrease. It is also shown that the larger the area of the longerons, the more sensitive the frequencies to the joints' stiffness. This is clear because for the longeron members of larger area bending of the members play a more dominant role to the overall strain energy of the truss. Finally, the torsional modes are more susceptible to change with the joints stiffness values.

Table 4-3 Natural frequencies for $L=12\text{ m}$ and $A_L=0.00729659\text{ m}^2$

ω (rad/sec.)	ω (rad/sec.)	ω (rad/sec.)	ω (rad/sec.)	ω (rad/sec.)	ω (rad/sec.)
$K_t=0$ (Nm/rad)	$K_t=40$ (Nm/rad)	$K_t=6000$ (Nm/rad)	$K_t=8000$ (Nm/rad)	$K_t=40000$ (Nm/rad)	rigid joint $K_t=infinity$
35.7 ^T	35.8 ^T	35.9 ^T	36.0 ^T	36.7 ^T	150.2 ^T
71.5 ^T	71.5 ^T	71.8 ^T	71.9 ^T	73.5 ^T	173.9 ^T
100.5 ^b	100.5 ^b	100.6 ^b	100.6 ^b	100.9 ^b	232.3 ^b
107.2 ^T	107.3 ^T	107.7 ^T	107.9 ^T	110.2 ^T	283.2 ^T
130.1 ^b	130.1 ^b	130.2 ^b	130.2 ^b	130.6 ^b	306.6 ^b
143.0 ^T	143.0 ^T	143.5 ^T	143.8 ^T	146.8 ^T	312.6 ^T
157.8 ^b	157.8 ^b	157.9 ^b	157.9 ^b	158.4 ^b	350.5 ^b
174.0 ^b	174.0 ^b	174.1 ^b	174.1 ^b	174.6 ^b	443.2 ^b
178.7 ^T	178.8 ^T	179.5 ^T	179.8 ^T	183.6 ^T	470.3 ^T
201.6 ^b	201.6 ^b	201.7 ^b	201.7 ^b	202.2 ^b	526.5 ^b
214.5 ^T	214.6 ^T	215.4 ^T	215.7 ^T	220.3 ^T	616.0 ^T
250.3 ^T	250.3 ^T	251.3 ^T	251.7 ^T	255.5 ^T	626.0 ^T
254.6 ^b	254.6 ^b	254.8 ^b	254.8 ^b	257.0 ^b	702.5 ^b
286.0 ^T	286.1 ^T	287.2 ^T	287.6 ^T	293.7 ^T	782.5 ^T
302.5 ^b	302.5 ^b	302.6 ^b	302.7 ^b	303.5 ^b	791.0 ^b
321.8 ^T	321.8 ^T	323.2 ^T	323.6 ^T	330.5 ^T	878.0 ^T
353.7 ^b	353.8 ^b	353.9 ^b	354.0 ^b	355.0 ^b	938.5 ^b
357.5 ^T	357.6 ^T	359.0 ^T	359.5 ^T	367.1 ^T	966.5 ^T
393.3 ^T	393.4 ^T	394.9 ^T	395.4 ^T	403.8 ^T	1053.8 ^T
403.4 ^b	403.4 ^b	403.6 ^b	403.7 ^b	404.8 ^b	1142.0 ^b
429.0 ^T	429.1 ^T	430.8 ^T	431.4 ^T	440.5 ^T	1230.0 ^T

^b bending

^T Torsion

Table 4-4 Natural frequencies for $L=30\text{ m}$ and $A_L=0.00729659\text{ m}^2$

ω (rad/sec.)	ω (rad/sec.)	ω (rad/sec.)	ω (rad/sec.)	Ω (rad/sec.)	ω (rad/sec.)
$K_t=0$ (Nm/rad)	$K_t=40$ (Nm/rad)	$K_t=6000$ (Nm/rad)	$K_t=8000$ (Nm/rad)	$K_t=40000$ (Nm/rad)	rigid joint $K_t=\text{infinity}$
14.3 ^T	14.3 ^T	14.4 ^T	14.4 ^T	14.7 ^T	60.6 ^T
28.6 ^T	28.6 ^T	28.7 ^T	28.8 ^T	29.38 ^T	65.97 ^T
39.5 ^b	39.5 ^b	39.5 ^b	39.5 ^b	39.6 ^b	98.6 ^b
42.9 ^T	42.9 ^T	43.1 ^T	43.2 ^T	44.1 ^T	124.5 ^T
56.9 ^b	56.9 ^b	56.9 ^b	56.9 ^b	57.12 ^b	138.4 ^b
57.2 ^T	57.2 ^T	57.44 ^T	57.5 ^T	58.74 ^T	186.6 ^T
71.5 ^T	71.5 ^T	71.8 ^T	71.9 ^T	73.42 ^T	209.4 ^T
80.2 ^b	80.3 ^b	80.3 ^b	80.3 ^b	80.53 ^b	238.85 ^b
85.8 ^T	85.8 ^T	86.2 ^T	86.3 ^T	88.1 ^T	279.9 ^T
97.9 ^b	98.0 ^b	98.0 ^b	98.0 ^b	98.3 ^b	281.25 ^b
100.1 ^T	100.1 ^T	100.5 ^T	100.6 ^T	102.8 ^T	283.1 ^T
114.4 ^T	114.4 ^T	114.9 ^T	115.1 ^T	117.5 ^T	313.3 ^T
120.8 ^b	120.8 ^b	120.8 ^b	120.8 ^b	121.1 ^b	321.4 ^b
128.7 ^T	128.7 ^T	129.3 ^T	129.4 ^T	132.15 ^T	350.5 ^T
136.5 ^b	136.5 ^b	136.6 ^b	136.6 ^b	136.95 ^b	375.15 ^b
143.0 ^T	143.0 ^T	143.6 ^T	143.8 ^T	146.85 ^T	387.5 ^T
157.3 ^T	157.4 ^T	157.92 ^T	157.9 ^T	158.4 ^T	420.8 ^T
157.8 ^b	157.8 ^b	157.98 ^b	159.1 ^b	159.55 ^b	438.1 ^b
159.0 ^b	159.0 ^b	159.07 ^b	161.3 ^b	161.72 ^b	457.1 ^b
161.2 ^b	161.2 ^b	161.3 ^b	172.6 ^b	176.2 ^b	491.1 ^b
171.6 ^T	171.6 ^T	172.4 ^T	184.1 ^T	184.5 ^T	500.4 ^T

^b bending
^T Torsion

Table 4-5 Natural frequencies for $L=60\text{ m}$ and $A_L=0.00729659\text{ m}^2$

ω (rad/sec.)	ω (rad/sec.)	ω (rad/sec.)	ω (rad/sec.)	ω (rad/sec.)	ω (rad/sec.)
$K_t=20$ (Nm/rad)	$K_t=40$ (Nm/rad)	$K_t=6000$ (Nm/rad)	$K_t=8000$ (Nm/rad)	$K_t=40000$ (Nm/rad)	rigid joint $K_t=\text{infinity}$
7.15 ^T	7.15 ^T	7.18 ^T	7.19 ^T	7.35 ^T	28.25 ^T
14.30 ^T	14.3 ^T	14.36 ^T	14.38 ^T	14.7 ^T	30.35 ^T
18.6 ^b	18.6 ^b	18.575 ^b	18.58 ^b	18.6 ^b	47.1 ^b
21.45 ^T	21.4 ^T	21.54 ^T	21.57 ^T	22.03 ^T	61.6 ^T
28.1 ^b	28.1 ^b	28.15 ^b	28.15 ^b	28.2 ^b	66.9 ^b
28.61 ^T	28.6 ^T	28.75 ^T	28.75 ^T	29.4 ^T	84.25 ^T
35.76 ^T	35.8 ^T	35.9 ^T	35.95 ^T	36.7 ^T	93.15 ^T
39.6 ^b	39.6 ^b	39.56 ^b	39.55 ^b	39.65 ^b	102.99 ^b
42.91 ^T	42.9 ^T	43.1 ^T	43.15 ^T	44.05 ^T	120.4 ^T
49.2 ^b	49.1 ^b	49.15 ^b	49.15 ^b	49.3 ^b	124.6 ^b
50.06 ^T	50.1 ^T	50.3 ^T	50.3 ^T	51.4 ^T	138.7 ^T
57.21 ^T	57.2 ^T	57.5 ^T	57.5 ^T	58.75 ^T	155.1 ^T
60.0 ^b	60 ^b	60.0 ^b	60.00 ^b	60.2 ^b	156.7 ^b
64.37 ^T	64.4 ^T	64.62 ^T	64.7 ^T	66.1 ^T	174.2 ^T
69.5 ^b	69.6 ^b	69.65 ^b	69.65 ^b	69.8 ^b	187.3 ^b
71.52 ^T	71.6 ^T	71.8 ^T	71.9 ^T	73.4 ^T	191.25 ^T
78.67 ^T	78.7 ^T	79.0 ^T	79.1 ^T	80.55 ^T	209.5 ^T
80.3 ^b	80.3 ^b	80.3 ^b	80.35 ^b	80.75 ^b	218.35 ^b
85.82 ^T	85.8 ^T	86.2 ^T	86.3 ^T	88.1 ^T	226.4 ^T
89.9 ^b	89.9 ^b	89.94 ^b	89.95 ^b	90.2 ^b	244.7 ^b
92.97 ^T	93.0 ^T	93.35 ^T	93.45 ^T	95.45 ^T	250.0 ^T

^b bending
^T Torsion

Table 4-6 Natural frequencies for $L=300\text{ m}$ and $A_L=0.00729659\text{ m}^2$

ω (rad/sec.)	ω (rad/sec.)	ω (rad/sec.)	ω (rad/sec.)	ω (rad/sec.)	ω (rad/sec.)
$K_t=0$ (Nm/rad)	$K_t=40$ (Nm/rad)	$K_t=6000$ (Nm/rad)	$K_t=8000$ (Nm/rad)	$K_t=40000$ (Nm/rad)	rigid joint $K_t=\text{infinity}$
1.43 ^T	1.43 ^T	1.44 ^T	1.44 ^T	1.47 ^T	1.8 ^T
1.70 ^b	1.70 ^b	1.70 ^b	1.71 ^b	1.71 ^b	4.60 ^b
2.86 ^T	2.86 ^T	2.87 ^T	2.88 ^T	2.94 ^T	6.08 ^T
3.86 ^b	3.86 ^b	3.86 ^b	3.86 ^b	3.87 ^b	8.12 ^b
4.29 ^T	4.30 ^T	4.31 ^T	4.32 ^T	4.41 ^T	11.97 ^T
5.72 ^T	5.72 ^T	5.75 ^T	5.75 ^T	5.89 ^T	12.18 ^T
6.20 ^b	6.20 ^b	6.18 ^b	6.18 ^b	6.20 ^b	15.92 ^b
7.15 ^T	7.20 ^T	7.18 ^T	7.19 ^T	7.34 ^T	18.30 ^T
8.47 ^b	8.50 ^b	8.47 ^b	8.47 ^b	8.49 ^b	19.90 ^b
8.58 ^T	8.60 ^T	8.62 ^T	8.63 ^T	8.81 ^T	23.70 ^T
10.01 ^T	10.012 ^T	10.05 ^T	10.05 ^T	10.28 ^T	24.59 ^T
10.70 ^b	10.70 ^b	10.70 ^b	10.70 ^b	10.75 ^b	27.65 ^b
11.44 ^T	11.40 ^T	11.50 ^T	11.50 ^T	11.75 ^T	30.75 ^T
12.87 ^T	12.87 ^T	12.90 ^T	12.90 ^T	12.93 ^T	31.50 ^T
12.89 ^b	12.89 ^b	12.93 ^b	12.95 ^b	13.22 ^b	35.30 ^b
14.30 ^T	14.30 ^T	14.35 ^T	14.40 ^T	14.70 ^T	36.95 ^T
15.05 ^b	15.05 ^b	15.05 ^b	15.06 ^b	15.10 ^b	39.06 ^b
15.73 ^T	15.75 ^T	15.80 ^T	15.82 ^T	16.15 ^T	42.60 ^T
17.16 ^T	17.16 ^T	17.19 ^T	17.19 ^T	17.23 ^T	43.35 ^T
17.18 ^b	17.17 ^b	17.23 ^b	17.26 ^b	17.63 ^b	46.45 ^b
18.59 ^T	18.60 ^T	18.67 ^T	18.70 ^T	19.09 ^T	49.50 ^T

^b bending

^T Torsion

Table 4-7 Natural frequencies for $L=12\text{ m}$ and $A_L=0.00024322\text{ m}^2$

ω (rad/sec.)	ω (rad/sec.)	ω (rad/sec.)	ω (rad/sec.)	ω (rad/sec.)	ω (rad/sec.)
$K_s=0$ (Nm/rad)	$K_s=40$ (Nm/rad)	$K_s=6000$ (Nm/rad)	$K_s=8000$ (Nm/rad)	$K_s=40000$ (Nm/rad)	rigid joint $K_s=\text{infinity}$
174.4 ^T	174.4 ^T	175.1 ^T	175.3 ^T	177.4 ^T	180.4 ^T
348.8 ^T	348.8 ^T	350.3 ^T	350.7 ^T	354.9 ^T	360.7 ^T
420.2 ^b	420.2 ^b	420.4 ^b	420.4 ^b	420.9 ^b	421.6 ^b
523.2 ^T	523.2 ^T	525.4 ^T	526.0 ^T	532.3 ^T	541.1 ^T
599.9 ^b	600.0 ^b	600.2 ^b	600.3 ^b	601.1 ^b	602.3 ^b
697.65 ^T	697.7 ^T	700.5 ^T	701.4 ^T	709.8 ^T	721.5 ^T
785.8 ^b	785.8 ^b	786.2 ^b	786.3 ^b	787.5 ^b	789.1 ^b
833.5 ^b	833.5 ^b	833.9 ^b	834.0 ^b	835.2 ^b	836.9 ^b
872.1 ^T	872.1 ^T	875.6 ^T	876.7 ^T	887.2 ^T	901.8 ^T
905.6 ^b	905.6 ^b	906.1 ^b	906.2 ^b	907.4 ^b	909.2 ^b
1046.5 ^T	1046.5 ^T	1050.8 ^T	1052.1 ^T	1064.6 ^T	1082.2 ^T
1170.7 ^b	1170.7 ^b	1171.2 ^b	1171.4 ^b	1173.1 ^b	1175.5 ^b
1220.9 ^T	1220.9 ^T	1225.9 ^T	1227.4 ^T	1242.1 ^T	1262.6 ^T
1369.4 ^b	1369.4 ^b	1370.1 ^b	1370.2 ^b	1372.1 ^b	1374.7 ^b
1395.3 ^T	1395.3 ^T	1401.0 ^T	1402.8 ^T	1419.5 ^T	1442.9 ^T
1569.7 ^T	1569.7 ^T	1576.2 ^T	1578.1 ^T	1597.0 ^T	1623.3 ^T
1627.9 ^b	1628.0 ^b	1628.8 ^b	1629.0 ^b	1631.4 ^b	1634.7 ^b
1668.4 ^b	1668.5 ^b	1668.8 ^b	1668.9 ^b	1669.8 ^b	1671.1 ^b
1744.1 ^T	1744.2 ^T	1751.3 ^T	1753.4 ^T	1774.4 ^T	1803.7 ^T
1880.5 ^b	1880.5 ^b	1881.4 ^b	1881.7 ^b	1884.2 ^b	1887.9 ^b
1918.5 ^T	1918.6 ^T	1926.4 ^T	1928.8 ^T	1951.9 ^T	1984.1 ^T

^b bending

^T Torsion

Table 4-8 Natural frequencies for $L=30\text{ m}$ and $A_L=0.00024322\text{ m}^2$

ω (rad/sec.)	ω (rad/sec.)	ω (rad/sec.)	ω (rad/sec.)	ω (rad/sec.)	ω (rad/sec.)
$K_r=0$ (Nm/rad)	$K_r=40$ (Nm/rad)	$K_r=6000$ (Nm/rad)	$K_r=8000$ (Nm/rad)	$K_r=40000$ (Nm/rad)	rigid joint $K_r=\text{infinity}$
69.76 ^T	69.80 ^T	70.10 ^T	70.10 ^T	71.0 ^T	72.1 ^T
120.12 ^b	120.10 ^b	120.10 ^b	120.10 ^b	120.2 ^b	120.3 ^b
139.53 ^T	139.50 ^T	140.10 ^T	140.30 ^T	142.0 ^T	144.3 ^T
209.29 ^T	209.30 ^T	210.20 ^T	210.40 ^T	212.9 ^T	216.4 ^T
225.71 ^b	225.70 ^b	225.80 ^b	225.80 ^b	226.0 ^b	226.4 ^b
279.06 ^T	279.10 ^T	280.20 ^T	280.60 ^T	283.9 ^T	288.6 ^T
332.17 ^b	332.20 ^b	332.30 ^b	332.30 ^b	332.7 ^b	333.3 ^b
348.82 ^T	348.80 ^T	350.30 ^T	350.70 ^T	354.9 ^T	360.7 ^T
418.59 ^T	418.60 ^T	420.30 ^T	420.80 ^T	425.9 ^T	430.9 ^b
429.30 ^b	429.30 ^b	429.50 ^b	429.50 ^b	430.1 ^b	432.9 ^T
488.35 ^T	488.40 ^T	490.40 ^T	491.00 ^T	496.8 ^T	505.0 ^T
529.22 ^b	529.20 ^b	529.50 ^b	529.50 ^b	530.2 ^b	531.2 ^b
558.12 ^T	558.10 ^T	560.40 ^T	561.10 ^T	567.8 ^T	577.2 ^T
618.98 ^b	619.00 ^b	619.30 ^b	619.40 ^b	620.2 ^b	621.4 ^b
627.88 ^T	627.90 ^T	630.50 ^T	631.20 ^T	638.8 ^T	649.3 ^T
697.65 ^T	697.70 ^T	700.50 ^T	701.40 ^T	709.8 ^T	721.3 ^T
718.56 ^b	718.60 ^b	718.90 ^b	719.00 ^b	720.0 ^b	721.5 ^b
766.68 ^b	766.70 ^b	767.10 ^b	767.20 ^b	768.3 ^b	769.8 ^b
767.41 ^T	767.40 ^T	770.60 ^T	771.50 ^T	780.7 ^T	789.1 ^T
785.84 ^b	785.80 ^b	786.20 ^b	786.30 ^b	787.5 ^b	793.6 ^b

^b bending

^T Torsion

Table 4-9 Natural frequencies for $L=60\text{ m}$ and $A_L=0.00024322\text{ m}^2$

ω (rad/sec.)	ω (rad/sec.)	ω (rad/sec.)	ω (rad/sec.)	ω (rad/sec.)	ω (rad/sec.)
$K_t=0$ (Nm/rad)	$K_t=40$ (Nm/rad)	$K_t=6000$ (Nm/rad)	$K_t=8000$ (Nm/rad)	$K_t=40000$ (Nm/rad)	rigid joint $K_t=\text{infinity}$
34.88 ^T	34.90 ^T	35.00 ^T	35.10 ^T	35.50 ^T	36.10 ^T
36.44 ^b	36.40 ^b	36.40 ^b	36.40 ^b	36.40 ^b	36.50 ^b
69.76 ^T	69.80 ^T	70.10 ^T	70.10 ^T	71.00 ^T	72.10 ^T
84.28 ^b	84.30 ^b	84.30 ^b	84.30 ^b	84.30 ^b	84.40 ^b
104.65 ^T	104.70 ^T	105.10 ^T	105.20 ^T	106.50 ^T	108.20 ^T
137.20 ^b	137.20 ^b	137.20 ^b	137.30 ^b	137.40 ^b	137.50 ^b
139.53 ^T	139.50 ^T	140.10 ^T	140.30 ^T	142.00 ^T	144.30 ^T
174.41 ^T	174.40 ^T	175.10 ^T	175.30 ^T	177.40 ^T	180.40 ^T
189.90 ^b	189.90 ^b	190.00 ^b	190.00 ^b	190.20 ^b	190.50 ^b
209.29 ^T	209.30 ^T	210.20 ^T	210.40 ^T	212.90 ^T	216.40 ^T
241.80 ^b	241.80 ^b	241.90 ^b	241.90 ^b	242.20 ^b	242.60 ^b
244.18 ^T	244.20 ^T	245.20 ^T	245.50 ^T	248.40 ^T	252.50 ^T
279.06 ^T	279.10 ^T	280.20 ^T	280.60 ^T	283.90 ^T	288.60 ^T
292.55 ^b	292.60 ^b	292.70 ^b	292.70 ^b	293.10 ^b	293.60 ^b
313.94 ^T	313.90 ^T	315.20 ^T	315.60 ^T	319.40 ^T	324.70 ^T
342.60 ^b	342.60 ^b	342.70 ^b	342.80 ^b	343.20 ^b	343.80 ^b
348.82 ^T	348.80 ^T	350.30 ^T	350.70 ^T	354.90 ^T	360.70 ^T
383.71 ^T	383.70 ^T	385.30 ^T	385.80 ^T	390.40 ^T	393.30 ^T
391.80 ^b	391.80 ^b	392.00 ^b	392.10 ^b	392.60 ^b	396.80 ^b
418.59 ^T	418.60 ^T	420.30 ^T	420.80 ^T	425.90 ^T	432.90 ^T
440.65 ^b	440.60 ^b	440.80 ^b	440.90 ^b	441.50 ^b	442.30 ^b

^b bending

^T Torsion

Table 4-10 Natural frequencies for $L=300\text{ m}$ and $A_L=0.00024322\text{ m}^2$

ω (rad/sec.)	ω (rad/sec.)	ω (rad/sec.)	ω (rad/sec.)	ω (rad/sec.)	ω (rad/sec.)
$K_T=0$ (Nm/rad)	$K_T=40$ (Nm/rad)	$K_T=6000$ (Nm/rad)	$K_T=8000$ (Nm/rad)	$K_T=40000$ (Nm/rad)	rigid joint $K_T=\text{infinity}$
1.58 ^b	1.59 ^b	1.59 ^b	1.59 ^b	1.59 ^b	1.59 ^b
4.33 ^b	4.33 ^b	4.33 ^b	4.33 ^b	4.33 ^b	4.33 ^b
6.98 ^T	6.98 ^T	7.01 ^T	7.01 ^T	7.10 ^T	7.21 ^T
8.36 ^b	8.36 ^b	8.36 ^b	8.36 ^b	8.36 ^b	8.36 ^b
13.54 ^b	13.54 ^b	13.54 ^b	13.54 ^b	13.54 ^b	13.55 ^b
13.95 ^T	13.95 ^T	14.01 ^T	14.03 ^T	14.20 ^T	14.43 ^T
19.75 ^b	19.75 ^b	19.75 ^b	19.75 ^b	19.75 ^b	19.76 ^b
20.93 ^T	20.93 ^T	21.02 ^T	21.04 ^T	21.29 ^T	21.64 ^T
26.83 ^b	26.83 ^b	26.83 ^b	26.83 ^b	26.84 ^b	26.85 ^b
27.90 ^T	27.91 ^T	28.02 ^T	28.06 ^T	28.39 ^T	28.86 ^T
34.64 ^b	34.64 ^b	34.65 ^b	34.65 ^b	34.66 ^b	34.67 ^b
34.88 ^T	34.88 ^T	35.03 ^T	35.07 ^T	35.49 ^T	36.07 ^T
41.86 ^T	41.86 ^T	42.03 ^T	42.08 ^T	42.59 ^T	43.10 ^T
43.05 ^b	43.05 ^b	43.06 ^b	43.06 ^b	43.08 ^b	43.29 ^b
48.84 ^T	48.84 ^T	49.04 ^T	49.10 ^T	49.68 ^T	50.50 ^T
51.95 ^b	51.95 ^b	51.95 ^b	51.96 ^b	51.98 ^b	52.01 ^b
55.81 ^T	55.81 ^T	56.04 ^T	56.11 ^T	56.78 ^T	57.72 ^T
61.21 ^b	61.22 ^b	61.23 ^b	61.23 ^b	61.26 ^b	61.31 ^b
62.79 ^T	62.79 ^T	63.05 ^T	63.12 ^T	63.88 ^T	64.93 ^T
69.76 ^T	69.77 ^T	70.05 ^T	70.14 ^T	70.83 ^T	70.89 ^T
70.78 ^b	70.77 ^b	70.79 ^b	70.79 ^b	70.98 ^b	72.15 ^b

^b bending

^T Torsion

To validate this micro-polar continuum modeling technique experimentally, the frequency response functions of the truss structure with the Pratt Girder configuration was used. Figure 4-13 shows a comparison between the results of the theory and experiment. The results for the natural frequencies of the two models (hinge and micropolar) are also shown in Table 4-11. It is shown that the results for the micro-polar-based continuum model has better accuracy (2% frequency estimation errors) compared to the hinge model particularly for the higher modes.

Table 4-11 Experimental and theoretical natural frequencies in Hz

Mode	micro-polar model	error	hinge model	error	experiment
1	6.8	1.09%	6.88	0.07%	6.875
2	152.5	0.33%	154	0.65%	153
3	319.3	1.45%	319	1.54%	324
4	441.9	0.47%	491	10.6%	444

Finally to perform a sensitivity analysis, the frequency values were found for a higher stiffness values. For this purpose a joint stiffness value of 1000 (Nm/rad) was chosen. The frequency values of 6.8, 292.05, 429.08, 473.96 (Hz) were found, meaning that the assumption of joints with higher stiffness values or rigid joints, as suggested by Noor et. al.,⁴⁵ in general results in lower accuracy for the frequencies of such structures. It should also be noted that to get these results some of the physical parameters were updated. A mass of approximately 9 grams (0.2% of the mass of the truss) was added to the joints and a value of 1.0 mm was also subtracted from the diameter of the diagonal members. This might raise a question if updating the values for the hinge joint model could result in the same accuracy as this model. To show this can not be the case, the parameters of the hinge model was altered to obtain better results for the higher modes. As a result the frequency values of 6.8, 150.72, 319.11, 479.37 (Hz) were obtained. It can be seen that the 4th natural frequency of the system is still off by 35 (Hz) when compared to the experiment (an error value of approximately 8%).

As it is shown in Figure 4-13, the peak for the 4th natural frequency is wider in the experimental FRF compared to the theory. This is simply because of the effects of the damping which is ignored in this model. In general in a mechanical system, the higher the frequency the mode is highly damped.² Therefore, this is more noticeable for the 4th frequency which essentially has higher damping than the lower modes. Also the natural

frequencies are estimated better than the FRF by this model. This is because usually the system's mode shapes are more susceptible to changes as a result of the variations of the system's parameters. So the simplified assumptions to reduce the order of the model affect the magnitude of the FRF more than the frequencies which results in better accuracy for the frequencies than the FRF magnitudes. This effect is shown more clearly for the 4th frequency shown in Figure 4-13.

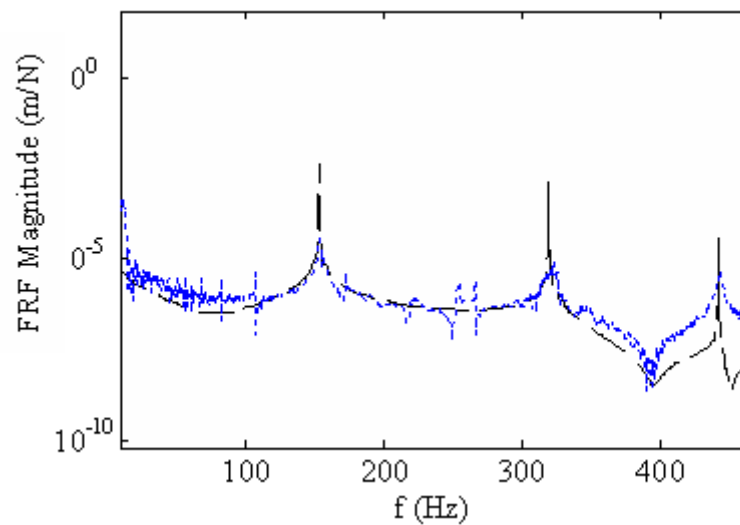


Figure 4-13 FRF **after** modeling joints

4.9 Concluding Remarks

A micropolar continuum modeling technique is developed for both the three-dimensional space truss and a planar truss with Pratt Girder configuration with flexible joints. Assuming that the mass moment of inertia is negligible for the individual components, an assumption of the nodal torque balance for the structure should hold. This assumption induces a constraint on the strain field for the elements of structure which results in a coupling between the micro-rotations and the independent strain states that are the same as those of the continuum model. Therefore, the effects of the torsional flexibility of the

joints and the micro-rotations of the members are preserved while a one-dimensional model is derived for the system. As a result the frequency response function and the frequency estimations are improved significantly for higher frequencies.

Chapter 5

Thermally Induced Vibrations

5.1 Introduction

The successful operation of any system requires precise understanding of the disturbances and its design criteria. For most space structures, the critical loads that the satellites encounter during launch are more important; the smaller loads during the operation are of secondary importance.⁵⁵ Inflatable structures, however, are stowed during launch and will be deployed upon reaching the destination orbit. Therefore, the critical loads in the space environment become of particular importance. A complete list of different kinds of disturbances in space environment is given in Ref. 55. Some examples of such disturbances are: gravity gradient forces, solar radiation pressure, magnetic fields, atmospheric drag and thermal loads. One of the most important environmental disturbances is the thermal loading. There are three known sources of radiation in space environment: 1) direct solar, 2) earth solar reflection (albedo), and 3) direct earth (infrared). The effects of the last two are less significant for orbits higher than the LEO orbit.⁵⁶ When a satellite goes through an eclipse, rapid temperature changes are

induced to the system. According to Thornton et. al.⁵⁷ the solar heating experienced by a satellite can change up to 95% dependent upon how long the transitions through the Penumbra (partial Earth shadow) and Umbra (full Earth shadow) takes (see Figure 5-1). As a result, the torques and moments induced in the system can increase the jitter, corrupt the pointing accuracy of the spacecraft and can cause spacecraft attitude problems, quasi-static deformations, unexpected thermal oscillations and in some cases even thermal flutter or instability. Figure 5-2 shows the Solar Array Flight Experiment (SAFE) that had unexpected deflections after its transition thorough the Earth shadow. Some of the problems with solar radiation in space such as thermally induced vibrations, thermal buckling, surface degradation and thermal stress are discussed in Refs. 58, 59, 60, and 15. The thermal environment in space can also affect a structure in other ways. For example, material properties might be temperature dependent or deformation and/or cracking of materials can occur as a result of the constant diffusion to the space. The temperature changes in space can be around 100 °C on sunlight surfaces, and as low as -100 °C on cold/shadow side.⁶¹

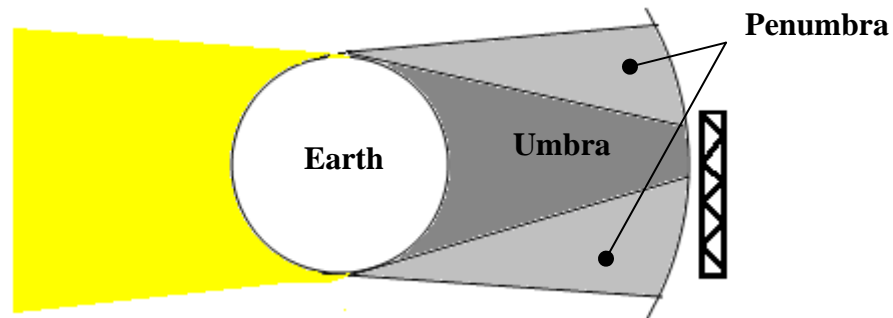


Figure 5-1 Schematic view of the Earth shadow on the Satellite (full and partial shadows)

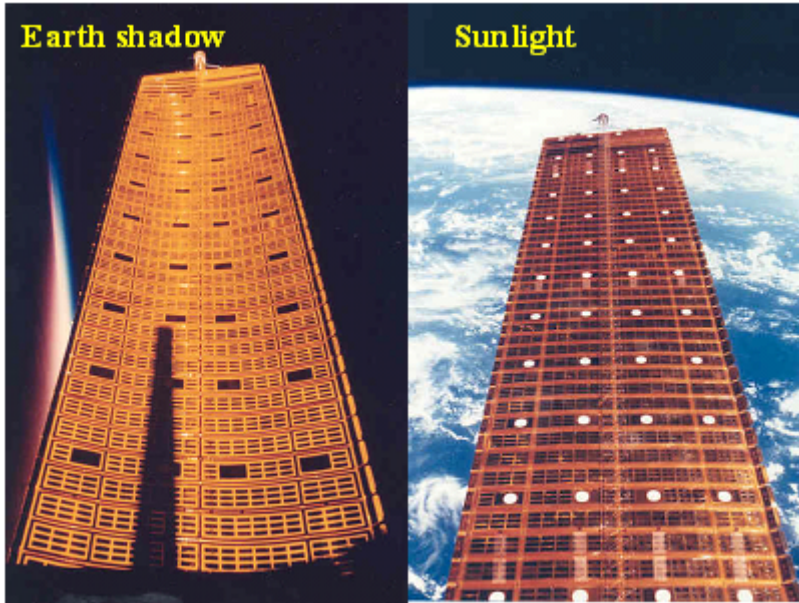


Figure 5-2 Photos of the SAFE courtesy of NASA Langley Research Center

The phenomenon of thermally induced vibrations was first examined by Boley in the late 1950s.⁶⁶ His analyses involve beams subjected to an instantaneous heat flux which results in a vibratory response. In the 1960s, a series of 6 Earth Orbiting spacecraft (Orbiting Geophysical Observatories-OGOs) were launched by the United States. In the early days of operation OGO I-III had some unexpected oscillations. In 1968, scientists found out that thermally induced vibrations were the source of this problem.⁶² The first experiment on thermally induced vibrations was performed at NASA Ames by Beam in 1968.⁶³

Most space structures have appendages with very low natural frequencies and therefore, susceptible to the low frequency disturbances. Thus, thermally induced disturbances remain a problem even for contemporary spacecraft. Such disturbances can be classified in four different categories:^{64, 65} 1) Thermal bending or torsion 2) Thermal snap 3) Thermally induced vibrations, and 4) Thermal flutter. Thermal bending is a

quasi-static deformation that is caused by slowly varying temperatures during non-transitional sunlight. These deformations result in a change in the inertia of a spacecraft which leads to corresponding changes in the gravity gradient torques acting on the system. Many space structures should be designed so that their overall moments of inertia correspond to those required for their gravitational stabilization.⁶⁶ The thermal snap is a non-oscillatory motion which is caused by an impulsive torque on the spacecraft due to rapid heating or cooling of its appendages. Because there is no external force involved in this process and such deformations are the structural response to the internal forces, the total angular momentum of the satellite is conserved. As a result, there will be a change in the kinetic energy due to the input solar heating, while there is no change in the overall momentum of the system. Therefore, to keep the momentum unaltered the satellite goes through a rigid body rotation which is called a thermal snap.⁶⁷ This can be of particular importance for structures with an unstable dynamic configuration (not a pointing satellite) where the gravity gradients do not help with their stabilization. The thermally induced disturbances experienced by the LANDSAT, Upper Atmosphere Research satellite, TOPEX and the Communications Technology Satellite can be best illustrated by the snap phenomenon. Finally, thermally induced vibrations are oscillatory responses as a result of the instantaneous time varying temperatures in space. Such motions can become unstable (thermal flutter) which first occurred in the late 1960's when satellites with extremely long gravity gradient booms of low rigidity were placed in orbit.^{68, 69}

Some examples of the satellites whose performance have been debilitated by the thermally induced motions are:⁷⁰ Hubble Space Telescope, Ulysses⁷¹ (1990-1991), Upper Atmosphere Research Satellite-UARS⁷² (1991), LANDSAT-4/5 (1980), Communications

Technology Satellite-CTS (1978), Voyager (1977), Apollo 15 Command and Service Module (CSM) (1977), Explorer 45 (1971), NRL (1969), GGSE-III-VI (1968-1969), OGO-10 (1967), OV-10 (1966), Explorer XX (1964), and Alouette 1 (1962).

The following literature reveals the previous research and analysis in the area of the thermally induced disturbances for different space structures. Additionally, Thornton has a complete survey for the design, evolution and lessons to be learned for the thermal space structures.^{73, 74} One such example is the Hubble Space Telescope which had numerous anomalous behaviors after its first launch in 1990. Some of these problems were an incorrectly fabricated primary mirror, pointing disturbance and jitter. Each of the solar array wings of the HST had four booms, two per blanket. Upon deployment of each wing, the booms for one blanket were faced toward the sun while the booms for the other blanket were oriented away from the sun which resulted in the thermally induced vibrations in the solar array wings. These problems were later fixed by modifying the control system that could compensate for the low frequency thermal disturbances and designing a new blanket with embedded sunshields that would easily deploy and retract with the booms.⁷⁵ This was the primary task of the in-orbit repair mission by the astronauts in 1993 (flight STS-61). There have been many studies on the unexpected vibrations of the HST solar array booms as a result of the eclipse transitions. References 76, 77 and 78 are some of the examples. Another work is done by Chung et. al.⁷⁹ that investigates the coupled thermal torsional-bending modes in the Hubble. The authors show that the low-frequency-large-amplitude coupled torsional-bending modes were responsible for the failure of the operation of this spacecraft. Etkin and Hughes⁸⁰ performed some studies to explain the progressive loss of spin of Alouette I and Explorer

XX satellites as a result of the thermally induced vibrations. Frisch,⁸¹ has a complete analysis of the thermally induced bending and twist of gravity gradient booms made of cylinders with open sections. The author states that for a general case where the deflection angle is not small, the assumptions of Timoshenko regarding the bending and twist being separable can not be applied. Therefore, a coupled numerical analysis is performed to solve for the twist and the bending of this structure. OGO-IV had some anomalous motion which lasted almost a year which led to a hypothesis that the structure was affected by some unstable thermally induced vibrations. Koval and Donohue modeled the thermally induced vibrations in the OGO-IV spacecraft. In their analysis they model the structure using a cylindrical beam with an open cross section which has an offset between the mass center and the shear center.^{82, 68} Both bending and twist induced vibrations of the booms of Apollo 15 Command and Service Module (CSM) are analyzed by Kumar⁸³. The effect of thermal shock on bending and attitude response of free-free beam and plate (a general solar array) is studied by Bainum⁸⁴. Ramesh et. al.⁶⁹ studied the radiation thermal effects on the orbital motion attitude motion and axial deformation of very large axially flexible space structures with a planar pitch motion around the earth. Another example of a satellite that was troubled with the thermally induced disturbances was the TOPEX (a joint US French project sponsored by NASA). The thermal structural response analysis of TOPEX satellite is presented in Refs. 85, and 86. The authors⁸⁵ show that the sunrise/ sunset is primarily a roll/yaw disturbance. They design a Normal Mission Mode PID controller for the TOPEX satellite. Lambertson et. al.⁷² investigated the UARS (the Upper Atmosphere Research satellite) which was troubled by the thermal snap. Stellar interferometer tracking experiment (SITE) was

another example of a space mission that must have been designed to be thermally quiet. The related analysis for this structure is presented in Ref. 87. Thornton et. al.⁸⁸ present an approach for investigation of the thermally induced vibrations of a split blanket solar array due to the self shadowing of the central truss. In another work⁸⁹ Foster et. al. perform an experimental investigation for the thermally induced vibrations of a fixed-free beam with a tip mass. The authors report a new phenomenon called “thermal strum” by which they mean that for the case of the unstable excitations related to the first mode, there is a presence of the second mode in the response also. The effects of thermally induced structural disturbances of a general flexible appendage on the attitude dynamics of a spacecraft are investigated in Ref. 90. In another research effort, the thermal performance of a solar panel is investigated experimentally which provides a detailed explanation of solar panel thermal snap disturbances.⁶⁵ Thermal distortion analysis of a three meter inflatable reflect array antenna is analyzed by Fang⁹¹, where they use FEM to analyze bending induced vibrations of the inflatable booms. The effects of the thermal distortion of the booms to the surface deviation of the radio frequency membrane are also investigated. Lin et. al. performs some thermo-structural analysis of a general Earth orbiting flexible structure⁹². The authors develop a coupled analysis for the thermal and the structural solution using a finite element formulation for a rotationally fixed floating frame. They consider both the axial force and bending moments due to temperature changes. Low frequency microwave radiometer (LFMR) is another structure that was placed on the geostationary orbit for the purpose of monitoring precipitation and ocean surface temperatures, surface currents and wind patterns. This structure with an allowable rms deflection error of $8.11 \times 10^{-5} m$ is another example of a structure that had to be

designed properly for such disturbances.⁹³ Williams et. al.⁹⁴ suggest a thermal radiation model for a triangular truss (ISAT) with MLI blankets to size and estimate the structural mass of a triangular truss that meets a given set of structural requirements. In their analysis they solve the temperature field for the back and front longerons where they include the effects of the direct solar radiation, Albedo, and Earth. However, the effect of the thermal conduction is ignored in their estimation of the temperature variations.

Most of the work done in the stated literature pertains to the bending thermally induced disturbances in the space structures. Very few of the aforementioned research projects and experiments addressed the thermally induced twist of space structures. HST and Apollo were examples of this which experienced the torsion of their long cylindrical booms. Due to the very large length of the ISAT, its relatively low torsional rigidity, and the special pattern of the diagonal members the structure is susceptible to the torsional excitations of low frequency. Therefore, we are motivated to understand this phenomenon. The main purpose of this study is to solve the thermal conduction in the 3 dimensional truss element. Also in some of the work in the previous literature, it is stated that the continuum models can not be accurate for the thermal analysis of the space structures because of their incapability of including the temperature variations along the members.^{57, 70} In the present analysis, the continuum model for the lattice type structure is used in conjunction with the solution of the thermal problem to solve for the structural response.

5.2 Problem Overview

The analysis of the thermal response for space structures requires a structural model and a thermal model. In the thermal model, the orbital heat fluxes are calculated.

These models can be solved in a coupled or decoupled form with the structural model to solve for the dynamic response. In the coupled analysis, it is assumed that the structural deflections affect the geometrical boundary conditions for the thermal problem and therefore, the thermal-structural analysis are performed at the same time. This method can be both complicated and time consuming. In the decoupled analysis, on the other hand, the thermal and structural solutions are found separately. The solution to the thermal problem provides us with the temperature gradients as a known function of time. The calculated thermal torques and moments from this step is then fed to the structural model to find the resulting deformations and dynamic responses. This approach assumes that the structural deformations are small enough to allow conduction and radiation to be unaltered by the structural deformations.⁷⁰ According to Thornton^{57, 70}, for overall isothermal structural behavior continuum models give good results. According to these authors, in realistic lattice type space structures where the temperatures vary significantly from member to member, consideration of this type of local temperature distribution is beyond the capability of the continuum models. In this study we show that the assumption for isothermal structural members is not really necessary. The limitation of the continuum model is only when the material properties are a function of time, or, when the deformations are so large that the effect of such deformations should be included in the thermal problem. In such cases, a coupled thermal-structural analysis is necessary which is beyond the capability of the continuum model approach presented here. Because the structure in this analysis is long and skinny (300 m \times 3 m), the deformations of the members at the cross section are assumed to be relatively small compared to the deformations of the overall length of the structure. So we assume that the local

deformations are small enough that they do not change the boundary conditions for the thermal problem (solved at the cross section). Therefore, in this chapter we use the decoupled approach with the continuum model to analyze the thermally induced torsional vibrations for this structure. For the thermal problem, on the other hand, the variations of the temperature from member to member as well as the variations of the temperature along each member are included. So the assumptions for the thermal model are not based on isothermal structural members.

5.3 Heat Conduction

In this section the heat conduction problem in the 3-D element is solved to find the temperature distribution in the structure. Some of the assumptions made in this analysis are as follow:

- 1) The satellite is in a circular orbit,
- 2) The longitudinal axis of the satellite is aligned with the orbit tangent,
- 3) The orbit plane for the structure is the same as the Earth's orbit around the sun, therefore, the satellite passes through the shadow line in every cycle. Dependent upon which orbit the satellite is located in it might not pass experience the eclipse,
- 4) Changes in the direct solar heating are dominant when the satellite passes the shadow line and therefore the Albedo and the Earth infrared are neglected in this analysis,
- 5) The thermal bending of the bar members are ignored here and it is assumed that the bar members can expand and compress only,
- 6) The radiation from the satellite to the space is neglected in the presented study.
- 7) The temperature variation is so fast the does not allow immediate expansion for the members,

8) The radar panel blocks the top members so that they don't see the sun, and warm up through the conduction

finally,

9) The temperature is invariant along the axial direction and it changes only within through the thickness. (Through thickness temperature ΔT is shown in Figure 5-3.)

The temperature distribution from this analysis is used to find the resultant thermal torque in the structure. The structural time response is then found using these results. Figure 5-3 depicts a schematic view of the heat transfer along the members of this truss. As it is shown in Figure 5-4 when the satellite passes through the shadow line the bottom part (the panel side) which faces the sun experiences an enormous heat flux. We assume that the panel blocks the diagonal and the batten members and therefore the only parts that absorb the heat are the bottom of longerons as shown in Figure 5-5.

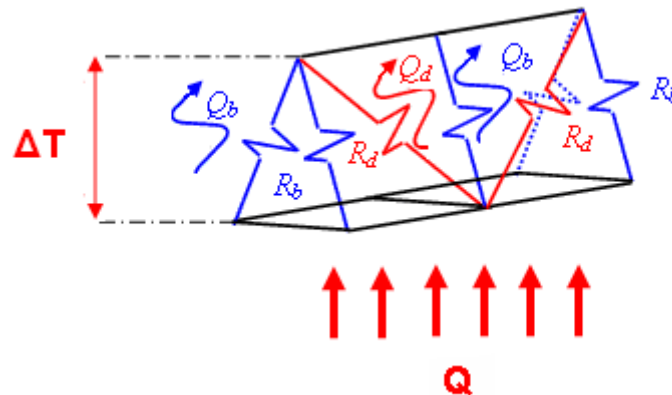


Figure 5-3 A view of the heat conduction in the truss element

Figure 5-4 shows the orientation of the satellite with respect to the Sun and the Earth when it passes the eclipse line. Following Unsold,⁹⁵ the relation for the solar heat flux can be found as,

$$q_s(r) = S \frac{r_E^2}{r^2} \quad (5.1)$$

where S is the input radiant energy from the sun at the distance of 1 AU (the distance between the Earth and the Sun which is 150×10^6 Km), and $S(r)$ is the solar heat flux at a distance r from the Sun in the solar system. The value of S is given by,

$$S = 1.37 \left(\frac{KW}{m^2} \right) \quad (5.2)$$

Using this figure we can write,

$$r^2 = r_E^2 + p^2 + 2r_E p \quad (5.3)$$

where p is the radius of the satellite orbit around the Earth and can be found as,

$$p = 18.371 \times 10^6 (m) \quad (5.4)$$

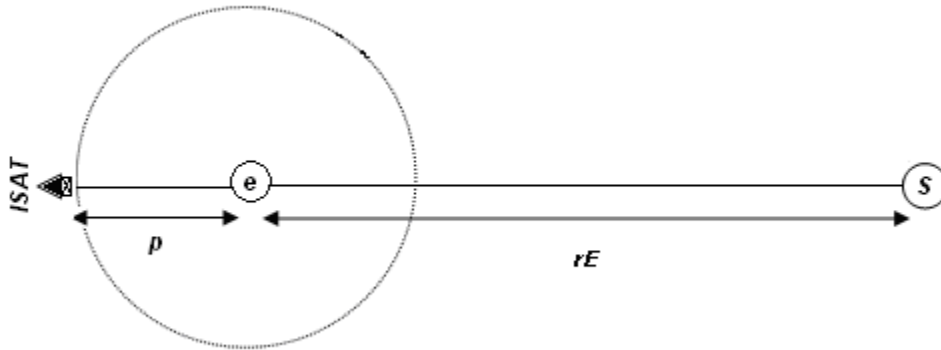


Figure 5-4 A view of the Earth and the ISAT orbit

Using the relations (5.1-4) we find,

$$q_s(r) \approx 1.37 \left(\frac{KW}{m^2} \right) \quad (5.5)$$

Presented here is the calculation for the time that it takes for the structure to fully exit the shadow. Knowing that the orbital altitude for this truss is 12000 (Km) we have the following:

$$p = 12'000(Km) + r_e = 12000 + 6.371 \times 10^3 = 18.371 \times 10^3 (Km) \quad (5.6)$$

where r_e is the radius of the Earth and p is the orbital radius. The orbital velocity can then be found as,

$$V = \sqrt{\frac{Gm_e}{p}} \rightarrow t = \frac{d}{V} = d \sqrt{\frac{p}{Gm_e}} \quad (5.7)$$

where,

$$G = 6.6743 \times 10^{-11} \left(\frac{Nm^2}{Kg^2} \right) \quad (5.8)$$

$$m_e = 5.9736 \times 10^{24} Kg \quad (5.9)$$

and m_e is the mass of the Earth. Assuming that the structure is aligned with the orbit tangent and passes the shadow line along its length, the time that it takes for the satellite to pass through this line can be found as,

$$t = \frac{d}{V} = d \sqrt{\frac{p}{Gm_e}} = 300 \sqrt{\frac{18.371 \times 10^6}{6.6743 \times 10^{-11} \times 5.9736 \times 10^{24}}} = 0.0644(\text{sec.}) \quad (5.10)$$

As it can be seen this time is very small. Therefore, we assume that the entire satellite is exposed to the sun instantaneously, also we assume that the conduction happens a lot faster upon the incident of the solar heat flux than the radiation from the satellite to the space. Therefore, to also account for a worst case analysis, the radiation from the structure is ignored in this entire analysis and the top part is assumed to be insulated.

Figure 5-5 shows the areas that are exposed to the sun flux.

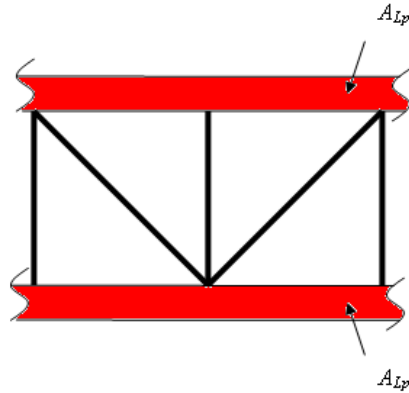


Figure 5-5 A Schematic of the bottom side of the truss repeating element

For the heat absorbed by the repeating element we get,

$$Q = 2q_s \cdot A_{Lp} \cdot \alpha_s \quad (5.11)$$

where α_s is the absorptivity of the longeron members, q_s is the solar flux and A_{Lp} is the area shown in Figure 5-5. Figures 5-6 and 5-7 show the view of the two sides of the truss element.

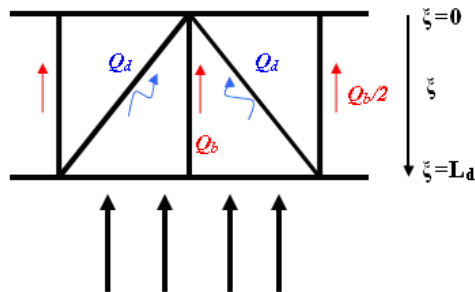


Figure 5-6 Heat transfer in the front side of the repeating element

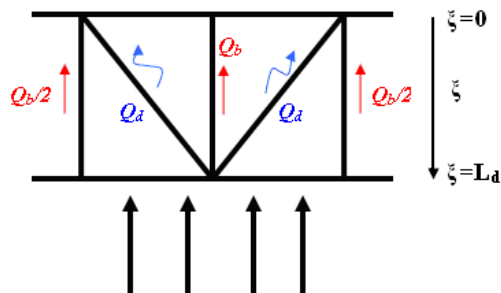


Figure 5-7 Heat transfer in the back side of the repeating element

The heat absorbed by an element is partly consumed by the members at the bottom (the 4 longerons, the 2 diagonal and 2 battens shown in Fig. 5-5). Therefore, the transferred heat through the longerons and diagonals on the element sides in Figs. 5-6 and 5-7 can be found as,

$$Q_t = Q - (2m_b c_b + 2m_d c_d + 4m_L c_L) \frac{\partial T}{\partial t} \Big|_{\xi=L_d} \quad \text{at } \xi = L_d \quad (5.12)$$

The heat Q_t is then divided between the total of 4 battens and 4 diagonals on the sides, so we get,

$$Q_t = 4Q_b + 4Q_d \quad (5.13)$$

where Q_b and Q_d are the heat flux along the battens and the diagonals respectively. Knowing that the cross-sectional area of the battens and the diagonals are the same, we assume the following relation for the ratio of the heat that passes through these members,

$$Q_b = \frac{Q_d L_d}{L_b} \quad (5.14)$$

The simplified assumption in (5.14) in its general form is based on a steady state case. A more detailed transient analysis can be performed by solving the heat transfer along these members. From (5.13) and (5.14) we get,

$$Q_t = 4 \frac{Q_d L_d}{L_b} + 4Q_d \quad (5.15)$$

or,

$$Q_d = \frac{Q_t L_b}{4(L_d + L_b)} \quad (5.16)$$

Using (5.16) and (5.12) we have,

$$Q_d|_{\xi=L_d} = \frac{\left(Q - (2m_b c_b + 2m_d c_d + 4m_L c_L) \frac{\partial T}{\partial t} \Big|_{\xi=L_d} \right) L_b}{4(L_d + L_b)} \quad (5.17)$$

Finally the heat flux for the diagonals (heat per unit area) can be found as,

$$q_d = \frac{Q_d}{A_d} \quad (5.18)$$

For the boundary condition of the bottom (heated side) we get,

$$q_d|_{\xi=L_d} = K \frac{\partial T}{\partial \xi} \Big|_{\xi=L_d} = \frac{\left(Q - (2m_b c_b + 2m_d c_d + 4m_L c_L) \frac{\partial T}{\partial t} \right) L_b}{4(L_d + L_b) A_d} \quad (5.19)$$

or,

$$K \frac{\partial T}{\partial \xi} + \frac{(m_b c_b + m_d c_d + 2m_L c_L) L_b}{2(L_d + L_b) A_d} \frac{\partial T}{\partial t} = \frac{Q L_b}{4(L_d + L_b) A_d} \quad \xi = L_d \quad (5.20)$$

The boundary condition at the top ($\xi = 0$) can be found in a very similar manner. The heat from the 4 diagonals and battens on the two sides of the truss is consumed by the top 2 longeron members shown in Fig. 5-3. For an insulated boundary condition at the top we get,

$$4(Q_d + Q_b) = 2m_L c_L \frac{\partial T}{\partial t} \quad \text{at } \xi = 0 \quad (5.21)$$

Using (5.14) and (5.21) we get,

$$4Q_d \left(\frac{L_d}{L_b} + 1 \right) = 2m_L c_L \frac{\partial T}{\partial t} \quad (5.22)$$

or,

$$Q_d = \frac{m_L c_L L_b}{2(L_d + L_b)} \frac{\partial T}{\partial t} \quad (5.23)$$

Finally the boundary condition for the top can be found as,

$$q_d = \frac{Q_d}{A_d} = K \frac{\partial T}{\partial \xi} = \frac{m_L c_L L_b}{2(L_d + L_b) A_d} \frac{\partial T}{\partial t} \quad \text{at} \quad \xi = 0 \quad (5.24)$$

So the PDE and the boundary conditions for the heat transfer problem of the system can be written in the following form,

$$\begin{cases} \kappa \frac{\partial^2 T}{\partial \xi^2} = \frac{\partial T}{\partial t} & 0 < \xi < L_d & t > 0 \\ K \frac{\partial T}{\partial \xi} - \eta_1 \frac{\partial T}{\partial t} = 0 & \xi = 0 & t > 0 \\ K \frac{\partial T}{\partial \xi} + \eta_2 \frac{\partial T}{\partial t} = q & \xi = L_d & t > 0 \end{cases} \quad (5.25)$$

where,

$$\begin{aligned} q &= \frac{QL_b}{4(L_d + L_b) A_d} \\ \eta_1 &= \frac{m_L c_L L_b}{2(L_d + L_b) A_d} \\ \eta_2 &= \frac{(m_b c_b + m_d c_d + 2m_L c_L) L_b}{2(L_d + L_b) A_d} \end{aligned} \quad (5.26)$$

Figure 5-8 shows a schematic of the resultant one-dimensional heat transfer problem for this structure. As shown in this figure the longeron members are modeled as thermal masses at the ends of a diagonal member. Since the top longeron member is connected to diagonals on both sides, there fore half of its thermal capacity is included here as shown in this figure.

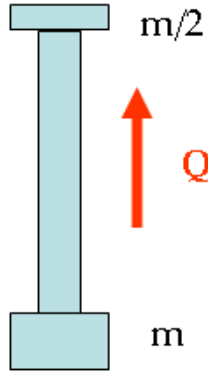


Figure 5-8 The heat transfer schematic along a diagonal member

The partial differential equation shown in (5.25) is a homogenous equation with non-homogenous boundary conditions. Using separation of variables, the solution for the non-dimensionalized temperature can be found as follows:

$$\begin{aligned} \tilde{T} = & \frac{K}{L_d q} \left(\sum_{n=1}^{\infty} B_n \left(\frac{-\eta_1 \lambda_n \kappa}{K} \sin(\lambda_n \xi) + \cos(\lambda_n \xi) \right) e^{-\lambda_n^2 \kappa t} + \frac{q \kappa}{KL_d + \kappa(\eta_1 + \eta_2)} t \right. \\ & \left. + \frac{q}{2(KL_d + \kappa(\eta_1 + \eta_2))} \xi^2 + \frac{\eta_1 q \kappa}{K(KL_d + \kappa(\eta_1 + \eta_2))} \xi - \frac{q}{6(KL_d + \kappa(\eta_1 + \eta_2))} L_d^2 \right) \end{aligned} \quad (5.27)$$

where λ_n 's are the roots of the characteristics equation,

$$\tan(\lambda_n L_d) = \frac{K \kappa \lambda_n (\eta_1 + \eta_2)}{-K^2 + \eta_1 \eta_2 \kappa^2 \lambda_n^2} \quad (5.28)$$

The initial temperature T_0 which is assumed to be invariant along the axial direction is then used to find the B_n values.

5.4 Structural Response

Figure 5-9 shows a cross section of this structure. As it can be seen in this figure the thermal expansion of the diagonal members causes thermal reactions f_d which result in a torque for this structure. For the batten members, however, the thermal reactions f_b

balance each other. Therefore the diagonal members are the only source for the thermal twist of this structure.

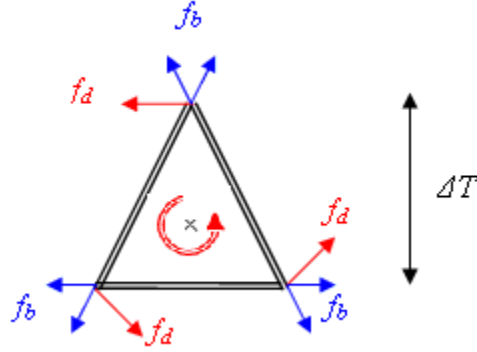


Figure 5-9 Thermal forces at the cross section

Having the temperature distribution of these members, the thermal reaction for the bottom diagonal members can be found using the following relation,

$$F_{d1} = A_d E_d \varepsilon_T = A_d E_d \alpha_d T \quad (5.29)$$

For the diagonal members on the sides that the temperature varies along their length, the thermal reaction can be found as,

$$F_{d2} = A_d E_d \varepsilon_T = A_d E_d \alpha_d \frac{\int_0^{L_d} T d\xi}{L_d} \quad (5.30)$$

The resultant thermal torque can then be calculated using the relations (5.29) and (5.30) as follows:

$$T_o = (F_{d1} + 2F_{d2}) \frac{L_b^2}{2L_d \sqrt{3}} \quad (5.31)$$

The resultant thermal torque can then be used to find the torsional vibration for the truss.

From Chapter 2, the torsional equation of motion for the truss can be found as,

$$GJ_{eq} \theta'' - \rho J_{eq} \ddot{\theta} = \frac{\partial T_o}{\partial x} \quad (5.32)$$

where coordinate x is measured along the length of the satellite. Because the temperature is assumed to be invariant in the axial direction and it changes through the thickness only, the thermal torque is constant along the length also, so we get:

$$\frac{\partial T_o}{\partial x} = 0 \rightarrow GJ_{eq.} \theta'' - \rho J_{eq.} \ddot{\theta} = 0 \quad (5.33)$$

The thermal torque at the cross section, on the other hand, is a function of time. Therefore, the problem that we are interested to solve is a free torsional vibration with a variable boundary condition in which the time varying thermal torque induces dynamics on the system. The general solution procedure for a 1-D continuum with variable boundary conditions can be found using Refs. 96 and 97. The boundary conditions for this problem are,

$$GJ_{eq.} \frac{\partial \theta}{\partial x}(0, t) = GJ_{eq.} \frac{\partial \theta}{\partial x}(L_{tot}, t) = T_o(t) \quad (5.34)$$

where T_o can be found using the thermal reactions as calculated in (5.31) and is a function of time only. The solution for the thermal twist θ can be decomposed in two parts, the quasi-static torsion in which the effect of the inertia is neglected and the dynamic response. Therefore, for the quasi-static solution we have,

$$GJ_{eq.} \frac{\partial^2 \theta_{st}}{\partial x^2} = 0 \rightarrow \theta_{st} = c_1 x \quad (5.35)$$

where the equivalent torsional stiffness as found in Chapter 2 is,

$$GJ_{eq.} = \frac{E_d A_d L_b^4 L_L}{4L_d^3} \quad (5.36)$$

Note that the quasi-static twist is the difference between the twist of a cross section at coordinate x and the torsion of the tip at $x=0$. Also, the following relation exists between the torque and the static twist:

$$GJ_{eq.} \frac{\partial \theta}{\partial x} = T_o \rightarrow GJ_{eq.} c_1 = T_o \rightarrow c_1 = \frac{T_o}{GJ_{eq.}} \quad (5.37)$$

From (5.35) and (5.37) we get,

$$\theta_{st.} = \frac{T_o}{GJ_{eq.}} x \quad (5.38)$$

The quasi-static response can be expanded in terms of the modes shapes for this structure using its Fourier coefficients,

$$\theta_{st} = \frac{T_o}{GJ_{eq.}} x = \sum_{n=1}^{\infty} a_n \Theta_n \frac{T_o}{GJ_{eq.}} \quad (5.39)$$

where,

$$a_n = \frac{-4L_{tot}}{n^2 \pi^2}, \quad n = 1, 3, 5, \dots \quad (5.40)$$

It is obvious that equation (5.39) automatically satisfies the boundary conditions in (5.34). For the initial conditions we have,

$$\frac{\partial \theta}{\partial t}(x, 0) = \theta(x, 0) = 0 \quad (5.41)$$

Because the solution is decomposed into the dynamic plus the quasi-static terms we get,

$$\theta_{dyn.} = \theta - \theta_{st.} \quad (5.42)$$

For the initial condition of the static response we have,

$$\theta_{st}(0) = \frac{T_o(0)}{GJ_{eq.}} x = 0 \quad (5.43)$$

Using (5.42) and (5.43) we get,

$$\theta_{dyn.}(0) = \underbrace{\theta(0)}_0 - \underbrace{\theta_{st.}(0)}_0 = 0 \quad (5.44)$$

For the initial velocity condition we have,

$$\dot{\theta}_{dyn.}(0) = \underbrace{\dot{\theta}(0)}_0 - \dot{\theta}_{st.}(0) = -\dot{\theta}_{st.}(0) \neq 0 \quad (5.45)$$

These initial conditions are later used to find the dynamic response solution for this system. The total response can be written as a summation of the quasi-static term and the dynamic term as follow,

$$\theta = \theta_{st} + \sum_{n=1}^{\infty} \Theta_n q_n \quad (5.46)$$

where Θ_n 's are the mode shapes and q_n 's are the temporal solutions. Using (5.39) and (5.46) we can write,

$$\theta = \sum_{n=1}^{\infty} \Theta_n \left(a_n \frac{T_o}{GJ_{eq.}} + q_n \right) \quad (5.47)$$

Making the substitution for (5.47) in (5.33) we get,

$$GJ_{eq.} \sum_{n=1}^{\infty} \Theta_n'' \left(a_n \frac{T_o}{GJ_{eq.}} + q_n \right) - \rho J_{eq.} \sum_{n=1}^{\infty} \Theta_n \left(a_n \frac{\ddot{T}_o}{GJ_{eq.}} + \ddot{q}_n \right) = 0 \quad (5.48)$$

Also from relation for the quasi-static response in (5.35) we get,

$$\sum_{n=1}^{\infty} a_n \Theta_n'' \frac{T_o}{GJ_{eq.}} = 0 \quad (5.49)$$

Using the relations in (5.48) and (5.49) we get,

$$GJ_{eq.} \Theta_n'' q_n - \rho J_{eq.} \Theta_n \left(a_n \frac{\ddot{T}_o}{GJ_{eq.}} + \ddot{q}_n \right) = 0 \quad (5.50)$$

This relation can be written in the following form: (a separation of variables)

$$\frac{\Theta_n''}{\Theta_n} = \frac{\rho J_{eq.} \left(a_n \frac{\ddot{T}_o}{GJ_{eq.}} + \ddot{q}_n \right)}{GJ_{eq.} q_n} = -c_n^2 \quad (5.51)$$

where the mode shapes can be found as,

$$\Theta_n = \cos\left(\frac{n\pi x}{L_{tot}}\right) \quad n = 1, 2, \dots \quad c_n = \frac{n\pi}{L_{tot}} \quad (5.52)$$

From (5.51) and (5.52) we get,

$$\ddot{q}_n + \frac{GJ_{eq.} n^2 \pi^2}{\rho J_{eq.} L_{tot}^2} q_n = -a_n \frac{\ddot{T}_o}{GJ_{eq.}} \quad (5.53)$$

Finally, using the modes shapes in (5.52) and the solution for the temporal solution in (5.53), and the initial conditions the dynamic response of the system can be as,

$$\begin{aligned} \theta_{dyn} = \theta - \theta_{st} = & \sum_{n=1,3,5,\dots}^{\infty} \cos\left(\frac{n\pi x}{l}\right) \times \left[a \sin\left(c_n \sqrt{\frac{GJ_{eq.}}{\rho J_{eq.}}} t\right) + b \cos\left(c_n \sqrt{\frac{GJ_{eq.}}{\rho J_{eq.}}} t\right) \right. \\ & \left. + \sum_{j=1}^{\infty} a_j \sin\left(c_n \sqrt{\frac{GJ_{eq.}}{\rho J_{eq.}}} t\right) + b_j \cos\left(c_n \sqrt{\frac{GJ_{eq.}}{\rho J_{eq.}}} t\right) + \gamma(t) \left(\frac{\rho J_{eq.}}{\alpha^2 \rho J_{eq.} + c_n^2 GJ_{eq.}} \right) \right] \end{aligned} \quad (5.54)$$

where,

$$\gamma(t) = \frac{2A_d B_j e^{-t\kappa\lambda_j^2} E_d L_b^2 L_{tot} \alpha_d \kappa^2 \lambda_j^3 \left(-\frac{2\eta_1 \lambda_j \kappa}{K} + \left(\frac{2\eta_1 \lambda_j \kappa}{K} + L_d \lambda_j \right) \cos(L_d \lambda_j) + \left(2 + \frac{-\eta_1 \lambda_j \kappa}{K} L_d \lambda_j \right) \sin(L_d \lambda_j) \right)}{\sqrt{3} GJ_{eq.} L_d^2 n^2 \pi^2}$$

$$a = \frac{2\sqrt{3} A_d E_d L_b^2 L_{tot} \alpha_d}{GJ L_d n^3 \pi^3 \sqrt{\frac{GJ}{\rho J}}} \frac{q \kappa}{KL_d + \kappa(\eta_1 + \eta_2)}$$

$$b = 0$$

$$\begin{aligned}
a_j = & - \frac{2A_d E_d B_j \frac{G}{\rho} L_b^2 L_{tot} \alpha_d \kappa \lambda_j \left(-\frac{2\eta_1 \lambda_j \kappa}{K} + \left(\frac{2\eta_1 \lambda_j \kappa}{K} + L_d \lambda_j \right) \text{cod}(L_d \lambda_j) + \left(2 - \frac{\eta_1 \lambda_j \kappa}{K} L_d \lambda_j \right) \sin(L_d \lambda_j) \right)}{\sqrt{3} G J L_d^2 n \pi \left(\frac{G}{\rho} n^2 \pi^2 + L_{tot}^2 \kappa^2 \lambda_j^4 \right) \sqrt{\frac{G}{\rho}}} \\
b_j = & - \frac{2A_d E_d B_j L_b^2 L_{tot} \alpha_d \kappa^2 \lambda_j^3 \left(-\frac{2\eta_1 \lambda_j \kappa}{K} + \left(\frac{2\eta_1 \lambda_j \kappa}{K} + L_d \lambda_j \right) \text{cod}(L_d \lambda_j) + \left(2 - \frac{\eta_1 \lambda_j \kappa}{K} L_d \lambda_j \right) \sin(L_d \lambda_j) \right)}{\sqrt{3} G J L_d^2 n^2 \pi^2 \left(\frac{G}{\rho L_{tot}^2} n^2 \pi^2 + \kappa^2 \lambda_j^4 \right)}
\end{aligned} \tag{5.55}$$

The relation in (5.54) presents the torsional vibration for this structure. Both the free vibration and the forced exponential function (thermal torque) are included in this relation.

5.5 Numerical Results

In this section the numerical results for the thermal torque, and the thermal quasi-static and vibration twist are presented. The following values are used for the thermal properties of the members in this analysis,

$$\begin{aligned}
\alpha_d &= 2 \text{ ppm}/^\circ C \\
\kappa &= 1.9841 \times 10^{-8} \text{ (m}^2/\text{sec.)} \\
K &= 0.04 \text{ (W/m/}^\circ K) \\
c &= 1400 \text{ (J/Kg/}^\circ K) \\
\alpha_s &= 0.1
\end{aligned} \tag{5.56}$$

where, α_d is the coefficient of the thermal expansion, κ is the thermal diffusivity, α_s is the thermal absorptivity and c is the thermal capacity for the members. We introduce a non-dimensional thermal time response parameter similar to Boley⁹⁶ as,

$$\tilde{t} = \frac{\kappa}{L_d^2} t \tag{5.57}$$

Figures 5-10 to 5-14 show the results for the temperature variation at the ends of the diagonal members, thermal torque, quasi-static torsion, dynamic torsion and the lateral vibration respectively. This structure experiences an approximate temperature change of 30 °C in an hour upon passing the shadow line. It should be noted that because the radiation is ignored in this analysis, the resultant torque, and quasi-static are overestimated. As it can be seen in the Figures 5-10 and 5-11, both the temperature and the thermal torque are increasing with time. This, off course, will not be the case in the real structure, because of the radiation of the truss to the space. Technically the structure can not get warmer than the surrounding space (sun side). Therefore, this temperature profile approximates the real structure initially and as time grows the temperature results for this analysis represent a very conservative case. On the other hand, for the case of the thermally induced vibrations that are of our main interest, the assumption regarding no radiation gives more realistic results compared to the quasi-static solution. The reason is that such oscillations are the results of an enormous heat flux in a very short period of time (in the order of seconds) during which the radiation can be considered small compared to the heat input. So this thermal shock provides an initial condition (similar to an impact) to the system and results in the vibrations which are no longer dependent on the heat transfer in the system after they start. These non-increasing oscillations in the system will continue until they eventually damp out as a result of the damping present in the system. Finally, the lateral vibrations as a result of the torsion are about are 2 cm at the tip of the truss system. Recommendations for reducing the thermal response of the system are presented in the following conclusion section.

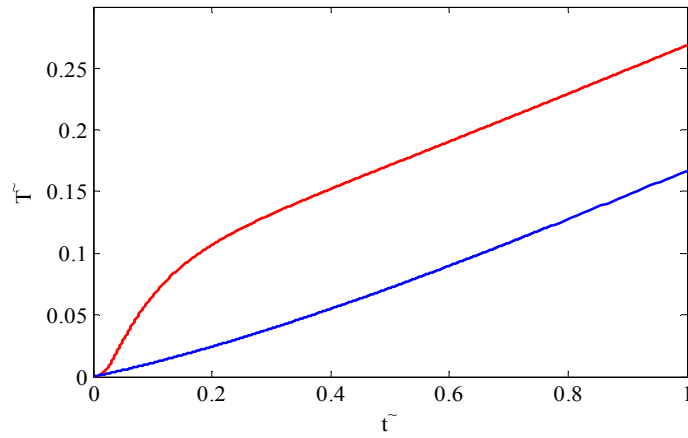


Figure 5-10 Non-dimensionalized temperature profile at the ends of a diagonal member

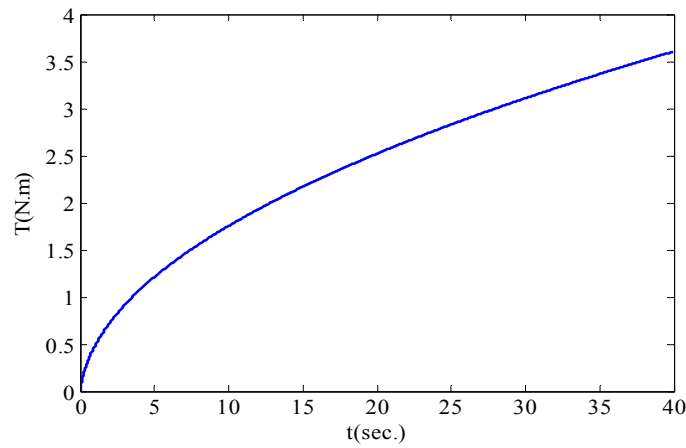


Figure 5-11 Variation of the thermal torque with respect to the temperature

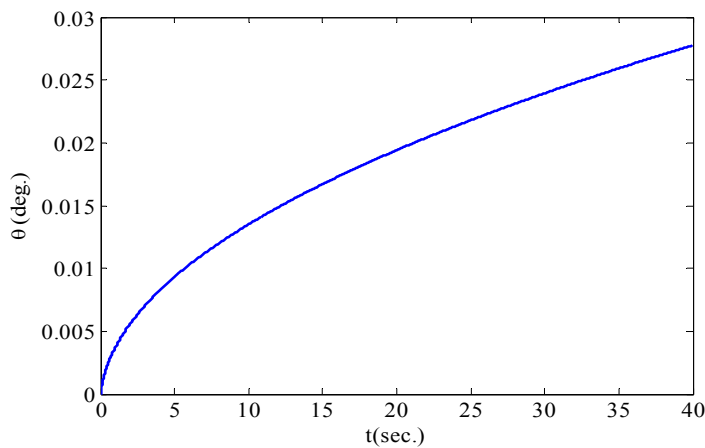


Figure 5-12 The quasi-static torsion at the tip

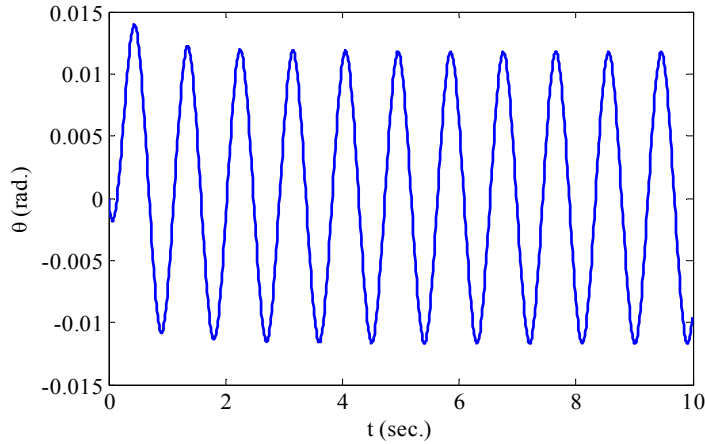


Figure 5-13 The dynamic twist at the tip

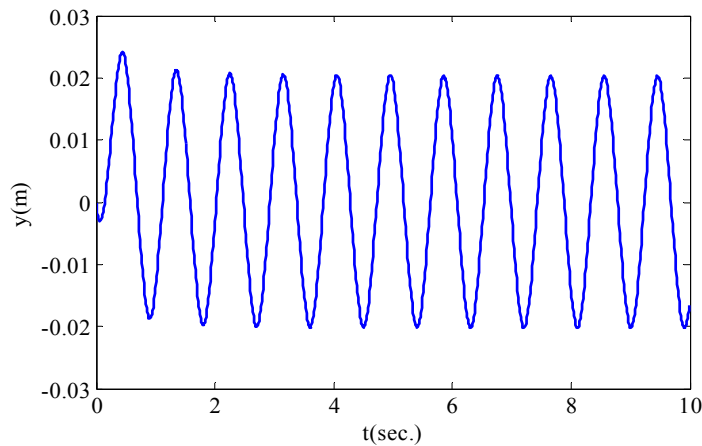


Figure 5-14 The lateral oscillations as a result of the torsion at the tip

Figures 5-15 to 5-18 show the results of the amplitude of thermal vibrations at the tip of the truss for different values of thermal conductivity, diffusivity and the thermal capacity. As is shown in these figures, the thermal response increases with diffusivity and decreases with the thermal conductivity. Examining equation (5.25), it is clear that the thermal diffusivity enhances the temperature gradients in the system. As a result, the thermal torque gets larger which results in larger oscillations in the system. The larger thermal conductivity values, on the other hand, result in quicker heat transfer through the members which reduces the temperature changes across the thickness. Therefore, the

resultant torque is smaller which reduces the thermal vibrations. Finally, since the longerons act like heat sink for the system, the larger their thermal capacity the slower the temperature changes in the truss and therefore, the smaller the thermal response. Therefore, as shown in Figure 5-18, an increase in the thermal capacity diminishes the structure's oscillations.

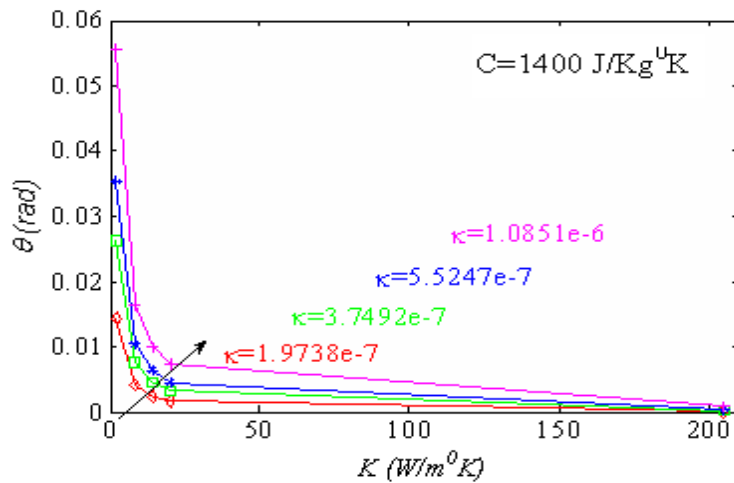


Figure 5-15 Dynamic twist with respect to the variation of the thermal conductivity

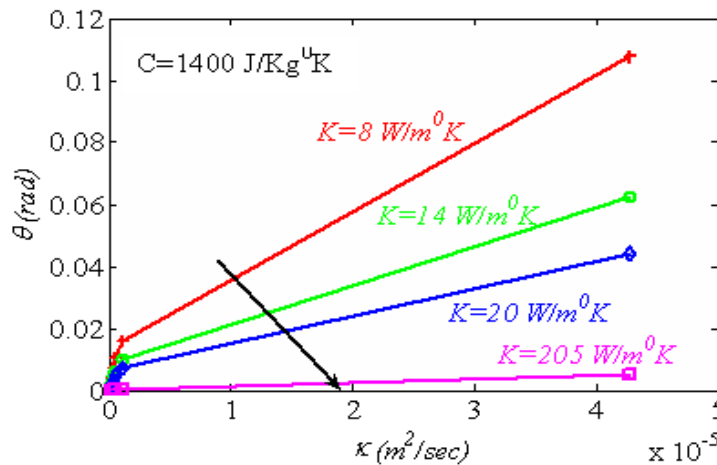


Figure 5-16 Dynamic twist with respect to the variation of the thermal diffusivity

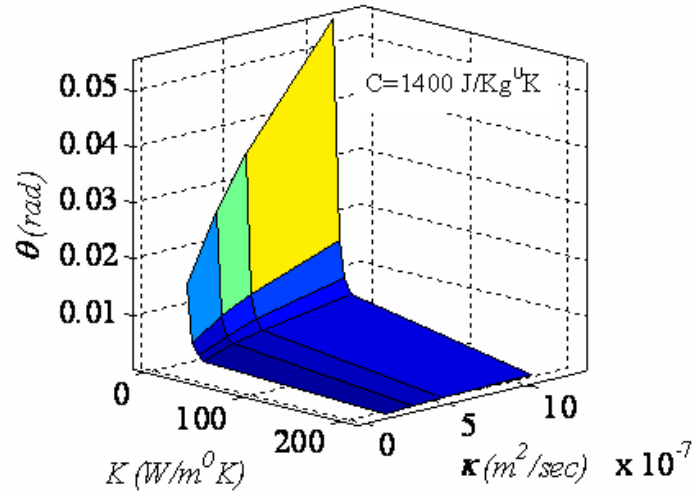


Figure 5-17 Variation of the dynamic thermal twist with both diffusivity and conductivity

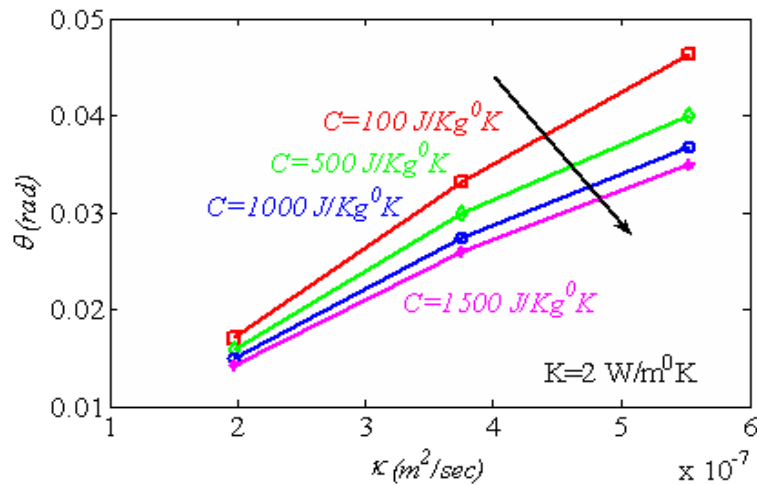


Figure 5-18 Dynamic twist with respect to the variation of the thermal capacity

5.6 Concluding Remarks

In this chapter the thermally induced torsional vibrations of a 3-dimensional truss structure with a repeated pattern are analyzed. A decoupled thermal structural analysis is used with the equivalent 1-D model for the structure to find the structural response. It is shown that when the satellite passes through the eclipse line, the instantaneous change in the solar heat flux induces temperature gradients in the system. The resultant thermal

torque causes a considerable vibration in the system. The heat radiation from the satellite to the space is ignored in this analysis which results in a worst case scenario of the thermal response. Finally, it is shown that the assumption of the so called isothermal members is not necessary to calculate the thermally induced vibrations in a homogenized model.

There are many ways to mitigate the thermally induced vibrations in a space structure. For example, using materials such as Kevlar fibers or other material with negative axial thermal coefficients of expansion with other materials.⁹⁸ A suitably layered construction of such materials can produce a lamina with a net zero CTE which is less sensitive to the thermal disturbances (a design to mitigate the temperature deformations). One of the other most common ways to mitigate the thermally induced responses in a spacecraft is the use of control materials such as Multi-Layer Insulation (MLI) thermal blankets (a design to mitigate the temperature gradients). Typical space MLI blankets have emittance values between 0.007 and 0.05 (The lower the emittance, the better thermal isolation).⁵⁶ In many applications using multiple layers of MLI to achieve a low effective emittance can be impractical due to the mass limitations for space structures. Other ways of correcting the pointing accuracy of a spacecraft as a result of thermal disturbances are using momentum wheels, magnetic coils, thrusters or gyros (a design to control and reduce the resultant motions). Finally, increasing the torsional rigidity of the structure, or choosing a symmetric pattern for the diagonal members for the case of this particular structure are other ways to avoid producing a thermal disturbances (See Figure 5-19).⁹⁴ For the case of symmetric configuration shown in the figure, the torque will be minimized and so will the resulting disturbances.

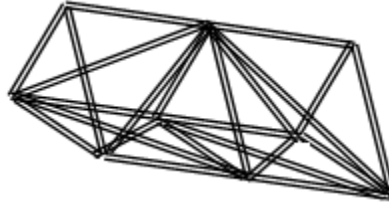


Figure 5-19 An alternative element configuration (less susceptible to thermal vibrations)

As mentioned earlier the thermal capacity and thermal conductivity help reducing the thermal oscillations as a result of the instantaneous temperature gradients in space. Therefore, using a material that is highly conductive or joints with high thermal capacity for this structure is desirable. Another way to reduce the thermal vibrations is to use joints such as sliding joints that allow expansions of the members in order to diminish the thermal reactions and the thermal torque.

Chapter 6

Conclusion, Recommendations and Future

Work

6.1 Conclusions

This research effort was concerned with developing a continuum model for a deployable space truss. Since, the connections in deployable structures are not as simple as a hinged or a rigid joint, a more complex type of joint was assumed in this analysis. In addition, an experimental effort for the purpose of validation of a continuum model with hinge connections revealed the need for an alternative modeling. Therefore, a micropolar continuum modeling technique is developed for the ISAT-like structure in this study. The results from the micropolar continuum theory are shown to be in much better agreement with the experiment compared to the methods presented in the previous research particularly for the higher modes. To develop this model, we assume that the mass moment of inertia is negligible for the individual components. Therefore, the condition of the nodal torque balance for the structure should hold. This assumption induces a

constraint on the strain field for the elements of the structure. This results in a coupling between the micro-rotations and the independent strain states that are the same as those of the continuum model. So the effects of the torsional flexibility of the joints and the micro-rotations of the members are retained while a one-dimensional model is found for the system.

Additionally, a finite element model was developed in MATLAB to validate the accuracy of the continuum model. The results are shown to be in good agreement (2% error for the frequencies) with those of the FEM. As a result of this model reduction the CPU usage is 180 times less than the FEM. In addition, the reduced order continuum model provides an analytical solution that allows simplicity and physical insight into the structural mechanics and the dominant physics of the structure. It also provides a simple tool for comparing dynamic characteristics of lattices with different properties.

It is shown that the error of the frequency estimations for this model gets larger for the smaller wavelengths (higher frequencies). This is because the error is related ratio of the wavelength to the element size. As the frequency of interest increases, the wavelength decreases, which diminishes the numbers of truss elements in the wavelength and results in a higher error. Also, one of the limitations of the continuum modeling is that the fundamental repeating element is a base of the analysis. Therefore, as opposed to the FEM methods where the mesh size can be refined to obtain better accuracy for the frequencies of interest, in continuum modeling the fundamental repeating element is known for a specific geometry and its size can not be dictated by the analyst. This results in lower accuracy for very high frequencies. So the continuum modeling technique is most efficient for the structures which contain a large number of repeating elements.

Therefore, the global dynamics play a more important role on the overall dynamics of the structure compared to the high frequency local modes.

In the final section of this dissertation, a thermal analysis is used with our continuum model to find the structural vibrations response. When the satellite passes through the eclipse line, the instantaneous change in the solar heat flux induces temperature gradients on the system. The temperature difference rises up to 20 °C between the hot and the cold sides of the satellite. Due to the extreme length of this structure, the resultant thermal torque from the temperature gradients induces a large amount of twist on the truss. The results presented here pertain to a more conservative analysis where the radiation is neglected during the transition time. Finally, it is shown that the assumption of the isothermal members is not necessary to calculate the thermally induced vibrations using a homogenized model.

The research reported herein has resulted in three journal articles^{3, 99, 100} and six conference papers.^{101, 103, 104, 105, 106, 107}

6.2 Future Work and Recommendations

As far as the future work for this model development goes, there are a few ways to improve the modeling technique presented in this research. In some of the suggested configurations for the space truss structures, the diagonal members are made of wires in tension and batten members in compression.⁴⁹ One possible approach would be to include the effects of the pre-tension and compression of these members and to account for their stiffness'.

Another improvement for this model would be to include the inherent damping in the structure. Dependent upon what are the main sources of damping in the system

(friction in the joints or viscoelasticity of the members), there are different ways to include them in the homogenized model. For example, for the case of the viscoelastic materials, the same assumptions for the displacement field can be made to express the damping of the individual members in terms of the strain values of the full order system. Similar assumptions regarding the local forces associated with the dependent strain components and their gradients can be employed. The difference is that the damping also contributes to these local forces and they need to be considered. As a result, these relations will introduce a coupling between the dependent strain values and the independent strain states. Therefore, they can be expressed in terms of the strain states similar to those of a continuum model. For the coulomb friction type damping existing in the joints, the model development would be more complicated because of the nonlinear nature in this type of damping.

Another important aspect of this satellite which opens up some possibilities for a future research is the experimental validation of the reduced-order model-based controller. Such technique has been validated numerically, using a LQR controller for lattice structures.^{4, 101, 102} An attempt for the purpose of the experimental validation of a controller based on this model was also made using Macro Fiber Composites (MFC) actuators. However, the voltage required for controlling the planar truss in this study was much higher than the capacity of the MFC. Therefore, using another type of actuator such as active members for this structure is recommended.

The other issue pertaining to this satellite is the dynamic stability. As mentioned previously in Chapter 5, the thermal twist for this satellite can be avoided for a different diagonal configuration. However, the thermal bending in this system will still remain to

be a problem. In particular, because of an unstable dynamic configuration due to its non-pointing position, the gravity gradients will play an important role for this structure. As opposed to the pointing satellites where the gravity forces can help with their stabilization, such forces can cause instability for this structure. As a result, the oscillations in the system become larger and larger so that eventually the satellite will be oriented away from its desired position. Therefore, this will open up another issue to include the gravity gradient effects on the dynamics of the system. Finally, some other interesting modeling aspects would be to develop a more complicated model to account for the changes in the kinetic energy of the members as a result of the flexibility of the joints. Also, due to the extreme length of this structure the nonlinear dynamics (geometric effects) for the homogenization approach should also to be investigated.

Bibliography

¹ Chmielewski, A.B., (2001), "Overview of Gossamer Structures," *Gossamer Spacecraft: Membrane and Inflatable Structures Technology for Space Applications*, edited by C.H.M. Jenkins, Vol. 191, Progress in Astronautics and Aeronautics, AIAA, Reston, Virginia, p. 2-3

² Sun, C.T., and Liebbe S.W., (1990), "Global-Local Approach to Solving Vibration of Large Truss Structures," *AIAA Journal*, Vol. 28, No. 2, 1990, p. 303-308

³ Salehian, A., Cliff, E.M., and Inman, D.J., (2006), "Continuum Modeling of an Innovative Space Based Radar Antenna Truss," *American Society of Civil Engineers Journal of Aerospace, Festschrift issue*, Vol. 19, No. 4, 2006, p. 227-240

⁴ Bennett, W.H., and Kwatny, H.G., (1989) "Continuum Modeling of Flexible Structures with Application to Vibration Control," *AIAA Journal*, Vol. 27, No. 9, p. 1264-1273

⁵ Yang, B., and Tan, C.A., (1992), "Transfer Functions of One-Dimensional Distributed Parameter Systems," *ASME Journal of Applied Mechanics*, Vol. 59, No. 4, p. 1009-1014

⁶ Noor, A.K., Mikulas, M.M., (1988), "Continuum Modeling of Large Lattice Structures: Status and Projections," *Large Space Structures: Dynamics and Control*, edited by Atluri, S.N., Amos, A.K., Springer-Verlag, NY

⁷ Noor, A.K., (1988), "Continuum Modeling for Repetitive Lattice Structures," *Appl. Mech. Rev.*, Vol. 41, No. 7, p. 285-296

⁸ Dean, D.L., and Avent, R.R., (1975), "State of the Art of Discrete Field Analysis of Space Structures," *Proceedings of the Second International Conference on Space Structures*, University of Guildford, England, p. 7-16

⁹ Renton J.D., (1970), "General Properties of Space Grids," *International Journal of Mechanical Sciences*, Vol. 12, p. 801-810

¹⁰ Tollenaere, H., and Caillerie, D. (1998), "Continuous Modeling of Lattice Structures by Homogenization," *Advances in Engineering Software*, Vol. 29, No. 7-9, p. 699-705

¹¹ Renton, J.D., (1967), "The Related Behavior of Plane Grids, Space Grids and Plates," *Proceedings of the Space Structures Conference*, Blackwell, Oxford, p. 19-32

¹² Wah, T., (1963), "Natural Frequencies of Uniform Grillages," *Journal of Applied Mechanics*, Vol. 30, p. 571-578.

- ¹³ Renton J.D., (1984), "The Beamlike Behavior of Space Trusses," *AIAA Journal*, Vol. 22, No. 2, p. 273-280
- ¹⁴ Burgardt, B., and Cartraud, P., (1999), "Continuum Modeling of Beamlike Lattice Trusses Using Averaging Methods," *Computers & Structures*, Vol. 73, p. 267-279
- ¹⁵ Noor, A.K., (1978), "Thermal Stress Analysis of Double-Layered Grids," *Journal of the Structural Division, ASCE*, Vol. 104, No. ST2, p. 251-262
- ¹⁶ Noor, A.K., and Andersen, C.M., (1979), "Analysis of Beam-like Lattice Trusses," *Computer Methods in Applied Mechanics and Engineering*, Vol. 20, p. 53-70
- ¹⁷ Noor, A.K., Anderson, M.S., and Greene, W.H., (1978), "Continuum Models for Beam- and Plate-like Lattice Structures," *AIAA Journal*, Vol. 16, No. 12, p. 1219-1228
- ¹⁸ Noor, A.K., and Weisstein, L.S., (1981), "Stability of Beamlike Lattice Trusses," *Computer Methods in Applied Mechanics and Engineering*, Vol. 25, p. 179-193
- ¹⁹ Dow, J.O., and Huyer, S.A., (1989), "Continuum Models of Space Station Structures," *Journal of Aerospace Engineering*, Vol. 2, No. 4, p. 220-237
- ²⁰ Gantes, C., Connor, J.J., and Logcher, R.D., (1994), "Equivalent Continuum Model for Deployable Flat Lattice Structures," *Journal of Aerospace Engineering*, Vol. 7, No. 1, p. 72-91
- ²¹ Kim, B.J. (1987), "A Methodology of an Equivalent Beam Modeling for a Nose-cone Missile," *Proceedings of the AIAA conference*, paper No. AIAA-1987-818, p. 1085-1092
- ²² Sun, C.T., and Kim, B.J., (1985), "Continuum Modeling of Periodic Truss Structures," *Damage Mechanics and Continuum Modeling*, edited by N. Stubbs and D. Krajcinovic, American Society of Civil Engineers, New York, p. 57-71
- ²³ Chen, C.C., and Sun, C.T., (1983), "Transient Analysis of Large Frame Structures by Simple Models," *Journal of Astronautical Sciences*, Vol. 31, No. 3, p. 359-379
- ²⁴ Abrate, S., (1985), "Continuum Modeling of Latticed Structures," *Shock and Vibration Digest*, Vol. 17, No. 1, p. 15-21
- ²⁵ Lake, M.S., and Klang, E.C., (1992), "Generation and Comparison of Globally Isotropic Space-Filling Truss Structures," *AIAA Journal*, Vol. 30, No. 5, p. 1416-1424.
- ²⁶ Kenner, W.S., and Knight, N.F., (1997) "Soft Lattice Truss Static Polynomial Response Using Energy Methods," *Proceedings of the AIAA/ASME/ASCE/AHS/ASC Structures, Structural Dynamics, and Materials Conference and Exhibit, 38th, and AIAA/ASME/AHS Adaptive Structures Forum*, Kissimmee, FL., paper AIAA-97-1376, p. 2900-2910

- ²⁷ Noor., A.K., and Russell, W.C., (1986) “Anisotropic Continuum Models for Beamlike Lattice Trusses,” *Computer Methods in Applied Mechanics and Engineering*, Vol. 57, p. 257-277
- ²⁸ Dow, J.O., Su, Z.W., Feng, C.C., (1985), “Equivalent Continuum Representation of Structures Composed of Repeated Elements,” *AIAA Journal*, Vol. 23, No. 10, p. 1564-1569
- ²⁹ Nayfeh, A.H., and Hefzy, M.S. (1978), “Continuum Modeling of Three-dimensional Truss-like Space Structures,” *AIAA Journal*, Vol. 16, No. 8, p. 779-787
- ³⁰ Nayfeh, A.H., and Hefzy, M.S., (1981), “Continuum Modeling of the Mechanical and Thermal Behavior of Discrete Large Structures,” *AIAA Journal*, Vol. 19, No. 6, p. 766-773
- ³¹ Wah, T., (1964), “Free Lateral Oscillations of a Supported Grillage,” Vol. 277, No. 4, p. 349-360
- ³² Shen, J.Y., Sharpe, L., and McGinley, W.M., (1995), “Identification of Dynamic Properties of Plate-like Structures by Using a Continuum Model,” *Mechanics Research Communications*, Vol. 22, No. 1, p. 67-78
- ³³ McCallen, D.B., and Romstad, K.M. (1990), “A Continuum Model for Lattice Structures with Geometric and Material Nonlinearities,” *Computers and Structures*, Vol. 37, No. 5, p. 795-822
- ³⁴ Ziegler, E., Accorsi, M., and Bennett, M., (2004), “Continuum Plate Model for Lattice Block Material,” *Journal of Mechanics of Materials*, Vol. 36, p. 753-766
- ³⁵ Oden, J.T., Bauman, P., and Prudhomme, S., (2005), “On the Extension of Goal-oriented Error Estimation and Hierarchical Modeling to Discrete Lattice Models,” *Computer Methods in Applied Mechanics and Engineering*, Vol. 194, p. 3668-3688
- ³⁶ Mohr, D., (2005), “Mechanism-based Multi-surface Plasticity Model for Ideal Truss Lattice Materials,” *International Journal of Solids and Structures*, Vol. 42, p. 3235-3260
- ³⁷ Potzta, G., and Kollar, L.P., (2003), “Analysis of Building Structures by Replacement Sandwich Beams,” *International Journal of Solids and Structures*, Vol. 40, p. 535-553
- ³⁸ Chajes, M.J., Zhang, L., and Kirby, J.T., (1996), “Dynamic Analysis of Tall Building Using Reduced-order Continuum Model,” *Journal of Structural Engineering*, Vol. 122, No. 11, p. 1284-1291
- ³⁹ Chajes, M.J., Finch, W.W., and Kirby, J.T., (1996), “Dynamic Analysis of a Ten-story Reinforced Concrete Building Using a Continuum Model,” *Journal of Computers and Structures*, Vol. 58, No. 3, p. 487-498

- ⁴⁰ Kim, K.S., Piziali, R.L., (1987), "Continuum Models of Materials with Beam Microstructures," *International Journal of Solids and Structures*, Vol. 23, No. 11, p. 1563-1578
- ⁴¹ Florence, C., and Sab, K., (2006) "A Rigorous Homogenization Method for the Determination of the Overall Ultimate Strength of Periodic Discrete Media and an Application to General Hexagonal Lattices of Beams," *European Journal of Mechanics A/Solids*, Vol. 25, p. 72-97
- ⁴² Cioranescu, D., and Donato, P., (2000), "An Introduction to Homogenization," Oxford Lectures Series in Mathematics and Its Applications
- ⁴³ Lamberson, S.E., (1985), "Equivalent continuum finite element modeling of plate-like space lattice structures," Air Force Institute of Tech. Wright-Patterson AFB OH., Doctoral Thesis
- ⁴⁴ Noor, A.K., and Nemeth, M.P., (1980), "Analysis of Spatial Beamlike Lattices with Rigid Joints," *Computer Methods in Applied Mechanics and Engineering*, Vol. 24, No. 1, p. 35-59
- ⁴⁵ Noor, A.K., and Nemeth, M.P., (1980), "Micropolar Beam Models for Lattice Grids with Rigid Joints," *Computer Methods in Applied Mechanics and Engineering*, Vol. 21, No. 2, p. 249-263
- ⁴⁶ Sun, C.T., and Yang, T.Y., (1973), "A Continuum Approach toward Dynamics of Grid Works," *Journal of Applied Mechanics*, Vol. 40, No. 1, p. 186-192
- ⁴⁷ Eringen, A.C., (1966), "Linear Theory of Micropolar Elasticity," *Journal of Mathematics and Mechanics*, Vol. 15, No. 6, p. 909-923
- ⁴⁸ Webster, M., Velde, W.V., (1991), "Modeling Beam-like Space Trusses with Nonlinear Joints," *Proceedings of the AIAA/ASME/ASCE/AHS/ASC 32nd Structures, Structural Dynamics, and Materials Conference*, Baltimore, MD, p. 2745-2754
- ⁴⁹ Soucy, Y., and Vigneron, F.R., (1984), "Identification of Structural Properties of a Continuous Longerons Space Mast," *Proceedings of the AIAA/ASME/ASCE/AHS 25th Structures, Structural Dynamics and Materials Conference*, Palm Springs, CA, p.130-139
- ⁵⁰ Tarazaga, P.A., Inman, D.J., and Wilkie, W., K., (2007), "Control of Space Rigidizable-Inflatable Boom Using Macro-Fiber Composite," *Journal of Vibration and Control*, Vol. 13, No. 7, p. 935-950
- ⁵¹ Papa, R.S., Lassiter, J.O., and Ross, B.P., (2003), "Structural Dynamics Experimental Activities in Ultra-light Weight and Inflatable Space Structures," *AIAA Journal of Spacecraft and Rockets*, Vol. 40, No. 1, p. 15-23

- ⁵² Guidanean, K., and Williams, G.T., (1998), "An Inflatable Rigidizable Truss Structure with Complex Joints," *Proceedings of the AIAA/ASME/SAE 39th Structures, Structural Dynamics and Materials Conference*, Long Beach, California, p. 2797-2806
- ⁵³ Inman, D.J., (2006), "Engineering Vibrations," 3rd edition, Prentice-Hall, Inc., Upper Saddle River, New Jersey, p. 509-513
- ⁵⁴ Timoshenko, S.P and Gere, J.M. (1972), "Mechanics of Materials," 2nd Ed., D. Van Nostrand Co., New York, N.Y.
- ⁵⁵ Davis, D.J. and Agnes, G.S. (2002), "Environmental Disturbance Modeling for Inflatable Space Structures," *Proceedings of the AIAA/ASME/ASCE/AHS/ASC 43rd Structures, Structural Dynamics, and Materials Conference*, Denver, CO., p. 1-8
- ⁵⁶ Perrygo, C., (2000), "Solar Shades," *Gossamer Spacecraft: Membrane and Inflatable Structures Technology for Space Applications*, C. H. M., Jenkins, Progress in Astronautics and Aeronautics, Vol. 191, AIAA, Reston, VA, p. 503-526
- ⁵⁷ Thornton, E.A. and Paul, D.B., (1985), "Thermal-structural Analysis of Large Space Structures: An assessment of recent advances" *Journal of Spacecraft*, Vol. 22, No. 4, p. 385-393
- ⁵⁸ Graham, J.D., (1970), "Solar Induced Bending Vibrations of a Flexible Member," *AIAA Journal*, Vol. 8, No. 11, p. 2031-2036
- ⁵⁹ Kraus, H. (1966), "Thermally Induced Vibrations of Thin Non-Shallow Spherical Shell," *AIAA Journal*, Vol. 4, No. 3, p. 500-505
- ⁶⁰ Schmit C.M., and Hanawalt A.J., (1957), "Skin Temperature of a Satellite," *Jet propulsion*, Vol. 27, No. 10, p. 1079-1083
- ⁶¹ Lida, T., Pelton J.N., and Ashford, E., (2003), "Satellite Communications in the 21st Century: Trends and Technologies," *Progress in Astronautics and Aeronautics*, Vol. 191, AIAA, Reston, Virginia
- ⁶² Thornton, E.A., and Paul, D.B., (1985), "Thermal Structural Analysis of Large Space structures: An Assessment of Recent Advances," *Journal of Spacecraft and Rockets*, Vol. 22, No.4, p. 385-393
- ⁶³ Beam, R.M., (1969), "On the Phenomenon of Thermoelastic Instability (Thermal Flutter) of Booms with Open Cross Section," NASA TN D-5222
- ⁶⁴ Thronton, E.A. and Foster, R.S., (1992), "Dynamic Response of Rapidly Heated Space Structures," *Computational Nonlinear Mechanics in Aerospace Engineering*, edited by Atluri, S.N., Progress in Astronautics and Aeronautics, Vol. 146, AIAA, Washington D.C., p. 451-477

- ⁶⁵ Johnston, J.D. and Thornton, E.A., (2000), "Thermally Induced Dynamics of Satellite Solar Panels," *Journal of Spacecraft and Rockets*, Vol. 37, No. 5, p. 604-613
- ⁶⁶ Krishna, R. and Bainumt, P. M., (1984), "Effect of Solar Radiation Disturbance on a Flexible Beam in Orbit," *AIAA Journal*, Vol. 22, No. 5, p. 677-682
- ⁶⁷ Johnston, J.D., and Thornton E.A., (1996), "An Evaluation of Thermally-Induced Structural Disturbances of Spacecraft Solar Array," *Proceedings of the 31st Intersociety of Energy Conversion Engineering Conference*, IECEC, Washington, DC, p. 1-6
- ⁶⁸ Donohue, J.H., and Frisch, H., (1969), "Thermo-elastic Instability of Open-Section Booms," NASA TN D5310, NASA, Washington D.C.
- ⁶⁹ Malla, R., Nash, W., and Lardner, T. (1988), "Thermal Effects on Very Large Space Structures," *Journal of Aerospace Engineering, ASCE*, Vol. 1, No. 3, p. 171-190
- ⁷⁰ Thornton, E.A., (1996), "Thermal Structures for Aerospace Applications," AIAA Educational series, Reston, Virginia
- ⁷¹ Anon, (1991), "Too Much Sun Gives Ulysses the Wobbles," *Electronic World and Wireless World*
- ⁷² Lambertson, M., Rohrbaugh, D., and Garrick, J., (1993), "Solar Array Thermal Snap and the Characteristics of Its Effects on UARS," *Flight Mechanics/ Estimation Theory Symposium*, NASA Goddard Spaceflight Center, Greenbelt, MD, p. 575-588
- ⁷³ Thornton, E.A. (1992), "Thermal Structures: Four Decades of Progress," *Journal of Aircraft*, Vol. 29, No. 3, p. 485-498
- ⁷⁴ Johnston, J.D., Foster, R.S., Eby, D.L., and Thornton, E.A., (1996), "Recent Progress in Thermally Induced Vibrations Research," *Proceedings of the 5th International Conference on Space 96*, Albuquerque, New Mexico, p. 1134-1140
- ⁷⁵ Foster, C.L., Tinker, M.L., Nurre, G.S. and Till, W.A., (1995), "The Solar Array Induced Disturbance of the Hubble Space Telescope Pointing System," *Journal of Spacecraft and Rockets*, Vol. 32, No. 4, p. 634-644, and NASA TP-3556
- ⁷⁶ Anderson, G.C., Quinn, D.A., Beals, G.A., Nelson, J.D., and Nurre, G.S., (1992), "An Overview of the Hubble Space Telescope Pointing Control System Design and Operation," *Proceedings of the AIAA Guidance, Navigation and Control Conference*, Head Island, SC, p. 1-10
- ⁷⁷ Thornton, E.A. and Kim, Y.A., (1993), "Thermally Induced Bending Vibrations of a Flexible Rolled-Up Solar Array," *Journal of Spacecraft and Rockets*, Vol. 30, No. 4, p. 438-448

- ⁷⁸ Angelia P. Bukley, (1995), "Hubble Space Telescope Pointing Control System Design Improvement Study Results," *Journal of Guidance, Control and Dynamics*, Vol. 18, No. 2, p. 194-199
- ⁷⁹ Chung, P.W. and Thornton, E.A., (1995), "Torsional Buckling and Vibrations of a Flexible Rolled Up Solar Array," *Proceedings of the AIAA/ASME/ASCE/AHS/ASC Structures, Structural Dynamics, and Materials Conference, 36th and AIAA/ASME Adaptive Structures Forum*, New Orleans, LA., p. 1654-1664
- ⁸⁰ Etkin, B. and Hughes, P.C., (1967), "Explanation of the Anomalous Spin Behavior of Satellites with Long Flexible Antenna," *Journal of Spacecraft*, Vol. 4, No. 9, p. 1139-1145
- ⁸¹ Frisch, H., (1967), "Thermal Bending Plus Twist of a Thin-walled Cylinder of Open Section with Application to Gravity Gradient Booms," NASA TN D 4069, Goddard Space Flight Center, Greenbelt, MD.
- ⁸² Koval, L.R., Mueller, M.R., and Paroczai, A.J., (1968), "Solar Flutter of a Thin-Walled Open Section Boom," *Symposium on Gravity Gradients Altitude Control Sponsored by the Air Force and Aerospace Corporation*, Los angles, California
- ⁸³ Kumar, R and Ahmed, S. (1972), "Bending and Flexing of the Apollo 15 Mass Spectrometer Boom," *Journal of Spacecraft*, Vol. 9, No.12, p. 940-942
- ⁸⁴ Bainum, P.M., Hamsath, N. and Krishna, R., (1980), "The Dynamics and Control of Large Space Structures after the Onset of Thermal Shock," *ACTA Astronautica*, Vol. 19, No. 1, p. 1-8
- ⁸⁵ Dennehy, C.J., Zimbelman, D.F., and Welch, R.V., (1990), "Sunrise/ Sunset Thermal Shock Disturbance Analysis and Simulation for the TOPEX Satellite," AIAA, Aerospace Sciences Meeting, 28th, Reno, NV, p.1-12
- ⁸⁶ Zimbelman, D.F., (1991), "Thermal Elastic shock and Its Effect on TOPEX Spacecraft Attitude Control," *Proceedings of the Annual Rocky Mountain Guidance and Control Conference*, Keystone, CO, p. 311-336
- ⁸⁷ Blackwood, G., Hyde, T., Miller, D., Crawley, E., Shao, M., and Laskin, R., (1993), "Stellar Interferometer Tracking Experiment: A Proposed Technology Demonstration Experiment," *Proceedings of the 44th Congress of International Astronautical Federation*, Graz, paper no: IAF-93-I.5-247, Graz, Austria
- ⁸⁸ Thornton, E.A. Chini, G.P., and Gulick D.W., (1995), "Thermally Induced Vibrations of a Self-Shadowed Split-Blanket Solar Array," *Journal of Spacecraft ad Rockets*, Vol. 32, No. 2, p. 302-311

- ⁸⁹ Foster, R.S. and Thornton, E.A., (1995), “Experimental Investigation of Thermally Induced Vibrations of Spacecraft Structures,” *Aerospace Thermal Structures and Materials for a New Era*, Thornton, E.A., *Progress in Astronautics and Aeronautics*, Vol.168, AIAA, Washington, D.C., p. 163-177 and AIAA-94-1380-CP, p. 584-596
- ⁹⁰ Johnston, J. D., and Thornton, E. A., (1998), “Thermally-Induced Attitude Dynamics of a Spacecraft with a Flexible Appendage,” *Journal of Guidance, Control and Dynamics*, Vol. 21, No. 4, p. 581–587
- ⁹¹ Fang, H., Lou, M., and Haung, J. (2003), “Thermal Distortion Analysis of a Three-Meter Inflatable Reflect-Array Antenna,” *Proceedings of the AIAA/ASME/SAE 44th Structures, Structural Dynamics and Materials Conference*, Norfolk, VA, p. 1–10
- ⁹² Lin, C., and Malla, (2004), “Coupled Thermo-Structural Analysis of an Earth Orbiting Flexible Structure,” *Proceedings of the AIAA/ASME/ASCE/AHS/ASC 45th Structures, Structural Dynamics & Materials Conference*, Palm Springs, California, p. 1-11
- ⁹³ Thornton, E.A. (1996), “Orbiting space structures,” *Thermal Structures for Aerospace Applications*, *Progress in Astronautics and Aeronautics*, AIAA, Reston, VA, p. 29
- ⁹⁴ Williams, R.B., and Agnes, G.S., (2006), “Minimum Mass Design of Large-Scale Space Trusses Subjected to Thermal Gradients,” *Proceedings of the 47th AIAA/ASME/ASCE/AHS/ASC Structures, Structural Dynamics, and Materials Conference*, Newport, Rhode Island, p. 1-21
- ⁹⁵ A. Unsold and B. Baschek (2002), “The New Cosmos: An Introduction to Astronomy and Astrophysics,” 5th Ed., Springer-Verlag, New York, p. 48
- ⁹⁶ Boley, B.A., (1956), “Thermally Induced Vibrations of Beams,” *Journal of Aeronautical Sciences*, Vol. 23, p. 179–181
- ⁹⁷ Mindlin, R.D., Goodman, L.E. and New York, N.Y., (1950), “Beam Vibrations with Time-Dependent Boundary Conditions,” *Journal of Applied Mechanics*, Vol. 17, p. 377-380
- ⁹⁸ Wetherhold, R.C. and Wang J., (1995), “Minimizing Thermal Deformation by Using Layered Structures” *Aerospace Thermal Structures and Materials for a New Era*, Thornton, E.A., *Progress in Astronautics and Aeronautics*, Vol.168, AIAA, Washington, D.C., p. 273-292
- ⁹⁹ Salehian, A., Seigler T.M., and Inman, D.J., (2007), “Dynamic Effects of a Radar Panel Mounted on a Truss Satellite,” *AIAA Journal*, Vol. 45, No. 7, p. 1642-1654
- ¹⁰⁰ Salehian, A., and Inman, D.J., (2008), “Dynamic Analysis of a Lattice Structure by Homogenization: Experimental Validation,” *Journal of Sound and Vibration*, to appear

- ¹⁰¹ Salehian, A., Seigler, T.M., and Inman, D.J., (2006), "Control of the Continuum Model of a Large Flexible Space Structure," *Proceedings of IMECE/ ASME International Mechanical Engineering Congress and Exposition*, paper No. IMECE2006-13362, Chicago, Illinois, p. 561-570
- ¹⁰² Berry, D.T., Yang, T.Y., Skelton, R.E., (1984), "Dynamics and Control of Lattice Beams Using Simplified Finite Element Models," *Journal of Guidance and Control*, Vol. 8, No. 5, p. 612-619
- ¹⁰³ Salehian, A., and Inman, D.J., (2005), "A Distributed Parameter Model of an ISAT," Presented at the 6th *SIAM conference on Control and Its Applications*, New Orleans, LA
- ¹⁰⁴ Salehian, A., Cliff, E.M. and Inman, D.J., (2005), "Continuum Modeling of a Slewing ISAT (Innovative Space Antenna Technology)," *Proceedings of the ASME International Design and Engineering Technical Conference*, Long Beach, California
- ¹⁰⁵ Salehian, A., Cliff, E.M. and Inman, D.J., (2006), "Natural Frequencies of an Innovative Space Based Radar Antenna by Continuum Modeling," *Proceedings of the 47th AIAA/ASME/ASCE/AHS/ASC Structures, Structural Dynamics, and Materials Conference*, Newport, Rhode Island
- ¹⁰⁶ Salehian, A., Inman, D.J., and Cliff, E.M., (2006), "Natural Frequency Validation of a Homogenized Model of a Truss," *Proceedings of the XXIV-International Modal Analysis Conference*, St. Louis, Missouri
- ¹⁰⁷ Salehian, A., Cliff, E.M. and Inman, D.J., (2008), "Natural Frequencies of an Innovative Space Based Radar Antenna by Continuum Modeling," To be presented at the 49th *AIAA/ASME/ASCE/AHS/ASC Structures, Structural Dynamics, and Materials Conference*, Schaumburg, Illinois
- ¹⁰⁸ Abrate, S., (1991), "Continuum modeling of lattice structures: Part III," *Shock and Vibration Digest*, Vol. 23, No. 3, p. 15-20
- ¹⁰⁹ Abrate, S., (1988), "Continuum modeling of latticed structures," *Shock and Vibration Digest*, Vol. 20, No. 10, p. 3-8
- ¹¹⁰ Mikulas M. M., (2003), "ISAT Truss Design Considerations," *Powerpoint Presentation to the ISAT Design Team*, Unpublished

Appendix A

Strain energy derivations for the hinge model

Following Ref. 17 the assumptions for a linear displacement field in Eq. (2.1) is made for this structure. The strain relations of the repeating element can be found very easily using the spatial derivatives of Eq. (2.1). The strain relations are then expended in their Taylor series form to account for the variations of the strain values along the x coordinate in the element as follow,

$$\begin{aligned}
 \varepsilon_{xx}^{(k)} &= \varepsilon_x - y^{(k)} \kappa_y + z^{(k)} \kappa_z + x^{(k)} \left(\frac{\partial \varepsilon_x}{\partial x} - y^{(k)} \frac{\partial \kappa_y}{\partial x} + z^{(k)} \frac{\partial \kappa_z}{\partial x} \right) \\
 \varepsilon_{yy}^{(k)} &= \varepsilon_{2,0} + x_1^{(k)} \frac{\partial \varepsilon_{2,0}}{\partial x_1} + \frac{1}{2} \left(x_1^{(k)} \right)^2 \frac{\partial^2 \varepsilon_{2,0}}{\partial x_1^2} \\
 \varepsilon_{zz}^{(k)} &= \varepsilon_{3,0} + x_1^{(k)} \frac{\partial \varepsilon_{3,0}}{\partial x_1} + \frac{1}{2} \left(x_1^{(k)} \right)^2 \frac{\partial^2 \varepsilon_{3,0}}{\partial x_1^2} \\
 \varepsilon_{xy}^{(k)} &= \frac{1}{2} \left(2\varepsilon_{xy} + y^{(k)} \frac{\partial \varepsilon_y}{\partial x} + z^{(k)} \left[-\kappa_x + \frac{1}{2} \left(2 \frac{\partial \varepsilon_{yz}}{\partial x} \right) \right] \right. \\
 &\quad \left. + x^{(k)} \left(2 \frac{\partial \varepsilon_{xy}}{\partial x} + y^{(k)} \frac{\partial^2 \varepsilon_y}{\partial x^2} + z^{(k)} \left[-\frac{\partial \kappa_x}{\partial x} + \frac{1}{2} \left(2 \frac{\partial^2 \varepsilon_{yz}}{\partial x^2} \right) \right] \right) \right) \\
 \varepsilon_{xz}^{(k)} &= \frac{1}{2} \left(2\varepsilon_{xz} + y^{(k)} \left[\kappa_x + \frac{1}{2} \left(2 \frac{\partial \varepsilon_{yz}}{\partial x} \right) \right] + z^{(k)} \frac{\partial \varepsilon_z}{\partial x} \right. \\
 &\quad \left. + x^{(k)} \left(2 \frac{\partial \varepsilon_{xz}}{\partial x} + y^{(k)} \left[\frac{\partial \kappa_x}{\partial x} + \frac{1}{2} \left(2 \frac{\partial^2 \varepsilon_{yz}}{\partial x^2} \right) \right] + z^{(k)} \frac{\partial^2 \varepsilon_z}{\partial x^2} \right) \right) \\
 \varepsilon_{yz}^{(k)} &= \varepsilon_{yz} + x^{(k)} \left(\frac{\partial \varepsilon_{yz}}{\partial x} \right) + \frac{1}{2} \left(x^{(k)} \right)^2 \frac{\partial^2 \varepsilon_{yz}}{\partial x^2}
 \end{aligned} \tag{A.1}$$

where superscript k denotes bar member ($k: 1 \rightarrow 18$) in the element shown in Figure 2-2, the strain components ε_x , ε_{xy} , ε_{xz} are the extensional and shear strain components

evaluated at the center of the element, κ_y , κ_z are the curvature, κ_x is the twist, u_0 , v_0 , w_0 are displacement components evaluated at the center of the element and ϕ_x , ϕ_y , ϕ_z are the rotational and torsional components. Using Eq. (A.1) the strain components can be evaluated at the center of the bar members. Following Noor,¹⁷ the relation used for the strain energy of a bar member k ,

$$U^{(k)} = \frac{1}{2} E^{(k)} A^{(k)} L^{(k)} \left(\varepsilon^{(k)} \right)^2 \quad (\text{A.2})$$

where $\varepsilon^{(k)}$ is the axial strain which is evaluated at the center of the member.

$$\varepsilon^{(k)} = \sum_{i=1}^3 \sum_{j=1}^3 \varepsilon_{ij}^{(k)} l_i^{(k)} l_j^{(k)} \quad (\text{A.3})$$

where $l_i^{(k)}$ and $l_j^{(k)}$ are the directional cosine of member (k) in the Cartesian coordinates. Using (A.1), (A.2), and (A.3) the strain energy of each of the longitudinal, batten and diagonal members can be found. As an example the strain components of member (13) (a diagonal member shown in Figure 2-2) are expanded in terms of the strain components at the center of the element and presented here,

$$\begin{aligned} \varepsilon_{xy}^{(13)} &= \frac{1}{2} \left(2\varepsilon_{xy} + \left(-\kappa_x + \frac{\partial \varepsilon_{yz}}{\partial x} \right) \left(\frac{-L_b}{2\sqrt{3}} \right) + \frac{L_L}{2} \left(2 \frac{\partial \varepsilon_{xy}}{\partial x} - \frac{L_b}{2\sqrt{3}} \left(-\frac{\partial \kappa_x}{\partial x} + \frac{\partial^2 \varepsilon_{yz}}{\partial x^2} \right) \right) \right) \\ \varepsilon_{xz}^{(13)} &= \frac{1}{2} \left(2\varepsilon_{xz} + \frac{L_L}{2} \left(2 \frac{\partial \varepsilon_{xz}}{\partial x} - \frac{L_b}{2\sqrt{3}} \frac{\partial^2 \varepsilon_z}{\partial x^2} \right) - \frac{L_b}{2\sqrt{3}} \frac{\partial \varepsilon_z}{\partial x} \right) \\ \varepsilon_{yz}^{(13)} &= \frac{1}{2} \left(2\varepsilon_{yz} + \frac{L_L^2}{4} \frac{\partial^2 \varepsilon_{yz}}{\partial x^2} + L_L \frac{\partial \varepsilon_{yz}}{\partial x} \right) \end{aligned}$$

$$\begin{aligned}
\varepsilon_{xx}^{(13)} &= \varepsilon_x + \left(\frac{-L_b}{2\sqrt{3}} \right) \kappa_z + \frac{L_L}{2} \left(\frac{\partial \varepsilon_x}{\partial x} - \frac{L_b}{2\sqrt{3}} \frac{\partial \kappa_z}{\partial x} \right) \\
\varepsilon_{yy}^{(13)} &= \varepsilon_y + \frac{1}{2} \left(\frac{L_L^2}{4} \frac{\partial^2 \varepsilon_y}{\partial x^2} + \frac{L_L}{2} \frac{\partial \varepsilon_y}{\partial x} \right) \\
\varepsilon_{zz}^{(13)} &= \varepsilon_z + \frac{L_L^2}{8} \frac{\partial^2 \varepsilon_z}{\partial x^2} + \frac{L_L}{2} \frac{\partial \varepsilon_z}{\partial x}
\end{aligned} \tag{A.4}$$

For the strain energy of all the diagonals we get:

$$\begin{aligned}
U_d &= \frac{1}{2} E_d A_d L_d \left(\left(c_1 \varepsilon_{xx}^{(13)} - c_3 \varepsilon_{xy}^{(13)} + c_2 \varepsilon_{yy}^{(13)} \right)^2 + \left(c_1 \varepsilon_{xx}^{(14)} + c_3 \varepsilon_{xy}^{(14)} + c_2 \varepsilon_{yy}^{(14)} \right)^2 + \right. \\
&\quad + \left(c_1 \varepsilon_{xx}^{(15)} + \frac{c_3}{2} \varepsilon_{xy}^{(15)} - \frac{\sqrt{3}c_3}{2} \varepsilon_{xz}^{(15)} + \frac{c_2}{4} \varepsilon_{yy}^{(15)} - \frac{\sqrt{3}c_2}{2} \varepsilon_{yz}^{(15)} + \frac{3c_2}{4} \varepsilon_{zz}^{(15)} \right)^2 \\
&\quad + \left(c_1 \varepsilon_{xx}^{(16)} - \frac{c_3}{2} \varepsilon_{xy}^{(16)} + \frac{\sqrt{3}c_3}{2} \varepsilon_{xz}^{(16)} + \frac{c_2}{4} \varepsilon_{yy}^{(16)} - \frac{\sqrt{3}c_2}{2} \varepsilon_{yz}^{(16)} + \frac{3c_2}{4} \varepsilon_{zz}^{(16)} \right)^2 \\
&\quad + \left(c_1 \varepsilon_{xx}^{(17)} + \frac{c_3}{2} \varepsilon_{xy}^{(17)} + \frac{\sqrt{3}c_3}{2} \varepsilon_{xz}^{(17)} + \frac{c_2}{4} \varepsilon_{yy}^{(17)} + \frac{\sqrt{3}c_2}{2} \varepsilon_{yz}^{(17)} + \frac{3c_2}{4} \varepsilon_{zz}^{(17)} \right)^2 \\
&\quad \left. + \left(c_1 \varepsilon_{xx}^{(18)} - \frac{c_3}{2} \varepsilon_{xy}^{(18)} - \frac{\sqrt{3}c_3}{2} \varepsilon_{xz}^{(18)} + \frac{c_2}{4} \varepsilon_{yy}^{(18)} + \frac{\sqrt{3}c_2}{2} \varepsilon_{yz}^{(18)} + \frac{3c_2}{4} \varepsilon_{zz}^{(18)} \right)^2 \right)
\end{aligned} \tag{A.5}$$

where c_1 , c_2 and c_3 are the square of 3 directional cosines as follow,

$$c_1 = \frac{L_L^2}{L_L^2 + L_b^2}, c_2 = \frac{L_b^2}{L_L^2 + L_b^2}, c_3 = \frac{2L_L L_b}{L_L^2 + L_b^2} \tag{A.6}$$

For the strain energy of the longerons we get:

$$\begin{aligned}
U_L = & \frac{1}{2} E_L A_L L_L \left(\varepsilon_x + \frac{L_b}{\sqrt{3}} \kappa_z + \frac{L_L}{2} \left(\frac{\partial \varepsilon_x}{\partial x} + \frac{L_b}{\sqrt{3}} \frac{\partial \kappa_z}{\partial x} \right) \right)^2 + \left(\varepsilon_x + \frac{L_b}{\sqrt{3}} \kappa_z - \frac{L_L}{2} \left(\frac{\partial \varepsilon_x}{\partial x} + \frac{L_b}{\sqrt{3}} \frac{\partial \kappa_z}{\partial x} \right) \right)^2 \\
& + \left(\varepsilon_x + \frac{L_b}{2} \kappa_y - \frac{L_b}{2\sqrt{3}} \kappa_z + \frac{L_L}{2} \left(\frac{\partial \varepsilon_x}{\partial x} + \frac{L_b}{2} \frac{\partial \kappa_y}{\partial x} - \frac{L_b}{2\sqrt{3}} \frac{\partial \kappa_z}{\partial x} \right) \right)^2 \\
& + \left(\varepsilon_x + \frac{L_b}{2} \kappa_y - \frac{L_b}{2\sqrt{3}} \kappa_z - \frac{L_L}{2} \left(\frac{\partial \varepsilon_x}{\partial x} + \frac{L_b}{2} \frac{\partial \kappa_y}{\partial x} - \frac{L_b}{2\sqrt{3}} \frac{\partial \kappa_z}{\partial x} \right) \right)^2 \\
& + \left(\varepsilon_x - \frac{L_b}{2} \kappa_y - \frac{L_b}{2\sqrt{3}} \kappa_z + \frac{L_L}{2} \left(\frac{\partial \varepsilon_x}{\partial x} - \frac{L_b}{2} \frac{\partial \kappa_y}{\partial x} - \frac{L_b}{2\sqrt{3}} \frac{\partial \kappa_z}{\partial x} \right) \right)^2 \\
& + \left(\varepsilon_x - \frac{L_b}{2} \kappa_y - \frac{L_b}{2\sqrt{3}} \kappa_z - \frac{L_L}{2} \left(\frac{\partial \varepsilon_x}{\partial x} - \frac{L_b}{2} \frac{\partial \kappa_y}{\partial x} - \frac{L_b}{2\sqrt{3}} \frac{\partial \kappa_z}{\partial x} \right) \right)^2
\end{aligned} \tag{A.7}$$

and finally for the battens we have,

$$\begin{aligned}
U_b = & \frac{1}{2} E_b A_b L_b \times \\
& \left(\frac{1}{4} \left(\varepsilon_y + L_L \frac{\partial \varepsilon_y}{\partial x} + \frac{L_L^2}{2} \frac{\partial^2 \varepsilon_y}{\partial x^2} \right) + \frac{3}{4} \left(\varepsilon_z + L_L \frac{\partial \varepsilon_z}{\partial x} + \frac{L_L^2}{2} \frac{\partial^2 \varepsilon_z}{\partial x^2} \right) + \frac{\sqrt{3}}{2} \left(\varepsilon_{yz} + L_L \frac{\partial \varepsilon_{yz}}{\partial x} + \frac{L_L^2}{2} \frac{\partial^2 \varepsilon_{yz}}{\partial x^2} \right) \right)^2 \\
& + \left(\frac{1}{4} \left(\varepsilon_y + L_L \frac{\partial \varepsilon_y}{\partial x} + \frac{L_L^2}{2} \frac{\partial^2 \varepsilon_y}{\partial x^2} \right) + \frac{3}{4} \left(\varepsilon_z + L_L \frac{\partial \varepsilon_z}{\partial x} + \frac{L_L^2}{2} \frac{\partial^2 \varepsilon_z}{\partial x^2} \right) - \frac{\sqrt{3}}{2} \left(\varepsilon_{yz} + L_L \frac{\partial \varepsilon_{yz}}{\partial x} + \frac{L_L^2}{2} \frac{\partial^2 \varepsilon_{yz}}{\partial x^2} \right) \right)^2 \\
& + \left(\varepsilon_y + L_L \frac{\partial \varepsilon_y}{\partial x} + \frac{L_L^2}{2} \frac{\partial^2 \varepsilon_y}{\partial x^2} \right)^2 + \varepsilon_y^2 + \left(\frac{1}{4} \varepsilon_y + \frac{3}{4} \varepsilon_z - \frac{\sqrt{3}}{2} \varepsilon_{yz} \right)^2 + \left(\frac{1}{4} \varepsilon_y + \frac{3}{4} \varepsilon_z + \frac{\sqrt{3}}{2} \varepsilon_{yz} \right)^2
\end{aligned} \tag{A.8}$$

From (A.5), (A.7) and (A.8), the strain energy of the truss element can be found in terms of a total of 21 strain and curvature components and their gradients. These are all evaluated at the center of the element. To find the continuum model the strain components should be found in terms of the displacement components and their derivative along the x coordinate only. For example an extensional strain component in the y direction ε_y is written in terms of the variation of the displacement component v in

the y direction ($\frac{\partial v}{\partial y}$). Therefore, this strain component needs to be found in terms of other strain components that can be expanded directly in terms of x . The solution for such strain values is considered reducing the order of the strain energy. To do this, necessary assumptions must be made, such as the local free deformation assumptions in Ref. 45. This means that forces associated with the local deformations should vanish and therefore the derivatives of the strain energy with respect to the following strain gradients should be zero. Making these assumptions will result in the following 9 equations,

$$\frac{\partial U_{total}}{\partial \frac{\partial \varepsilon_x}{\partial x}} = 0 \Rightarrow$$

$$6 \left(A_d E_d L_d L_L^3 + A_L E_L (L_b^2 + L_L^2)^2 \right) \frac{\partial \varepsilon_x}{\partial x} + A_d E_d L_b^2 L_d L_L \left(3 \frac{\partial \varepsilon_y}{\partial x} + 3 \frac{\partial \varepsilon_z}{\partial x} - 2\sqrt{3} \kappa_x \right) = 0$$

(a)

$$\frac{\partial U_{total}}{\partial \frac{\partial \kappa_y}{\partial x}} = 0 \Rightarrow$$

$$-A_d E_d L_b L_d L_L \frac{\partial \varepsilon_y}{\partial x} + 4 A_L E_L (L_b^2 + L_L^2)^2 \frac{\partial \kappa_y}{\partial x} + A_d E_d L_d L_L \left(L_L^2 \frac{\partial \kappa_y}{\partial x} + 2\sqrt{3} \left(L_b \frac{\partial \varepsilon_{yz}}{\partial x} + 4 \varepsilon_{xz} \right) \right)$$

$$+ A_d E_d L_b L_d L_L \frac{\partial \varepsilon_z}{\partial x} = 0$$

(b)

$$\frac{\partial U_{total}}{\partial \frac{\partial \kappa_z}{\partial x}} = 0 \Rightarrow$$

$$4 A_L E_L (L_L^2 + L_b^2) \frac{\partial \kappa_z}{\partial x} + A_d E_d L_d L_L \left(-\sqrt{3} L_b \frac{\partial \varepsilon_y}{\partial x} + \sqrt{3} L_b \frac{\partial \varepsilon_z}{\partial x} - 2 L_b \frac{\partial \varepsilon_{yz}}{\partial x} + L_L^2 \frac{\partial \kappa_z}{\partial x} + 8\sqrt{3} \varepsilon_{xy} \right) = 0$$

(c)

$$\frac{\partial U_{total}}{\partial \frac{\partial \varepsilon_{xy}}{\partial x}} = 0 \Rightarrow$$

$$3L_b L_L^2 \frac{\partial^2 \varepsilon_y}{\partial x^2} - 3L_b L_L^2 \frac{\partial^2 \varepsilon_z}{\partial x^2} + 4L_b \left(\sqrt{3} L_L^2 \frac{\partial^2 \varepsilon_{yz}}{\partial x^2} + 6\varepsilon_y - 6\varepsilon_z \right) - 8L_L^2 \left(6 \frac{\partial \varepsilon_{xy}}{\partial x} + \sqrt{3} \kappa_z \right) = 0$$

(d)

$$\frac{\partial U_{total}}{\partial \frac{\partial \varepsilon_{xz}}{\partial x}} = 0 \Rightarrow$$

$$\sqrt{3} L_b L_L^2 \frac{\partial^2 \varepsilon_y}{\partial x^2} - 24L_b \varepsilon_{yz} - L_L^2 \left(\sqrt{3} L_b \frac{\partial^2 \varepsilon_z}{\partial x^2} + 3L_b \frac{\partial^2 \varepsilon_{yz}}{\partial x^2} + 24 \frac{\partial \varepsilon_{xz}}{\partial x} + 4\sqrt{3} \kappa_y \right) = 0$$

(e)

$$\frac{\partial U_{total}}{\partial \frac{\partial \kappa_x}{\partial x}} = 0 \Rightarrow$$

$$L_L^2 \left(L_b^2 \left(\sqrt{3} \frac{\partial^2 \varepsilon_y}{\partial x^2} + \sqrt{3} \frac{\partial^2 \varepsilon_z}{\partial x^2} - 4 \frac{\partial \kappa_x}{\partial x} \right) + 16\sqrt{3} \varepsilon_x \right) + 8\sqrt{3} L_b^2 (\varepsilon_y + \varepsilon_z) = 0$$

(f)

$$\frac{\partial U_{total}}{\partial \frac{\partial^2 \varepsilon_y}{\partial x^2}} = 0 \Rightarrow$$

$$L_L^2 \left(13A_d E_d L_b^3 L_d + 72A_b E_b (L_b^2 + L_L^2)^2 \right) \frac{\partial^2 \varepsilon_y}{\partial x^2} + L_L^2 \left(-A_d E_d L_b^3 L_d + 24A_b E_b (L_b^2 + L_L^2)^2 \right) \frac{\partial^2 \varepsilon_z}{\partial x^2} +$$

$$+ 8(6A_b E_b L_L (L_b^2 + L_L^2)^2 \left(3 \frac{\partial \varepsilon_y}{\partial x} + \frac{\partial \varepsilon_z}{\partial x} \right) - A_d E_d L_b^2 L_d L_L^2 \left(6 \frac{\partial \varepsilon_{xy}}{\partial x} + 4\sqrt{3} \frac{\partial \varepsilon_{xz}}{\partial x} \right)$$

$$- \sqrt{3} A_d E_d L_b^3 L_d L_L^2 \frac{\partial \kappa_x}{\partial x} + 12A_d E_d L_b L_d L_L^2 \varepsilon_x + 18A_b E_b (L_b^4 + L_L^4) \varepsilon_y + 6A_b E_b (L_b^4 + L_L^4) \varepsilon_z$$

$$+ 12A_b E_b L_b^2 L_L^2 (3\varepsilon_y + \varepsilon_z) + A_d E_d L_b^3 L_d (9\varepsilon_y + 3\varepsilon_z - 4\sqrt{3} \varepsilon_{yz}) - A_d E_d L_b^2 L_d L_L^2 (2\kappa_y + \sqrt{3} \kappa_z) = 0$$

(g)

$$\begin{aligned}
& \frac{\partial U_{total}}{\partial \frac{\partial^2 \varepsilon_z}{\partial x^2}} = 0 \\
& \Rightarrow L_L^2 \left(-A_d E_d L_b^3 L_d + 24 A_b E_b (L_b^2 + L_L^2)^2 \right) \frac{\partial^2 \varepsilon_y}{\partial x^2} + L_L^2 \left(13 A_d E_d L_b^3 L_d + 72 A_b E_b (L_b^2 + L_L^2)^2 \right) \frac{\partial^2 \varepsilon_z}{\partial x^2} \\
& + 8(6 A_b E_b L_L (L_b^2 + L_L^2))^2 \left(\frac{\partial \varepsilon_y}{\partial x} + 3 \frac{\partial \varepsilon_z}{\partial x} \right) + 6 A_b E_b (L_b^4 + L_L^4) \varepsilon_y + 12 A_b E_b L_b^2 L_L^2 (\varepsilon_y + 3 \varepsilon_z) \\
& + 18 A_b E_b (L_b^4 + L_L^4) \varepsilon_z + A_d E_d L_b^2 L_d L_L^2 \left(6 \frac{\partial \varepsilon_{xy}}{\partial x} + 4\sqrt{3} \frac{\partial \varepsilon_{xz}}{\partial x} + 2\kappa_y + \sqrt{3}\kappa_z \right) - \sqrt{3} A_d E_d L_b^3 L_d L_L^2 \frac{\partial \kappa_x}{\partial x} \\
& + 12 A_d E_d L_b L_d L_L^2 \varepsilon_{1,0} + A_d E_d L_b^3 L_d (3\varepsilon_y + 9\varepsilon_z + 4\sqrt{3}\varepsilon_{yz}) = 0
\end{aligned} \tag{h}$$

$$\begin{aligned}
& \frac{\partial U_{total}}{\partial \frac{\partial^2 \varepsilon_{yz}}{\partial x^2}} = 0 \Rightarrow \\
& L_L^2 \left(7 A_d E_d L_b^3 L_d + 24 A_b E_b (L_b^2 + L_L^2)^2 \right) \frac{\partial^2 \varepsilon_{yz}}{\partial x^2} + 48 A_b E_b (L_b^2 + L_L^2)^2 \left(L_L \frac{\partial \varepsilon_{yz}}{\partial x} + \varepsilon_{yz} \right) \\
& + 4 A_d E_d L_b^2 L_d \left(2 L_b (\sqrt{3}\varepsilon_y - \sqrt{3}\varepsilon_z + 3\varepsilon_{yz}) + L_L^2 \left(-4\sqrt{3} \frac{\partial \varepsilon_{xy}}{\partial x} + 6 \frac{\partial \varepsilon_{xz}}{\partial x} + \sqrt{3}\kappa_y - 2\kappa_z \right) \right) = 0
\end{aligned} \tag{i}$$

(A.9)

Similarly in order to get a shear deformation type beam, the extensional stresses along the y and z directions and the shear stress in yz direction should vanish.¹⁷ Note that in a beam member, there is no extensional stress in the y and z direction in contrast to a block where all the three extensional stresses along the Cartesian coordinates exists. Also, there are no shear stresses on the sides of a beam and only shear stresses at the cross section are considered. These include the ε_{xz} and ε_{xy} . So the following should hold:

$$\begin{aligned} \frac{\partial U_{total}}{\partial \varepsilon_y} = 0 \Rightarrow \\ \left(A_d E_d L_b^3 L_d + 2 A_b E_b (L_b^2 + L_L^2) \right)^2 \left(\frac{\partial^2 \varepsilon_y}{\partial x^2} + \frac{\partial^2 \varepsilon_z}{\partial x^2} \right) + 12 A_b E_b (L_b^2 + L_L^2)^2 \left(3 L_L \frac{\partial \varepsilon_y}{\partial x} + L_L \frac{\partial \varepsilon_z}{\partial x} + 6 \varepsilon_y + 2 \varepsilon_z \right) \\ + 4 A_d E_d L_b L_d \left(24 L_L^2 \varepsilon_x + L_b^2 \left(\sqrt{3} L_L^2 \left(\frac{\partial^2 \varepsilon_{yz}}{\partial x^2} - 2 \frac{\partial \kappa_x}{\partial x} \right) + 6 (3 \varepsilon_y + \varepsilon_z) \right) - 2 L_b L_L^2 \left(6 \frac{\partial \varepsilon_{xy}}{\partial x} + \sqrt{3} \kappa_z \right) \right) = 0 \end{aligned}$$

$$\begin{aligned} \frac{\partial U_{total}}{\partial \varepsilon_z} = 0 \Rightarrow \\ \left(A_d E_d L_b^3 L_d + 2 A_b E_b (L_b^2 + L_L^2) \right)^2 \left(3 L_L^2 \frac{\partial^2 \varepsilon_y}{\partial x^2} + 9 L_L^2 \frac{\partial^2 \varepsilon_z}{\partial x^2} \right) + 12 A_b E_b (L_b^2 + L_L^2)^2 \left(L_L \frac{\partial \varepsilon_y}{\partial x} + 3 L_L \frac{\partial \varepsilon_z}{\partial x} + 2 \varepsilon_y + 6 \varepsilon_z \right) \\ - 4 A_d E_d L_b L_d \left(-24 L_L^2 \varepsilon_x + L_b^2 \left(\sqrt{3} L_L^2 \left(\frac{\partial^2 \varepsilon_{yz}}{\partial x^2} + 2 \frac{\partial \kappa_x}{\partial x} \right) - 6 (\varepsilon_y + 3 \varepsilon_z) \right) - 2 L_b L_L^2 \left(6 \frac{\partial \varepsilon_{xy}}{\partial x} + \sqrt{3} \kappa_z \right) \right) = 0 \end{aligned}$$

$$\begin{aligned} \frac{\partial U_{total}}{\partial \varepsilon_{yz}} = 0 \Rightarrow \\ 6 A_b E_b L_b (L_b^2 + L_L^2)^2 \left(L_L^2 \frac{\partial^2 \varepsilon_{yz}}{\partial x^2} + 2 L_L \frac{\partial \varepsilon_{yz}}{\partial x} + 4 \varepsilon_{yz} \right) \\ - A_d E_d L_b^3 L_d \left(\sqrt{3} L_b L_L^2 \frac{\partial^2 \varepsilon_y}{\partial x^2} - 24 L_b \varepsilon_{yz} - L_L^2 \left(\sqrt{3} L_b \frac{\partial^2 \varepsilon_z}{\partial x^2} + 3 L_b \frac{\partial^2 \varepsilon_{yz}}{\partial x^2} + 24 \frac{\partial \varepsilon_{xz}}{\partial x} + 4 \sqrt{3} \kappa_y \right) \right) = 0 \end{aligned} \quad (A.10)$$

On the other hand, the compatibility condition requires that the strain components at the plane the cross section of two adjacent elements (strain components ε_z , ε_y , ε_{yz}) be the same.⁴⁵ So we get,

$$\frac{\partial \varepsilon_y}{\partial x} = 0, \quad \frac{\partial \varepsilon_z}{\partial x} = 0, \quad \frac{\partial \varepsilon_{yz}}{\partial x} = 0 \quad (A.11)$$

The equations (A.9), (A.10) and (A.11) provide us with 15 equations to solve for 15 unknowns of the 21 strain components and their gradients. This results in a total of 6

independent strain and curvature components. Since we are interested in a 1-D beam type model, the strain components in a beam such as ε_x , κ_y , κ_z , κ_x , ε_{xy} and ε_{xz} are kept as independent variables and other strain components are expressed in terms of these strain values. Finally the strain energy of a repeating element can be found in terms of these 6 strain values as follow:

$$U = 3A_L E_L L_L (\varepsilon_x)^2 + \frac{1}{2} A_L E_L L_b^2 L_L \left((\kappa_y)^2 + (\kappa_z)^2 \right) + \frac{24 A_d A_L E_d E_L L_b^2 L_d L_L^2}{A_d E_d L_d L_L^3 + 4 A_L E_L (L_b^2 + L_L^2)^2} \left((\varepsilon_{xy})^2 + (\varepsilon_{xz})^2 \right) + \frac{A_d A_L E_d E_L L_b^4 L_d L_L^2}{4 \left(A_d E_d L_d L_L^3 + A_L E_L (L_b^2 + L_L^2)^2 \right)} (\kappa_x)^2$$

(A.12)

Appendix B

Decoupling the equations of motion

The procedure of decoupling of the equations of motion for the truss is presented here. As it is shown in the Eqs. (2-26) and (2-27), the bending coordinates v_0 and w_0 is coupled with the rotational component φ_y and φ_z respectively in the following form,

$$a \frac{\partial^2 \psi_1}{\partial t^2} + b \left(\psi_1 \pm \frac{\partial \psi_2}{\partial x} \right) + c \frac{\partial^2 \psi_1}{\partial x^2} = 0 \quad (\text{B.1})$$

$$a' \frac{\partial^2 \psi_2}{\partial t^2} + b' \left(\frac{\partial^2 \psi_2}{\partial x^2} \pm \frac{\partial \psi_1}{\partial x} \right) = 0 \quad (\text{B.2})$$

where ψ_1 is the rotational component and ψ_2 is the bending coordinate. Taking the partial derivative versus x from (B.1), we have,

$$a \frac{\partial^3 \psi_1}{\partial t^2 \partial x} + b \left(\frac{\partial \psi_1}{\partial x} \pm \frac{\partial^2 \psi_2}{\partial x^2} \right) + c \frac{\partial^3 \psi_1}{\partial x^3} = 0 \quad (\text{B.3})$$

$\frac{\partial \psi_1}{\partial x}$ can be found from (B.2) as follows,

$$\frac{\partial \psi_1}{\partial x} = \mp \left(a' \frac{\partial^2 \psi_2}{\partial t^2} + b' \frac{\partial^2 \psi_2}{\partial x^2} \right) \frac{1}{b'} \quad (\text{B.4})$$

Taking additional derivatives from (B.4) results in the following:

$$\frac{\partial^3 \psi_1}{\partial x \partial t^2} = \mp \left(a' \frac{\partial^4 \psi_2}{\partial t^4} + b' \frac{\partial^4 \psi_2}{\partial x^2 \partial t^2} \right) \frac{1}{b'} \quad (\text{B.5})$$

$$\frac{\partial^3 \psi_1}{\partial x^3} = \mp \left(a' \frac{\partial^4 \psi_2}{\partial t^2 \partial x^2} + b' \frac{\partial^4 \psi_2}{\partial x^4} \right) \frac{1}{b'} \quad (\text{B.6})$$

Substituting (B.4), (B.5) and (B.6) in (B.3), we can decouple the equations in the following form,

$$\mp \left(a \left(a' \frac{\partial^4 \psi_2}{\partial t^4} + b' \frac{\partial^4 \psi_2}{\partial x_1^2 \partial t^2} \right) \frac{1}{b'} + b \left(\left(a' \frac{\partial^2 \psi_2}{\partial t^2} + b' \frac{\partial^2 \psi_2}{\partial x_1^2} \right) \frac{1}{b'} - \frac{\partial^2 \psi_2}{\partial x_1^2} \right) + c \left(a' \frac{\partial^4 \psi_2}{\partial t^2 \partial x_1^2} + b' \frac{\partial^4 \psi_2}{\partial x_1^4} \right) \frac{1}{b'} \right) = 0 \quad (\text{B.7})$$

Therefore,

$$\eta \frac{\partial^4 \psi_2}{\partial t^4} + \alpha \frac{\partial^4 \psi_2}{\partial x^4} + \gamma \frac{\partial^2 \psi_2}{\partial t^2} + \xi \frac{\partial^4 \psi_2}{\partial x^2 \partial t^2} = 0 \quad (\text{B.8})$$

where the coefficients of this partial differential equation can be found as:

$$\eta = aa' = \frac{\rho^2 I}{\kappa^2 G} \Big|_{eq}, \quad \alpha = b'c = (EI)_{eq} \quad (\text{B.9})$$

$$\gamma = a'b = (\rho A)_{eq}, \quad \xi = ab' + a'c = -\rho I \left(1 + \frac{E}{\kappa^2 G} \right)_{eq}.$$

Appendix C

Strain energy for the Pratt Girder truss

A view of the repeating element for the planar truss, the joints and their interconnecting parts are shown in Figs. 3-1 and 3-2, respectively. As a preliminary analysis, we assume that the structure consists of pin joints. Therefore, similar to the outlined derivation for the 3-D structure in Chapter 1, the linear variation for the displacement components (u, w) along the z axis are assumed. The coordinate v_0 is not shown here in contrast with the 3D structure, because the structure is planar and therefore the bending perpendicular to the plane of the truss is ignored. So we get,

$$\begin{aligned} u(x, z) &= u_0(x) + z\phi_y(x) \\ w(x, z) &= w_0(x) + z\varepsilon_z(x) \end{aligned} \quad (\text{C.1})$$

where $u(x, z)$ and $w(x, z)$ are the displacement components along the x, z axis shown in Fig. 3-1 and $u_0(x), w_0(x)$ and $\phi_y(x)$ are the displacement and rotation components evaluated at the center of the element. The strain component $\varepsilon_z(x)$ is the extensional strain in the z direction evaluated at the center of the element and all of the $u_0(x), w_0(x)$, and $\phi_y(x)$ and $\varepsilon_z(x)$ depend on x coordinate only. Using Eq. (C.1) the strain components can be found by taking the derivatives of the displacement field with respect to the coordinates x, y, z ,

$$\begin{aligned} \varepsilon_x^{(k)} &= \frac{\partial u}{\partial x} = \frac{\partial u_0}{\partial x} + z \frac{\partial \phi_y}{\partial x} = \varepsilon_x + z^{(k)} \kappa_z \\ \varepsilon_z^{(k)} &= \varepsilon_z \\ \varepsilon_{xz}^{(k)} &= \frac{1}{2} \left(\frac{\partial u}{\partial z} + \frac{\partial w}{\partial x} \right) = \frac{1}{2} \underbrace{\left(\frac{\partial w_0}{\partial x} + \phi_y \right)}_{2\varepsilon_{xz}} = \varepsilon_{xz} \end{aligned} \quad (\text{C.2})$$

where superscript k denotes each of the 5 bar members in an element and ε_x , ε_{xz} , ε_z and κ_z are the strain and the curvature components evaluated at the center of the element and can be written as,

$$\varepsilon_x = \frac{\partial u_0}{\partial x}, \varepsilon_z = \frac{\partial w_0}{\partial z}, \varepsilon_{xz} = \frac{1}{2} \left(\frac{\partial w_0}{\partial x} + \phi_y \right), \kappa_z = \frac{\partial \phi_y}{\partial x} \quad (C.3)$$

Similar to the assumptions made for a 3-D truss element, a Taylor series expansion for the strain components is found to account for the strain variations along the length of an element. So we have,

$$\begin{aligned} \varepsilon_x^{(k)} &= \varepsilon_x + z^{(k)} \kappa_z + x^{(k)} \left(\frac{\partial \varepsilon_x}{\partial x} + z^{(k)} \frac{\partial \kappa_z}{\partial x} \right) \\ \varepsilon_z^{(k)} &= \varepsilon_z \\ \varepsilon_{xz}^{(k)} &= \varepsilon_{xz} + x^{(k)} \left(\frac{\partial \varepsilon_{xz}}{\partial x} \right) \end{aligned} \quad (C.4)$$

The strain energy of a bar in tension or compression can be written as,

$$U^{(k)} = \frac{1}{2} E^{(k)} A^{(k)} L^{(k)} \left(\varepsilon^{(k)} \right)^2 \quad (C.5)$$

where $\varepsilon^{(k)}$ is the strain value along the bar k and can be found using the strain values in (C.4) and their directional cosines with the bar member. From (C.5) the strain energy of the truss element can be found,

$$U_{total} = \frac{1}{2} E_L A_L L_L \left[\left(\varepsilon_x^{(2)} \right)^2 + \left(\varepsilon_x^{(4)} \right)^2 + \frac{\left(\varepsilon_z^{(1)} \right)^2 + \left(\varepsilon_z^{(3)} \right)^2}{2} \right] + \frac{1}{2} E_d A_d L_d \left[\frac{\left(\varepsilon_x^{(5)} \right)}{2} + \left(\varepsilon_{xz}^{(5)} \right) + \frac{\left(\varepsilon_z^{(5)} \right)}{2} \right]^2 \quad (C.6)$$

Using (C.4) and (C.6) the strain energy of an element can be written in terms of the strain components at the center of the element. So we get,

$$U_e = \frac{1}{8} \left(E_d A_d L_d (\varepsilon_x + \varepsilon_z + 2\varepsilon_{xz})^2 + 2E_L A_L L_L (4\varepsilon_x^2 + 2\varepsilon_z^2 + L_L^2 \kappa_z^2) \right) \quad (C.7)$$

To obtain an equivalent 1-D model the strain energy needs to be expanded in terms of the displacement components evaluated at the center and their derivative values with respect to the x axis only. Therefore, the strain ε_z in Eq. (C.6) needs to be written in terms of the other strain components. Similar to the approach used in Chapter 1, the assumption for a shear deformation type beam should hold. So we use the following relation to solve for ε_z ,

$$\frac{\partial U_{total}}{\partial \varepsilon_z} = 0 \quad (C.8)$$

Using (C.7) and (C.8) we find the following,

$$E_L A_L L_L \varepsilon_z + \frac{1}{4} E_d A_d L_d (\varepsilon_x + \varepsilon_z + 2\varepsilon_{xz}) = 0 \quad (C.9)$$

A solution to the (C.9) results in the relation for ε_z ,

$$\varepsilon_z = -\frac{A_d E_d L_d (\varepsilon_x + 2\varepsilon_{xz})}{A_d E_d L_d + 4E_L A_L L_L} \quad (C.10)$$

Making the substitution for (C.10) in (C.7) gives us the relation for the strain energy of the element,

$$U = \frac{1}{4(E_d A_d L_d + 4E_L A_L L_L)} (E_L A_L L_L (2(3E_d A_d L_d + 8E_L A_L L_L) \varepsilon_x^2 + 8E_d A_d L_d \varepsilon_x \varepsilon_{xz} + 8E_d A_d L_d \varepsilon_{xz}^2 + L_L^2 (E_d A_d L_d + 4E_L A_L L_L) \kappa_z^2)) \quad (C.11)$$

Finally, using the relation (C.3) we can expand the strain energy expression of the repeating truss element in terms of the displacement components in the following form:

$$\begin{aligned}
U_e = & \frac{E_L A_L L_L}{4(E_d A_d L_d + 4E_L A_L L_L)} (2E_d A_d L_d \phi_y^2 + 2E_d A_d L_d \left(\frac{\partial w_0}{\partial x}\right)^2) \\
& + L_L^2 (A_d E_d L_d + 4E_L A_L L_L) \left(\frac{\partial \phi_y}{\partial x}\right)^2 + 4A_d E_d L_d \frac{\partial w_0}{\partial x} \frac{\partial u_0}{\partial x} \\
& + 2(3E_d A_d L_d + 8E_L A_L L_L) \left(\frac{\partial u_0}{\partial x}\right)^2 + 4E_d A_d L_d \psi_0 \left(\frac{\partial w_0}{\partial x} + \frac{\partial u_0}{\partial x}\right)
\end{aligned} \tag{C.12}$$

Kinetic energy for the Pratt Girder truss

Similar to the appendix A, it can be proved very easily that the kinetic energy of a bar in planar motion shown in Fig. C.1 can be written as,

$$T = \frac{1}{6} \rho A L (V_{x,1}^2 + V_{z,1}^2 + V_{x,2}^2 + V_{z,2}^2 + V_{x,1} V_{x,2} + V_{z,1} V_{z,2}) \tag{C.13}$$

where ρ , A , L are density, cross sectional area and length of the bar. Using Eqs. (C.13) and Eq. (2.1) and ignoring the stain terms in the kinetic energy derivations, we get the following relation for the kinetic energy of a bar member (k) in the element,

$$\begin{aligned}
T^{(k)} = & \frac{1}{6} \rho^{(k)} A^{(k)} L^{(k)} \left(\left(\frac{\partial u_0}{\partial t} + z_{(1)}^{(k)} \frac{\partial \phi_y}{\partial t} \right)^2 + 3 \left(\frac{\partial w_0}{\partial t} \right)^2 + \left(\frac{\partial u_0}{\partial t} + z_{(2)}^{(k)} \frac{\partial \phi_y}{\partial t} \right)^2 \right. \\
& \left. + \left(\frac{\partial u_0}{\partial t} + z_{(1)}^{(k)} \frac{\partial \phi_y}{\partial t} \right) \left(\frac{\partial u_0}{\partial t} + z_{(2)}^{(k)} \frac{\partial \phi_y}{\partial t} \right) \right)
\end{aligned} \tag{C.14}$$

Here $z_{(1)}^{(k)}$ and $z_{(2)}^{(k)}$ are the z coordinate of each of the two nodes of the bar member (k).

Also for the kinetic energy of the joints we get,

$$T_j = m_j \left(\left(\frac{\partial u_0}{\partial t} \right)^2 + \left(\frac{\partial w_0}{\partial t} \right)^2 + \frac{1}{4} L_L^2 \left(\frac{\partial \phi_y}{\partial t} \right)^2 \right) \tag{C.15}$$

The kinetic energy of the repeating element can be written in terms of the kinetic energy of the bar members and the joints as follows,

$$T_e = \frac{T^{(1)}}{2} + T^{(2)} + \frac{T^{(3)}}{2} + T^{(4)} + T^{(5)} + T_j \quad (\text{C.16})$$

where $T^{(1)}$, $T^{(2)}$, $T^{(3)}$, $T^{(4)}$ and $T^{(5)}$ are the kinetic energy of the bar members and T_j is the kinetic energy of the joints. Note that half of the bar members 1 and 3 belong to the adjacent truss elements and therefore half of their kinetic energies are included here. The same assumption was made for the strain energy derivation. Using (C.14) the kinetic energy for the truss element (with no joints) can be expanded in the following form,

$$\begin{aligned} T_m = & \frac{1}{2}(3A_L\rho_L L_L + A_d\rho_d L_d) \left(\left(\frac{\partial u_0}{\partial t} \right)^2 + \left(\frac{\partial w_0}{\partial t} \right)^2 \right) \\ & + \frac{1}{24} L_L^2 (7A_L\rho_L L_L + A_d\rho_d L_d) \left(\frac{\partial \phi_y}{\partial t} \right)^2 \end{aligned} \quad (\text{C.17})$$

Using (C.15), (C.16) and (C.17), we get the relation for the kinetic energy of the truss element as follow,

$$\begin{aligned} T_e = & \frac{1}{2}(3A_L\rho_L L_L + A_d\rho_d L_d) \left(\left(\frac{\partial u_0}{\partial t} \right)^2 + \left(\frac{\partial w_0}{\partial t} \right)^2 \right) \\ & + \frac{1}{24} L_L^2 (7A_L\rho_L L_L + A_d\rho_d L_d) \left(\frac{\partial \phi_y}{\partial t} \right)^2 \\ & + \frac{1}{4} m_j \left(4 \left(\frac{\partial u_0}{\partial t} \right)^2 + 4 \left(\frac{\partial w_0}{\partial t} \right)^2 + L_L^2 \left(\frac{\partial \phi_y}{\partial t} \right)^2 \right) \end{aligned} \quad (\text{C.18})$$

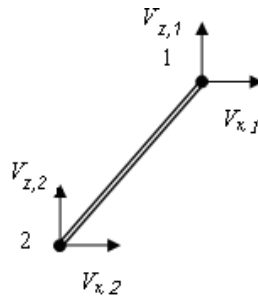


Figure C-1 Schematic view of a bar and the nodal velocities

Appendix D

Micropolar model of the 3D truss

Using the relation (4.1) and the Cartesian coordinates of the longeron members the extensional components for these members can be found as:

$$\begin{aligned}
 \Delta_{L1} &= \left(\varepsilon_x + \frac{L_b\sqrt{3}}{3} \kappa_z \right) L_L + \left(\partial\varepsilon_x + \frac{L_b\sqrt{3}}{3} \partial\kappa_z \right) \frac{L_L^2}{2} \\
 \Delta_{L2} &= \left(\varepsilon_x - \frac{L_b}{2} \kappa_y - \frac{L_b\sqrt{3}}{6} \kappa_z \right) L_L + \left(\partial\varepsilon_x - \frac{L_b}{2} \partial\kappa_y - \frac{L_b\sqrt{3}}{6} \partial\kappa_z \right) \frac{L_L^2}{2} \\
 \Delta_{L3} &= \left(\varepsilon_x + \frac{L_b}{2} \kappa_y - \frac{L_b\sqrt{3}}{6} \kappa_z \right) L_L + \left(\partial\varepsilon_x + \frac{L_b}{2} \partial\kappa_y - \frac{L_b\sqrt{3}}{6} \partial\kappa_z \right) \frac{L_L^2}{2} \\
 \Delta_{L4} &= - \left(\varepsilon_x + \frac{L_b\sqrt{3}}{3} \kappa_z \right) L_L + \left(\partial\varepsilon_x + \frac{L_b\sqrt{3}}{3} \partial\kappa_z \right) \frac{L_L^2}{2} \\
 \Delta_{L5} &= - \left(\varepsilon_x - \frac{L_b}{2} \kappa_y - \frac{L_b\sqrt{3}}{6} \kappa_z \right) L_L + \left(\partial\varepsilon_x - \frac{L_b}{2} \partial\kappa_y - \frac{L_b\sqrt{3}}{6} \partial\kappa_z \right) \frac{L_L^2}{2} \\
 \Delta_{L6} &= - \left(\varepsilon_x + \frac{L_b}{2} \kappa_y - \frac{L_b\sqrt{3}}{6} \kappa_z \right) L_L + \left(\partial\varepsilon_x + \frac{L_b}{2} \partial\kappa_y - \frac{L_b\sqrt{3}}{6} \partial\kappa_z \right) \frac{L_L^2}{2} \tag{D.1}
 \end{aligned}$$

Bending and extension of battens for ε_z component

In the section the bending and extension of the batten members using the ε_z components are found. Figure D-1 shows the deformation of the element cross section as a result of the ε_z strain component. The deflection components V1 and V2 are the projection of the deflections along the perpendicular direction of these members (bending components).

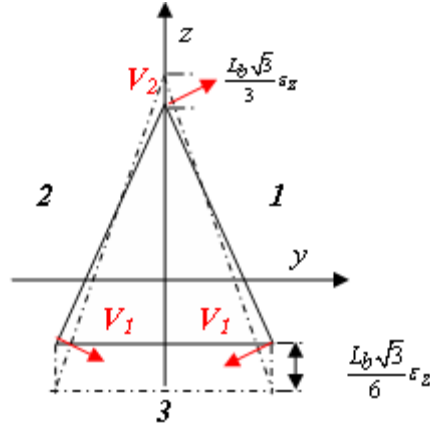


Figure D-1 Bending and extension of battens for ε_z

Using Figure D-1 for members 1 and 2 we get:

$$\frac{dl}{dz} = \frac{z}{l} \rightarrow dl = dz \frac{z}{l} \rightarrow dl_1 = dl_2 = \frac{L_b \sqrt{3}}{2L_b} \frac{L_b \sqrt{3}}{2} \varepsilon_z = \frac{3L_b \varepsilon_z}{4} \quad (\text{D.2})$$

Also, it is obvious from this figure that the strain value ε_z does not contribute to the extension of members 3. The bending deflection components V_1 and V_2 can be found as follow:

$$\begin{aligned} V_1 &= \frac{L_b \sqrt{3}}{6} \varepsilon_z \cos(60) = \frac{L_b \sqrt{3}}{12} \varepsilon_z \\ V_2 &= \frac{L_b \sqrt{3}}{3} \varepsilon_z \cos(60) = \frac{L_b \sqrt{3}}{6} \varepsilon_z \end{aligned} \quad (\text{D.3})$$

Bending and extension of battens for ε_{yz} and ε_{zy} component

We use a similar approach to find the bending and extension of the batten members for the ε_{yz} component. The cross section distortion for this strain component is shown in Figure D-2.

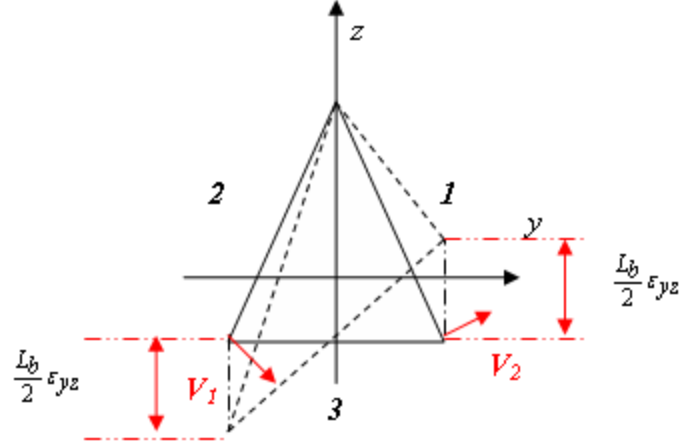


Figure D-2 Bending and extension of battens for ε_{yz}

The extension of members 1 and 2 can be found as:

$$\frac{dl}{dz} = \frac{z}{l} \rightarrow dl = dz \frac{z}{l} \rightarrow \begin{cases} dl_1 = -\frac{L_b \sqrt{3}}{2} \frac{L_b}{L_b} \varepsilon_{yz} = -\frac{L_b \sqrt{3}}{4} \varepsilon_{yz} \\ dl_2 = \frac{L_b \sqrt{3}}{2} \frac{L_b}{L_b} \varepsilon_{yz} = \frac{L_b \sqrt{3}}{4} \varepsilon_{yz} \end{cases} \quad (\text{D.4})$$

For member 3 we get:

$$\begin{aligned} l_{new} &= \sqrt{L_b^2 + (L_b \varepsilon_{yz})^2} = L_b \sqrt{1 + (\varepsilon_{yz})^2} \\ \rightarrow dl &= \text{Lim} \left(L_b \sqrt{1 + (\varepsilon_{yz})^2} - L_b \right)_{\varepsilon_{yz} \rightarrow 0} \\ \rightarrow dl_3 &= L_b \frac{(\varepsilon_{yz})^2}{2} \end{aligned} \quad (\text{D.5})$$

Similar to the previous section, the bending deflections V_1 and V_2 for these members are,

$$V_1 = V_2 = \frac{L_b}{2} \varepsilon_{yz} \cos(60) = \frac{L_b}{4} \varepsilon_{yz} \quad (\text{D.6})$$

The cross section distortion for the ε_{zy} component is shown in Figure D-3.

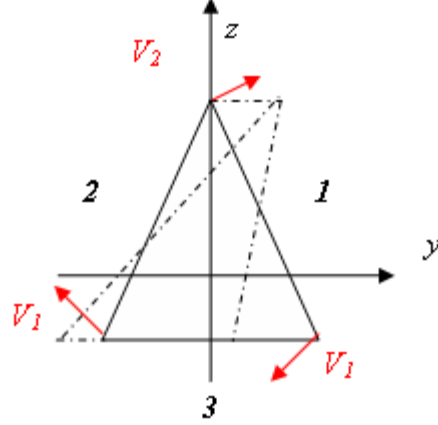


Figure D-3 Bending and extension of battens for ε_{zy}

The extension for 1 and 2 for this strain can be found as,

$$\frac{dl}{dy} = \frac{y}{l} \rightarrow dl = dy \frac{y}{l} \rightarrow \begin{cases} dl_1 = -\frac{L_b \sqrt{3}}{2} \varepsilon_{yz} \frac{\frac{L_b}{2}}{L_b} = -\frac{L_b \sqrt{3}}{4} \varepsilon_{yz} \\ dl_2 = \frac{L_b \sqrt{3}}{4} \varepsilon_{yz} \end{cases} \quad (D.7)$$

For member 3 at the bottom we have,

$$dl_3 = 0 \quad (D.8)$$

Finally the bending deflections V_1 and V_2 are,

$$\begin{aligned} V_1 &= \frac{L_b \sqrt{3}}{6} \varepsilon_{yz} \cos(30) = \frac{L_b}{4} \varepsilon_{yz} \\ V_2 &= \frac{L_b \sqrt{3}}{3} \varepsilon_{yz} \cos(30) = \frac{L_b}{2} \varepsilon_{yz} \end{aligned} \quad (D.9)$$

Using the relations for the bending and extensional strain of the batten members as a result of the ε_{zy} , ε_{yz} , ε_z , and ε_y the total extension and bending deflections of the battens can be found. For the extension of the batten members marked 1 in the Figure D-1, we have:

$$\frac{L_b \varepsilon_y}{4} + \frac{3L_b \varepsilon_z}{4} - \frac{L_b \sqrt{3}}{2} \varepsilon_{yz} \quad (D.10)$$

and for the second and third members we get,

$$\frac{L_b \varepsilon_y}{4} + \frac{3L_b \varepsilon_z}{4} + \frac{L_b \sqrt{3}}{2} \varepsilon_{yz}$$

$$L_b \varepsilon_y + L_b \frac{(\varepsilon_{yz})^2}{2} \quad (D.11)$$

Calculations for the bending strain energy of a beam member

Using the stiffness method in Timoshenko,⁵⁴ the shear forces and bending moments as a result of the deflection components shown in Figure D-4.

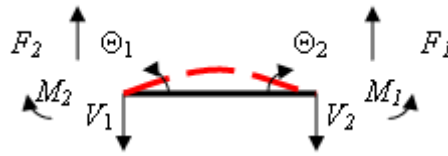


Figure D-4 Schematic of a beam member, the deflection components and nodal reactions

Table D-1 Nodal reactions for the rotational and displacement components

	F_1	M_1	F_2	M_2
V_1	$\frac{12EI}{L^3} V_1$	$-\frac{6EI}{L^2} V_1$	$-\frac{12EI}{L^3} V_1$	$\frac{6EI}{L^2} V_1$
V_2	$-\frac{12EI}{L^3} V_2$	$\frac{6EI}{L^2} V_2$	$\frac{12EI}{L^3} V_2$	$-\frac{6EI}{L^2} V_2$
θ_1	$-\frac{6EI}{L^2} \theta_1$	$\frac{4EI}{L} \theta_1$	$\frac{6EI}{L^2} \theta_1$	$-\frac{2EI}{L} \theta_1$
θ_2	$\frac{6EI}{L^2} \theta_2$	$-\frac{2EI}{L} \theta_2$	$-\frac{6EI}{L^2} \theta_2$	$\frac{4EI}{L} \theta_2$

The strain energy of the beam member shown in Figure D-4 under nodal shear forces and bending moments can be obtained as,

$$U = \frac{1}{2} V_1 \sum F_1 + \frac{1}{2} V_2 \sum F_2 + \frac{1}{2} \theta_1 \sum M_1 + \frac{1}{2} \theta_2 \sum M_2 \quad (D.12)$$

Using Eq. (D.12) and Table D-1 we get,

$$U = \frac{EI}{L} \left(\frac{6(V_1 - V_2)^2}{L^2} - \frac{6(V_1 - V_2)(\theta_1 - \theta_2)}{L} + 2(\theta_1^2 + \theta_2^2 - \theta_1\theta_2) \right) \quad (D.13)$$

From the bending components calculated for the batten and the longeron members and using (D.13) the bending strain energy of these members can be found as in (4.4) and (4.13).

Reduced order continuum model assumptions

In addition to the assumptions stated in section (4.2), the relations regarding the compatibility condition, the shear deformation type beam and the local free deformations as stated in Chapter 2 and following Ref. 45 must be employed. These equations for the frame element with micro-rotations take the following form:

For free local deformations we should have,

$$\begin{aligned} \frac{\partial U_e}{\partial \left(\frac{\partial \varepsilon_x}{\partial x} \right)} &= \frac{\partial U_e}{\partial \left(\frac{\partial \kappa_y}{\partial x} \right)} = \frac{\partial U_e}{\partial \left(\frac{\partial \kappa_z}{\partial x} \right)} = \frac{\partial U_e}{\partial \left(\frac{\partial \varepsilon_{xy}}{\partial x} \right)} = \frac{\partial U_e}{\partial \left(\frac{\partial \varepsilon_{xz}}{\partial x} \right)} = \frac{\partial U_e}{\partial \left(\frac{\partial \kappa_x}{\partial x} \right)} \\ &= \frac{\partial U_e}{\partial \left(\frac{\partial^2 \varepsilon_y}{\partial x^2} \right)} = \frac{\partial U_e}{\partial \left(\frac{\partial^2 \varepsilon_z}{\partial x^2} \right)} = \frac{\partial U_e}{\partial \left(\frac{\partial^2 \varepsilon_{yz}}{\partial x^2} \right)} = 0 \end{aligned} \quad (D.14)$$

Therefore we get the following 9 equations,

$$6 \left(A_d E_d L_d L_L^3 + (L_b^2 + L_L^2)^2 A_L E_L \right) \frac{\partial \varepsilon_x}{\partial x} + A_d E_d L_d L_L L_b^2 \left(3 \frac{\partial \varepsilon_y}{\partial x} + 3 \frac{\partial \varepsilon_z}{\partial x} - 2\sqrt{3} \kappa_x \right) = 0 \quad (D.15)$$

$$4 A_L E_L \frac{\partial \kappa_y}{\partial x_1} + \frac{A_d E_d L_d L_L \left(L_b \left(-\frac{\partial \varepsilon_y}{\partial x_1} + \frac{\partial \varepsilon_z}{\partial x_1} + 2\sqrt{3} \frac{\partial \varepsilon_{xz}}{\partial x_1} \right) + L_L^2 \frac{\partial \kappa_y}{\partial x_1} + 8\sqrt{3} \varepsilon_{xz} \right)}{(L_b^2 + L_L^2)^2} = 0 \quad (D.16)$$

$$4A_L E_L \frac{\partial \kappa_z}{\partial x_1} + \frac{A_d E_d L_d L_L \left(L_b \left(-\sqrt{3} \frac{\partial \varepsilon_y}{\partial x_1} + \sqrt{3} \frac{\partial \varepsilon_z}{\partial x_1} - 2 \frac{\partial \varepsilon_{yz}}{\partial x_1} \right) + L_L^2 \frac{\partial \kappa_z}{\partial x_1} + 8\sqrt{3} \varepsilon_{xy} \right)}{(L_b^2 + L_L^2)^2} = 0 \quad (\text{D.17})$$

$$3L_b L_L^2 \frac{\partial^2 \varepsilon_y}{\partial x_1^2} - 3L_b L_L^2 \frac{\partial^2 \varepsilon_z}{\partial x_1^2} + 4L_b \left(\sqrt{3} L_L^2 \frac{\partial^2 \varepsilon_{yz}}{\partial x_1^2} + 6\varepsilon_y - 6\varepsilon_z \right) - 8L_L^2 \left(6 \frac{\partial \varepsilon_{xy}}{\partial x_1} + \sqrt{3} \kappa_z \right) = 0 \quad (\text{D.18})$$

$$\sqrt{3} L_b L_L^2 \frac{\partial^2 \varepsilon_y}{\partial x^2} - 24L_b \varepsilon_{yz} - L_L^2 \left(\sqrt{3} L_b \frac{\partial^2 \varepsilon_z}{\partial x^2} + 3L_b \frac{\partial^2 \varepsilon_{yz}}{\partial x^2} + 24 \frac{\partial \varepsilon_{xz}}{\partial x} + 4\sqrt{3} \kappa_y \right) = 0 \quad (\text{D.19})$$

$$L_L^2 \left(L_b^2 \left(\sqrt{3} \frac{\partial^2 \varepsilon_y}{\partial x_1^2} + \sqrt{3} \frac{\partial^2 \varepsilon_z}{\partial x_1^2} - 4 \frac{\partial \kappa_x}{\partial x_1} \right) + 16\sqrt{3} \varepsilon_x \right) + 8\sqrt{3} L_b^2 (\varepsilon_y + \varepsilon_z) = 0 \quad (\text{D.20})$$

$$\begin{aligned} & L_L^2 \left(13A_d E_d L_b^3 L_d + 72(L_b^2 + L_L^2)^2 A_b E_b \right) \frac{\partial^2 \varepsilon_y}{\partial x^2} + L_L^2 \left(-A_d E_d L_b^3 L_d + 24(L_b^2 + L_L^2)^2 A_b E_b \right) \frac{\partial^2 \varepsilon_z}{\partial x^2} \\ & + 8(6(L_b^2 + L_L^2)^2 A_b E_b \left(3L_L \frac{\partial \varepsilon_y}{\partial x} + L_L \frac{\partial \varepsilon_z}{\partial x} + 3\varepsilon_y + \varepsilon_z \right) - L_b L_L^2 \left(4\sqrt{3} \frac{\partial \varepsilon_{xz}}{\partial x} + 2\kappa_y + \sqrt{3} \kappa_z \right) \\ & A_d E_d L_b L_d (6L_b L_L^2 \frac{\partial \varepsilon_{xy}}{\partial x} - 12L_L^2 \varepsilon_x + L_b^2 \left(\sqrt{3} L_L^2 \frac{\partial \kappa_x}{\partial x} - 3\varepsilon_y - 9\varepsilon_z + 4\sqrt{3} \varepsilon_{yz} \right)) = 0 \end{aligned} \quad (\text{D.21})$$

$$\begin{aligned}
& L_L^2 \left(-A_d E_d L_b^3 L_d + 24 (L_b^2 + L_L^2)^2 A_b E_b \right) \frac{\partial^2 \varepsilon_y}{\partial x_1^2} + L_L^2 \left(13 A_d E_d L_b^3 L_d + 72 (L_b^2 + L_L^2)^2 A_b E_b \right) \frac{\partial^2 \varepsilon_z}{\partial x_1^2} \\
& + 8 (L_b^2 + L_L^2)^2 A_b E_b \left(L_L \frac{\partial \varepsilon_y}{\partial x_1} + 3 L_L \frac{\partial \varepsilon_z}{\partial x_1} + \varepsilon_y + 3 \varepsilon_z \right) + L_b L_L^2 \left(4 \sqrt{3} \frac{\partial \varepsilon_{xz}}{\partial x_1} + 2 \kappa_y + \sqrt{3} \kappa_z \right) \\
& A_d E_d L_b L_d \left(6 L_b L_L^2 \frac{\partial \varepsilon_{xy}}{\partial x_1} + 12 L_L^2 \varepsilon_x - L_b^2 \left(\sqrt{3} L_L^2 \frac{\partial \kappa_x}{\partial x_1} - 9 \varepsilon_y - 3 \varepsilon_z - 4 \sqrt{3} \varepsilon_{yz} \right) \right) = 0
\end{aligned} \tag{D.22}$$

$$\begin{aligned}
& L_L^2 \left(7 A_d E_d L_b^3 L_d + 24 (L_b^2 + L_L^2)^2 A_b E_b \right) \frac{\partial^2 \varepsilon_{yz}}{\partial x^2} + 48 (L_L^2 + L_b^2)^2 A_b E_b \left(L_L \frac{\partial \varepsilon_{yz}}{\partial x} + \varepsilon_{yz} \right) + \\
& 4 A_d E_d L_d L_b^2 \left(2 L_b (\sqrt{3} \varepsilon_y - \sqrt{3} \varepsilon_z + 3 \varepsilon_{yz}) + L_L^2 \left(-4 \sqrt{3} \frac{\partial \varepsilon_{xy}}{\partial x} + 6 \frac{\partial \varepsilon_{xz}}{\partial x} + \sqrt{3} \kappa_y - 2 \kappa_z \right) \right) = 0
\end{aligned} \tag{D.23}$$

For a shear-deformation-type beam theory the following should hold,

$$\frac{\partial U_e}{\partial \varepsilon_y} = \frac{\partial U_e}{\partial \varepsilon_z} = \frac{\partial U_e}{\partial \varepsilon_{yz}} = 0 \tag{D.24}$$

which gives us the additional 3 equations in the following form:

$$\begin{aligned}
& \frac{1}{L_b} (96 E_b (8 I_b (\sqrt{3} \theta_{1b} - \sqrt{3} \theta_{2b} + \sqrt{3} \theta_{3b} - \sqrt{3} \theta_{6b} + \sqrt{3} \theta_{7b} - \sqrt{3} \theta_{8b} + \sqrt{3} \theta_{9b} - \sqrt{3} \theta_{12b} + 6 \varepsilon_y - 6 \varepsilon_z) \\
& + L_b^2 A_b (L_L (3 L_L \frac{\partial^2 \varepsilon_y}{\partial x_1^2} + L_L \frac{\partial^2 \varepsilon_z}{\partial x_1^2} + 6 \frac{\partial \varepsilon_y}{\partial x_1} + 2 \frac{\partial \varepsilon_z}{\partial x_1}) + 4 (3 \varepsilon_y + \varepsilon_z))) \\
& + \frac{1}{(L_b^2 + L_L^2)^2} (16 A_d E_d L_b^2 L_d (9 L_b^2 L_L^2 \frac{\partial^2 \varepsilon_y}{\partial x_1^2} + 3 L_b^2 L_L^2 \frac{\partial^2 \varepsilon_z}{\partial x_1^2} + 96 L_L^2 \varepsilon_z \\
& + 4 L_b^2 (\sqrt{3} L_L^2 \left(\frac{\partial^2 \varepsilon_{yz}}{\partial x_1^2} - 2 \frac{\partial \kappa_x}{\partial x_1} \right) + 6 (3 \varepsilon_y + \varepsilon_z)) - 8 L_b L_L^2 \left(6 \frac{\partial \varepsilon_{xy}}{\partial x_1} + \sqrt{3} \kappa_z \right)) = 0
\end{aligned} \tag{D.25}$$

$$\begin{aligned}
& \frac{1}{L_b} (96E_b(-8I_b(\sqrt{3}\theta_{1b} - \sqrt{3}\theta_{2b} + \sqrt{3}\theta_{3b} - \sqrt{3}\theta_{6b} + \sqrt{3}\theta_{7b} - \sqrt{3}\theta_{8b} + \sqrt{3}\theta_{9b} - \sqrt{3}\theta_{12b} + 6\varepsilon_{2,0} - 6\varepsilon_z) + \\
& L_b^2 A_b (L_L (L_L \frac{\partial^2 \varepsilon_y}{\partial x_1^2} + 3L_L \frac{\partial^2 \varepsilon_z}{\partial x_1^2} + 2 \frac{\partial \varepsilon_y}{\partial x_1} + 6 \frac{\partial \varepsilon_z}{\partial x_1}) + 4(\varepsilon_y + 3\varepsilon_z))) \\
& + \frac{1}{(L_b^2 + L_L^2)^2} (16A_d E_d L_b^2 L_d (3L_b^2 L_L^2 \frac{\partial^2 \varepsilon_y}{\partial x_1^2} + 9L_b^2 L_L^2 \frac{\partial^2 \varepsilon_z}{\partial x_1^2} + 96L_L^2 \varepsilon_x - 4L_b^2 (\sqrt{3}L_L^2 \left(\frac{\partial^2 \varepsilon_{yz}}{\partial x_1^2} + 2 \frac{\partial \kappa_x}{\partial x_1} \right) \\
& - 6(\varepsilon_y + 3\varepsilon_z)) + 8L_b L_L^2 \left(6 \frac{\partial \varepsilon_{xy}}{\partial x_1} + \sqrt{3}\kappa_z \right)) = 0
\end{aligned} \tag{D.26}$$

$$\begin{aligned}
& \frac{1}{8L_b} (-6E_b(4I_b(\theta_{1b} + \theta_{2b} - \theta_{3b} + 2\theta_{4b} + 2\theta_{5b} - \theta_{6b} + \theta_{7b} + \theta_{8b} - \theta_{9b} + 2\theta_{10b} + 2\theta_{11b} - \theta_{12b} - 12\varepsilon_{yz}) \\
& - L_b^2 A_b (L_L^2 \frac{\partial^2 \varepsilon_{yz}}{\partial x_1^2} + 2L_L \frac{\partial \varepsilon_{yz}}{\partial x_1} + 4\varepsilon_{yz})) + \frac{1}{(L_b^2 + L_L^2)^2} (A_d E_d L_d L_b^4 (-\sqrt{3}L_b L_L^2 \frac{\partial^2 \varepsilon_y}{\partial x_1^2} + 24L_b \varepsilon_{yz} \\
& + L_L^2 (\sqrt{3}L_b \frac{\partial^2 \varepsilon_z}{\partial x_1^2} + 3L_b \frac{\partial^2 \varepsilon_{yz}}{\partial x_1^2} + 24 \frac{\partial \varepsilon_{xz}}{\partial x_1} + 4\sqrt{3}\kappa_y))) = 0
\end{aligned} \tag{D.27}$$

Finally the compatibility equations require that,

$$\frac{\partial \varepsilon_y}{\partial x} = \frac{\partial \varepsilon_z}{\partial x} = \frac{\partial \varepsilon_{yz}}{\partial x} = 0 \tag{D.28}$$

These equations and the relations in section 4.2 are used to find the equivalent 1 dimensional reduced order model for the micro-polar structure.

Appendix E

Strain energy calculations of the planar truss element

The assumptions used for the 3-D truss element are employed here for the fundamental repeating element of the planar truss. Similar to the previous the assumptions for the displacement field at the cross section are made. The strain values are then calculated to find the extensions and bending of the individual members. Subsequently, the bending and extensional strain energies are calculated.

The elongation for the longeron members can be found using the following relation:

$$\Delta = \int_{-\frac{L_L}{2}}^{\frac{L_L}{2}} \varepsilon_x(x) dx = \int_{-\frac{L_L}{2}}^{\frac{L_L}{2}} \left[(\varepsilon_x + z\kappa_z) + x^{(k)} (\partial \varepsilon_x + z \partial \kappa_z) \right] dx = \left((\varepsilon_x + z\kappa_z)x + (\partial \varepsilon_x + z \partial \kappa_z) \frac{x^2}{2} \right) \Big|_{-\frac{L_L}{2}}^{\frac{L_L}{2}} \quad (\text{E.1})$$

So for the 5 members shown in the Figure 4-8, we get the following relations for the extension of the members:

$$\begin{aligned} \Delta_1 &= \varepsilon_z L_b \\ \Delta_2 &= \frac{L_L}{2} \left(\varepsilon_x + \frac{L_b}{2} \kappa_z \right) - \left(-\frac{L_L}{2} \left(\varepsilon_x + \frac{L_b}{2} \kappa_z \right) \right) = \left(\varepsilon_x + \frac{L_b}{2} \kappa_z \right) L_L \\ \Delta_3 &= \varepsilon_z L_b \\ \Delta_4 &= \frac{L_L}{2} \left(\varepsilon_x - \frac{L_b}{2} \kappa_z \right) - \left(-\frac{L_L}{2} \left(\varepsilon_x - \frac{L_b}{2} \kappa_z \right) \right) = \left(\varepsilon_x - \frac{L_b}{2} \kappa_z \right) L_L \\ \Delta_5 &= \frac{L_L^2}{2L_d} (2\varepsilon_x) + \varepsilon_z \frac{L_b^2}{L_d} + 2 \frac{L_b L_L}{L_d} \varepsilon_{xz} \end{aligned} \quad (\text{E.2})$$

Consequently the strain energy as a result of the tension-compression of these members

can be found using the relation, $U_{ext} = \frac{EA}{2L} \Delta_i^2$

$$\begin{aligned}
U_{ext} = & \frac{E_b A_b}{2L_b} (\varepsilon_z L_b)^2 + \frac{E_L A_L}{2L_L} \left(\left(\varepsilon_x + \frac{L_b}{2} \kappa_z \right)^2 L_L^2 + \left(\varepsilon_x - \frac{L_b}{2} \kappa_z \right)^2 L_L^2 \right) \\
& + \frac{E_d A_d}{2L_d} \left(\frac{L_L^2}{2L_d} \left(2\varepsilon_x + \frac{L_b L_L}{2} \partial \kappa_z \right) + \varepsilon_z \frac{L_b^2}{L_d} + 2 \frac{L_b L_L}{L_d} \varepsilon_{xz} \right)^2
\end{aligned} \tag{E.3}$$

Similarly the bending components of the longeron and batten members must be found to account for the bending strain energy of these members. For the batten member shown in Figure E-1 we have:

$$\begin{aligned}
V_1 &= -\frac{L_b}{2} (\varepsilon_{xz}) + \left(\varepsilon_x - \frac{L_b}{2} \kappa_z \right) \left(-\frac{L_L}{2} \right) \\
V_2 &= \frac{L_b}{2} (\varepsilon_{xz}) + \left(\varepsilon_x + \frac{L_b}{2} \kappa_z \right) \left(-\frac{L_L}{2} \right)
\end{aligned} \tag{E.4}$$

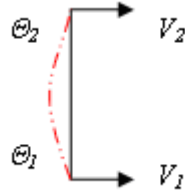


Figure E-1 Batten member and the bending components

Similarly for the longeron members shown in Figure E-2 we get the following:

$$\begin{aligned}
V_1 &= \frac{L_L}{2} (\varepsilon_{xz}) + (\varepsilon_z) \left(-\frac{L_b}{2} \right) \\
V_2 &= -\frac{L_L}{2} (\varepsilon_{xz}) + (\varepsilon_z) \left(-\frac{L_b}{2} \right)
\end{aligned} \tag{E.5}$$

and,

$$\begin{aligned}
V_1 &= \frac{L_L}{2} (\varepsilon_{xz}) + (\varepsilon_z) \frac{L_b}{2} \\
V_2 &= -\frac{L_L}{2} (\varepsilon_{xz}) + (\varepsilon_z) \frac{L_b}{2}
\end{aligned} \tag{E.6}$$

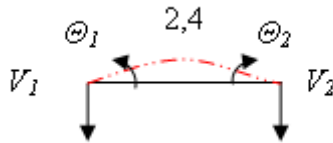


Figure E-2 Longeron members and the bending components

Finally using the relation in (D.13) the bending strain energy of these members can be found.

Bending and extension of the diagonal member

Presented here is the calculation for the bending and extension of the diagonal member for this planar truss. These components can be found using the superposition method and each of the individual strain components ε_x , ε_z and ε_{xz} . For the bending deflections of the diagonal member as a result of the strain component ε_x and κ_z we get:

$$\begin{aligned}
 V_{11} &= -\frac{L_L}{2} \left(\varepsilon_x - \frac{L_b}{2} \kappa_z \right) \frac{L_b}{L_d} \\
 V_{12} &= \frac{L_L}{2} \left(\varepsilon_x + \frac{L_b}{2} \kappa_z \right) \frac{L_b}{L_d}
 \end{aligned} \tag{E.7}$$

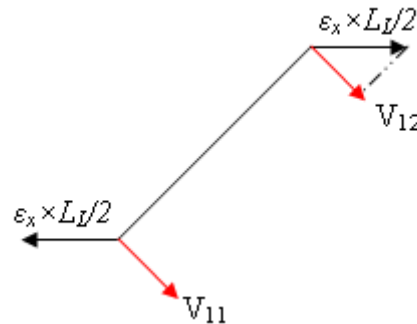


Figure E-3 Bending of the diagonal member for ε_x and κ_z

Similarly for the bending components as a result of the strain component ε_z we have,

$$\begin{aligned}
 V_{21} &= \frac{L_b}{2} \varepsilon_z \frac{L_L}{L_d} \\
 V_{22} &= -\frac{L_b}{2} \varepsilon_z \frac{L_L}{L_d}
 \end{aligned} \tag{E.8}$$

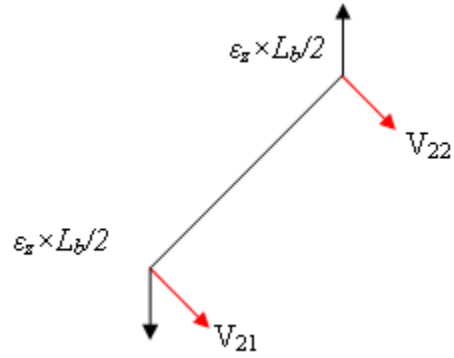


Figure E-4 Bending of the diagonal member for ε_z

and finally for the ε_{zx} and ε_{xz} we have:

$$V_{31} = -\frac{L_b}{2} \varepsilon_{zx} \frac{L_b}{L_d}$$

$$V_{32} = \frac{L_b}{2} \varepsilon_{zx} \frac{L_b}{L_d} \quad (\text{E.9})$$

and,

$$V_{41} = \frac{L_L}{2} \varepsilon_{xz} \frac{L_L}{L_d}$$

$$V_{42} = -\frac{L_L}{2} \varepsilon_{xz} \frac{L_L}{L_d} \quad (\text{E.10})$$

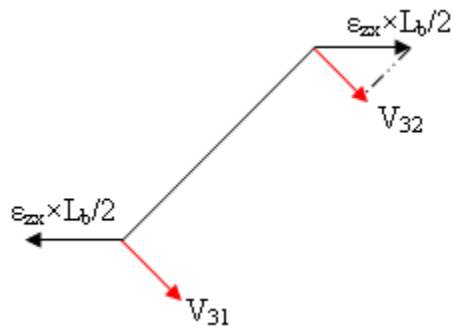


Figure E-5 Bending of the diagonal member for ε_{zx}

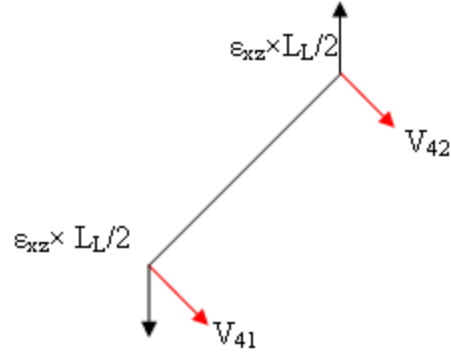


Figure E-6 Bending of the diagonal member for ϵ_{xz}

Therefore the total bending components for this member is,

$$\begin{aligned}
 V_1 = V_{11} + V_{21} + V_{31} + V_{41} &= -\frac{L_L}{2} \left(\epsilon_x - \frac{L_b}{2} \kappa_z \right) \frac{L_b}{L_d} + \frac{L_b}{2} (\epsilon_z) \frac{L_L}{L_d} - \frac{L_b}{2} (\epsilon_{xz}) \frac{L_b}{L_d} + \frac{L_L}{2} (\epsilon_{xz}) \frac{L_L}{L_d} \\
 V_2 = V_{12} + V_{22} + V_{32} + V_{42} &= \frac{L_L}{2} \left(\epsilon_x + \frac{L_b}{2} \kappa_z \right) \frac{L_b}{L_d} - \frac{L_b}{2} (\epsilon_z) \frac{L_L}{L_d} + \frac{L_b}{2} (\epsilon_{xz}) \frac{L_b}{L_d} - \frac{L_L}{2} (\epsilon_{xz}) \frac{L_L}{L_d}
 \end{aligned}
 \tag{E.11}$$

Extension of the diagonal member

The elongation of the diagonal member can be found in a very similar manner. Figure E-7 shows the extension of this member as a result of the ϵ_x .

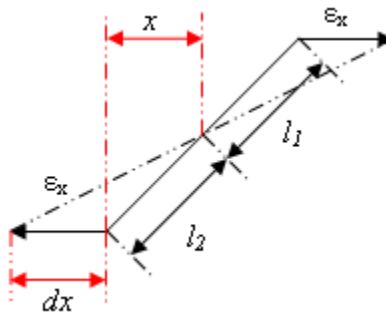


Figure E-7 Extension of the diagonal member for ϵ_x

Using this figure the following relations can be found very easily.

$$l_1 = l_2 = \frac{L}{2} \quad (\text{E.12})$$

$$dl = \frac{x dx}{l} \quad (\text{E.13})$$

So we get:

$$dl_1 = \frac{L_L}{2} \frac{L_L}{2} \left(\varepsilon_x + \frac{L_b}{2} \kappa_z \right) \frac{1}{\varepsilon_x \left(\frac{L_L}{2} \right)^2} \frac{L_d}{2} \quad (\text{E.14})$$

$$dl_2 = \frac{L_L}{2} \frac{L_L}{2} \left(\varepsilon_x - \frac{L_b}{2} \kappa_z \right) \frac{1}{\varepsilon_x \left(\frac{L_L}{2} \right)^2} \frac{L_d}{2} \quad (\text{E.15})$$

Finally for the extension as a result of the extensional strain ε_x we have:

$$dl = dl_1 + dl_2 = \frac{L_L^2}{L_d} \varepsilon_x \quad (\text{E.16})$$

Also, for the ε_z component the strain in the diagonal member can be written in the form:

$$dl = L_b \varepsilon_z \frac{L_d}{L_b} = \varepsilon_z L_d \quad (\text{E.17})$$

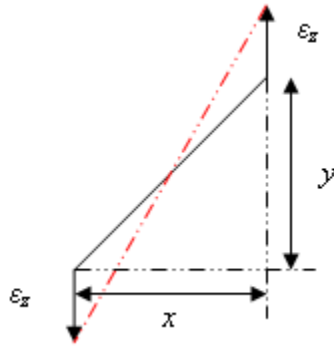


Figure E-8 Extension of the diagonal member for ε_z

Similarly using Figure E-9 for ε_{xz} we get:

$$l_1^2 = x^2 + y^2 \rightarrow dl_1 = \frac{x dx}{l} \quad (\text{E.18})$$

$$dl_1 = \frac{L_b}{2} \varepsilon_{xz} \frac{L_L}{2} \frac{1}{\frac{L_d}{2}} \quad (\text{E.19})$$

$$dl_2 = \frac{L_b}{2} \varepsilon_{xz} \frac{L_L}{2} \frac{1}{\frac{L_d}{2}} \quad (\text{E.20})$$

$$dl = dl_1 + dl_2 = \frac{L_b L_L}{L_d} \varepsilon_{xz} \quad (\text{E.21})$$

and finally for ε_{zx} we have,

$$dl_1 = \frac{y dy}{l_1} \quad (\text{E.22})$$

$$dl_1 = \frac{L_L}{2} \varepsilon_{zx} \frac{L_b}{2} \frac{1}{\frac{L_d}{2}} \quad (\text{E.23})$$

$$dl_2 = \frac{L_L}{2} \varepsilon_{zx} \frac{L_b}{2} \frac{1}{\frac{L_d}{2}} \quad (\text{E.24})$$

$$dl = dl_1 + dl_2 = \frac{L_L L_b}{L_d} \varepsilon_{zx} \quad (\text{E.25})$$

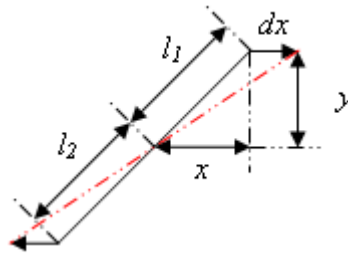


Figure E-9 Extension of the diagonal member for ε_{zx}

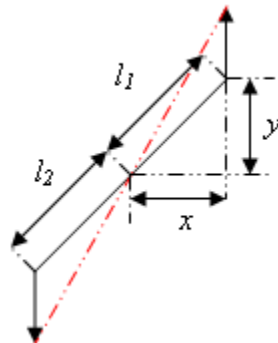


Figure E-10 Extension of the diagonal member for ε_{xz}

Vita

Armaghan Salehian received a Bachelor of Science degree in Mechanical Engineering from Sharif University of Technology in 1997. She started her first job as an oil and gas equipment design engineer in Enerchimi Engineering Company in Tehran, Iran, in the June 1997. Armaghan then received her Master of Science degree from University of Tehran in 2000. In the fall of 2001, she moved to the United States and received her second Master of Science degree in Mechanical Engineering from Worcester Polytechnic Institute in Worcester, MA, in 2003. She has won a NSF-*AdvanceVT* postdoctoral fellowship and will start her job as a postdoctoral fellow in the February 2008. Starting April 2008, Armaghan will start her new position as an Assistant Professor in the Mechanical Engineering department at the University of Waterloo in Ontario, Canada.